PENETRATION DEPTH STUDIES OF UNCONVENTIONAL SUPERCONDUCTORS

BY

EE MIN ELBERT CHIA

B.S., University of Auckland, 1992
M.S., University of Illinois at Urbana-Champaign, 1999

DISSERTATION

Submitted in partial fulfillment of the requirements
for the degree of Doctor of Philosophy in Physics
in the Graduate College of the
University of Illinois at Urbana-Champaign, 2004

Urbana, Illinois

Abstract

The magnetic penetration depth λ of various unconventional superconductors have been measured down to $\sim$0.1 K using a tunnel-diode based, self-inductive technique at 21 and 28 MHz. The samples measured are the heavy-fermion superconductors $CeCoIn_5$ and $PrOs_4Sb_{12}$, the rare-earth borocarbides $RENi_2B_2C$ (RE = Y, Lu, Er, Ho), the spin-triplet superconductor Sr_2RuO_4, and elemental Pb. From these studies we see how superconductivity is affected by the presence of another order, such as paramagnetism/antiferromagnetism (in $ErNi_2B_2C$) or spin-density-wave (in Pb). We also see how the superfluid response is modified by nonlocal corrections in $CeCoIn_5$ and Sr_2RuO_4. Hints of multi-band superconductivity are seen in YNi_2B_2C, $LuNi_2B_2C$ and Sr_2RuO_4. Finally, we observe point-node behavior in $PrOs_4Sb_{12}$, whose superconductivity is suggested to be non-magnetic in origin — the first of its kind. Various theoretical models have been used to fit the data. Some of the work are still ongoing.

To my parents

Chia Kang Seah and Wong Moey Ngen

Acknowledgments

First and foremost I would like to thank my advisor, Professor Myron Salamon, for his constant encouragement and support all these years. The depth and breadth of his knowledge of physics, and his ability to utilize a seemingly unrelated branch of physics to apply to the problem at hand, is always a sight to behold. I also thank him for believing in me and telling me that I am a better physicist than I thought I am. I thank Professor Dale Van Harlingen for letting me live in his lab, for the many stimulating discussions, and most of all, for preventing his graduate students from taking away my Lakeshore temperature controller. I deeply appreciate the fruitful sessions spent with Professor Russ Giannetta, who explained to me the many intricacies of the tunnel diode oscillator circuit.

Next I want to thank Ismardo Bonalde and Brian Yanoff, for teaching me, from zero upwards, everything about low-temperature physics, low-noise electronics and superconductivity when I first joined them four years ago. Besides Professor Salamon, Ismardo has certainly set the benchmark for me to follow. David Lawrie from the Giannetta group was never tired of discussing and explaining to me the many practical issues related to the penetration depth setup. I thank all past and present members of my group — Ismardo, Kevin, Peter, Hideto, Tuson, Scott, Wesley, Young, Dario, and Tuan, for their friendship and help. Special thanks to Tuson for the many hours of discussing about superconductivity, and about life and faith; to Scott for his knowledge of Latex and every equipment in the lab, and to Hideto for sharing his knowledge of how to take care of an infant. Outside my group, I thank Aki and Jaime for our fighting the Qual battle together, for the numerous lunch discussions, and for their special friendship. I also thank Spencer Schultz and Cliff Gulyash of the MRL

machine shop for their finely-machined components, their cheerful demeanor, and sharing with me their extensive knowledge of machining. Special thanks also to Steve Burdin and Ernie Sammon from the CMM, for coming to my rescue at a time when I was beginning to wonder if I'll ever graduate.

Outside of MRL, I want to thank our friends from the Illini Chinese Christian Fellowship, for giving Renee, Daniel and myself a family away from home. Our heartfelt thanks to Pastor Michael McQueen for his many acts of love and concern to our family that are too many to innumerate. Half a world away, I want to thank my parents, my grandparents, and my many uncles and aunts, for their extravagant love for me and sacrifices in bringing me up. Without them, I will not be who I am today.

I thank God for giving me Renee, my wife, and Daniel, our 2-year-old son, to be with me here in Urbana. Renee's constant support and prayer have been a major source of strength for me. Daniel's entry into this world, and his remarkable growth, has been a source of great joy to both of us. Most of all, I thank my Lord Jesus Christ, who sustained me and strengthened me throughout these $5\frac{1}{2}$ years, and who was with me every step of the way.

All my work was supported by the NSF through Grant No. DMR99-72087. Some of the work was carried out in the Center for Microanalysis of Materials (CMM), University of Illinois, which is partially supported by the U.S. Department of Energy under grant DEFG02-91-ER45439.

Table of Contents

Chapter 1

Introduction

Superconductivity has remained an active area of research since the first superconductor was discovered about 100 years ago [1]. In 1957, the Bardeen-Cooper-Schreiffer (BCS) theory was successful in explaining the superconducting properties of conventional superconductors [2]. The BCS theory attributed the attraction between two electrons of a Cooper pair (CP) to the electron-phonon interaction. Since 1987, when the high-temperature superconductor (HTSC) Yttrium-Barium-Copper-Oxide (YBCO) was discovered [3], efforts were made to explain its unusual superconducting properties in the framework of BCS theory, but to little avail. It is now thought that the mechanism of superconductivity in these unconventional superconductors is magnetically-mediated, i.e. due to the interaction between the magnetic moments and the conduction electrons.

The Meissner effect is one of the most striking and fundamental properties of superconductors. It is the ability of the superconductor to expel, from the bulk of the sample, the externally applied magnetic field. This effect can be explained by assuming that, in response to the external magnetic field, circulating (non-dissipative) supercurrents are generated in the system, and the magnetic field induced by these currents cancels exactly the external field in the bulk of the sample. However, in reality, the external magnetic field is still able to penetrate a small distance, of the order of Ångstorms and nanometers, into the superconductor. This distance, which we call the penetration depth (λ), is a direct measure of the density of the superconducting electrons in the superconductor — the superfluid density

ρ_s. λ, and thus ρ_s, vary with temperature, and their temperature-dependences offer strong evidence about the symmetry of the superconducting order parameter (OP). Knowing the symmetry of the OP, $\Delta(\hat{\mathbf{k}})$, is not sufficient to identify the underlying pairing mechanism in a superconductor, but it can certainly help in narrowing down the number of competing microscopic theories of unconventional superconducivity.

In this thesis I present penetration depth data on a number of unconventional superconductors, namely the Heavy-Fermion superconductors (HFSC) $CeCoIn_5$ and $PrOs_4Sb_{12}$; the borocarbide superconductors $RENi_2B_2C$ (RE = Y, Lu, Er, Ho); the spin-triplet superconductor Sr_2RuO_4, and elemental Pb. First I will give a brief account of the theory of penetration depth (Chapter 2) and our experimental setup (Chapter 3). $CeCoIn_5$ (Chapter 4) has attracted much interest due to its similarity with the cuprates: quasi-2D structure and proximity to magnetic order. Yet its superconducting transition temperature T_c is only 2.3 K — much less than that of the cuprates. $PrOs_4Sb_{12}$ (Chapter 5) is another HFSC, yet the mechanism of superconductivity in this material might be due to quadrupolar fluctuations, i.e. non-magnetically mediated, making it the only material whose superconductivity is mediated neither by the electron-phonon, nor magnetic, interactions. The non-magnetic members of the rare-earth borocarbide family, YNi_2B_2C and $LuNi_2B_2C$ (Chapter 6), give glimpses of multi-band behavior, but because of surface effects, we could not make a definitive statement about it. The magnetic members, $ErNi_2B_2C$ (Chapter 7) and $HoNi_2B_2C$ (Chapter 8), show an interesting interplay between magnetism and superconductivity. The work on Sr_2RuO_4 (Chapter 9) is a continuation of previous work done by I. Bonalde and B. Yanoff [4]. We measured the penetration depth of samples with various impurity concentrations, to see how impurities affect the two-band behavior in the purest samples, as proposed by Kusunose and Sigrist [5]. Finally, we show some preliminary results on elemental Pb (Chapter 10), which should show some unusual behavior when the field is applied in the [110] direction, as predicted by Overhauser [6] and seen in phonon dispersion measurements [7]. The work of chapters 6 to 10 is still on-going.

Chapter 2

Penetration Depth

2.1 Some Ideas in Superconductivity

In the BCS theory, the electron-phonon interaction leads to an effective attraction between electrons, and pairs of electrons (called Cooper pairs) are bound together by this attractive interaction. This electron-electron interaction near the Fermi surface (FS) leads to an instability in the usual Fermi distribution. As a result, a different superconducting ground state forms. At $T = 0$, all the carrier electrons go into this ground state, known as the condensate. The condensate is separated from the excited states by an energy gap, $2\Delta(T)$. In other words, the energy gap appears in the one-electron excitation spectrum. These one-electron excitations are called quasiparticles. For there to be enough thermal energy to break one Cooper pair, such that *two* quasiparticles can be *thermally* excited out of the superfluid condensate at a temperature T, the temperature has to be high enough such that $k_B T$ is at least $2\Delta(T)$. The existence of the energy gap for quasiparticle excitations is one of the most well-known predictions of the BCS theory. The quasiparticle energies in a singlet superconducting state are given by

$$E_k = \sqrt{\xi_k^2 + \Delta_k^2}, \tag{2.1}$$

where ξ_k is the normal-state quasiparticle energy measured relative to the chemical potential, and Δ_k is the gap function. The gap function serves the purpose of the order parameter (OP) of the system., i.e. it is non-vanishing only in the superconducting state.

The original BCS theory treated an isotropic system, and the gap function was a single temperature-dependent constant. In a real system, with crystalline anisotropy, the gap function depends on the crystal momentum $\mathbf{k}$. The threshold energy required to break Cooper pairs to create *two* quasipartcles is the minimum value of $2|\Delta(\mathbf{k})|$ on the FS, $2\Delta_{min}$. Note the important distinction between the *gap function*, $\Delta(\mathbf{k})$, and the energy gap for quasiparticle excitations, Δ_{min}.

If the energy gap is isotropic, i.e. constant in magnitude everywhere on the FS, microscopic calculations for a BCS superconductor in this low temperature limit give

$$\frac{\lambda^2(0)}{\lambda^2(T)} \approx 1 - \sqrt{\frac{2\pi\Delta}{k_B T}} \exp^{-\Delta/k_B T} . \tag{2.2}$$

If the energy gap is anisotropic, but the gap is finite and non-zero everywhere, then Δ in Eqn. 2.2 is replaced by Δ_{min}, the minimum value of the gap. We call these superconductors with non-zero energy gap (conventional) s-wave superconductors. If the gap is isotropic in $\mathbf{k}$-space we call it a (conventional) *isotropic* s-wave superconductor. Thus we see that with an energy gap that is non-zero everywhere on the FS, its presence in the excitation spectrum yields exponentially activated behavior at low temperatures.

On the other hand, the symmetries of unconventional states often require that Δ_{min} vanishes. When $\Delta_{min} = 0$, the location on the FS where the gap vanishes is called a *node*. Nodes can be point nodes or line nodes, depending on the nature of the gap function. For example, in a d-wave superconductor with gap function

$$\Delta(\hat{\mathbf{p}}) = \Delta_0(\hat{p}_x^2 - \hat{p}_y^2) \tag{2.3}$$

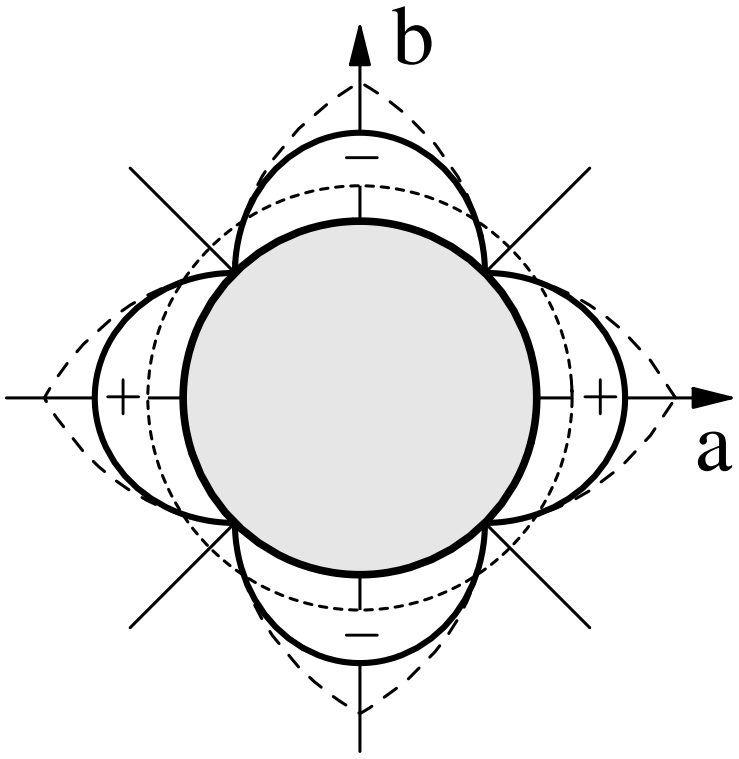

Figure 2.1: Polar plot, in momentum space, of the model order parameter $\Delta(\hat{\mathbf{p}})$ of $d_{x^2-y^2}$ symmetry (thick line). The shaded circle represents the circular Fermi surface. The dashed-line circle, with radius $E_F + T$, represents the maximum energy of the thermally excited quasiparticles; these populate preferentially the nodal regions of the OP. The long-dashed curve is the polar plot of the linear angular expansion of $\Delta(\hat{\mathbf{p}})$ around the four nodes. Taken from Ref. [8].

is called the $d_{x^2-y^2}$-state. A polar plot in momentum space of $\Delta(\hat{\mathbf{p}})$ is shown in Fig. 2.1 (thick line). The OP has four lobes with alternating signs, and vanishes in between, at four nodal points on the FS (shaded circle in Fig. 2.1), along radial directions determined by $\hat{p_x} = \pm\hat{p_x}$ directions, or equivalently at $\phi = \pm\frac{\pi}{2}, \pm\frac{3\pi}{2}$, where ϕ denotes the angle formed by $\hat{\mathbf{p}}$ with the a-axis. We can see from Fig. 2.1 that quasiparticles with energy $E_F + T$ (E_F = Fermi energy) has enough energy to exceed the energy gap near the nodes. If the FS of Fig. 2.1 is a cross-section of a cylindrical FS, then there are lines of nodes running down the c-axis. In terms of the azimuthal angle ϕ the gap function can be rewritten as

$$\Delta(\phi) = \Delta_0 \cos(2\phi). \tag{2.4}$$

A gap function which vanishes on certain parts of the FS leads to low-lying (gapless) excitations in the corresponding energy spectrum; these excitations will dominate the low-temperature physics of the system. Since the gap is anisotropic, the breakup of Cooper pairs is preferential in momentum space and at the lowest temperatures the pairs affected are only those which correspond to electronic momenta oriented close to the nodes of the gap function, i.e. the thermally excited quasiparticles occupy the momentum space preferentially along the nodal directions. In this regime it is convenient to approximate $\Delta(\hat{\mathbf{p}}) = \Delta_0\Phi(\hat{\mathbf{p}})$ by its Taylor expansion with respect to the angular deviation φ of $\hat{\mathbf{p}}$ from the nodal directions in the basal plane, i.e. [8]

$$\Delta(\hat{\mathbf{p}}) \approx \Delta_0\Phi'(0)\varphi \quad \varphi \equiv \phi - \phi_n \in \left[-\frac{\pi}{4}, \frac{\pi}{4}\right], \quad \phi_n = (2n-1)\frac{\pi}{4}, \quad n = 1, 2, 3, 4. \tag{2.5}$$

For this model OP the angular slope of the gap function near a node is $\Phi'(0) = 2$, but Eqn. 2.5 is more general and applicable for *any* unconventional OP with nodes along the θ_n directions, provided that $\Phi'(0)$ does not vanish. The quantity $\Phi'(0)$ is relevant in Chapter 4, where it is related to the prefactor α in the expression for superfluid density $\rho_s = 1 - \alpha T/T_c$.

In contrast to the exponential behavior of s-wave superconductors at low temperatures, in this case we have a power law behavior, i.e. $\Delta(T) \propto T^n$, where the power exponent n depends on the dimensionality of the nodes (point or line, 2D or 3D) *and* the rate at which the gap vanishes in the neighborhood of the nodes [9]. The exponential and power-law behaviors will be derived in subsequent sections.

The total wavefunction describing the superconducting state consists of a spin (S) part and an orbital (L) part. By "singlet" superconductor we mean the two electrons in each Cooper pair have opposite spins, with zero net zero spin ($S = 0$). Thus the spin part of the total wavefunction is odd under exchange of particles. Since the total wavefunction has to be antisymmetric under particle exchange, the orbital part has to be even, i.e. $L =$ even number. $L = 0$ corresponds to an s-wave superconductor, while $L = 2$ corresponds to d-wave. In the next section (Section 2.2) we shall have a fuller discussion of the spin structure of Cooper-paired states.

Finally, note that the existence of nodes depends upon two factors — the topology of the FS and the symmetry of the state. This is a very important point, because even if the symmetry of the superconducting state requires the existence of nodes in the *gap function*, this will only give rise to a vanishing *energy gap* if the gap function happens to vanish *on the FS* [10].

2.2 Spin Structure of Paired States

This section follows closely that of Mineev *et al.* [11]. In all Fermi superfluids known at the present time, Cooper pairs are composed of particles with spin 1/2. The spin component of a pair wave function can be characterized by its total spin $S = 0$ (singlet) or $S = 1$ (triplet).

The orbital wave function is even for even values of orbital angular momentum l and odd for odd values of l:

$$g_l(-\mathbf{k}) = (-1)^l g_l(\mathbf{k}). \tag{2.6}$$

At the same time, according to Pauli's exclusion principle, the total wave function of a pair expressed in the form of a product like $g(\mathbf{k})\chi_{12}$, where χ_{12} is the spin component of the wave function of particles 1 and 2, should change its sign after their permutation (particle exchange):

$$g_l(-\mathbf{k})\chi_{12} = -g_l(\mathbf{k})\chi_{12}. \tag{2.7}$$

It follows from Eqns. 2.6 and 2.7 that the spin component of a paired state with even (odd) orbital angular momentum l should be antisymmetric (symmetric) under the permutation (exchange) of particles.

Spin wave functions of a pair of particles with spin 1/2 are constructed from the one-particle spin wave functions

$$\alpha_\lambda = \begin{pmatrix} 1 \\ 0 \end{pmatrix} = |\uparrow\rangle \quad \text{and} \quad \beta_\lambda = \begin{pmatrix} 0 \\ 1 \end{pmatrix} = |\downarrow\rangle \tag{2.8}$$

which are eigenstates of the operators s^2 and s_z:

$$s_z = \frac{\hbar}{2}\begin{pmatrix} 1 & 0 \\ 0 & -1 \end{pmatrix}, \quad s_z\alpha_\lambda = \frac{\hbar}{2}\alpha_\lambda, \quad s_z\beta_\lambda = -\frac{\hbar}{2}\beta_\lambda. \tag{2.9}$$

The eigenfunction corresponding to the spin-singlet state of a pair, in which $S = 0$ and $S_z = 0$, (where $\mathbf{S} = \mathbf{s}_1 + \mathbf{s}_2$), and is antisymmetric with respect to the particle exchange, has the form

$$\alpha_{1\lambda}\beta_{2\mu} - \beta_{1\lambda}\alpha_{2\mu} = |\uparrow\downarrow\rangle - |\downarrow\uparrow\rangle = \begin{pmatrix} 0 & 1 \\ -1 & 0 \end{pmatrix} = i\sigma_y, \tag{2.10}$$

i.e. it is expressed in terms of the Pauli matrix σ_y. Recall the definition of the Pauli matrices:

$$\sigma_x = \begin{pmatrix} 0 & 1 \\ 1 & 0 \end{pmatrix}, \quad \sigma_y = \begin{pmatrix} 0 & -i \\ i & 0 \end{pmatrix}, \quad \sigma_z = \begin{pmatrix} 1 & 0 \\ 0 & -1 \end{pmatrix}. \tag{2.11}$$

As a result, the total wave function of a pair with $S = 0$ takes the form

$$\Psi^l_{pair} = g(\mathbf{k}) i\sigma_y = \sum_{m=-l}^{l} a_{lm} Y_l^m(\hat{\mathbf{k}}) i\sigma_y, \tag{2.12}$$

where l takes the values 0, 2, 4, ... The respective pair states are labelled, as is traditional in atomic physics, by letters s, d, g, ...

The complex coefficients a_{lm} in Eqn. 2.12, same for all Cooper pairs of a given superconducting state, represent the *superconductor order parameter*. In non-uniform states the order parameter depends on the coordinates, i.e. a_{lm} are functions of $\mathbf{r}$. For example, the order parameter for a s-wave superconductor is expressed by a single complex function

$$a_{00}(\mathbf{r}) = \psi(\mathbf{r}) = |\psi| e^{i\phi} \tag{2.13}$$

whereas in a d-wave superconductor ($l = 2$) the order parameter includes five complex functions.

In the case of the triplet state of a pair ($S = 1$), the wave functions corresponding to the three different spin projections on the quantization axis, which are symmetric under particle exchange can be written as

$$S_z = \begin{cases} 1, & \alpha_{1\lambda}\alpha_{2\mu} = |\uparrow\uparrow\rangle = \begin{pmatrix} 1 & 0 \\ 0 & 0 \end{pmatrix}, \\ 0, & \alpha_{1\lambda}\beta_{2\mu} + \beta_{1\lambda}\alpha_{2\mu} = |\uparrow\downarrow\rangle + |\downarrow\uparrow\rangle = \begin{pmatrix} 0 & 1 \\ 1 & 0 \end{pmatrix}, \\ -1, & \beta_{1\lambda}\beta_{2\mu} = |\downarrow\downarrow\rangle = \begin{pmatrix} 0 & 0 \\ 0 & 1 \end{pmatrix}, \end{cases} \tag{2.14}$$

i.e. they are symmetric matrices. The total wave function of a pair is a linear combination of these states:

$$\Psi^l_{pair} = g_1(\mathbf{k})|\uparrow\uparrow\rangle + g_2(\mathbf{k})(|\uparrow\downarrow\rangle + |\downarrow\uparrow\rangle) + g_3(\mathbf{k})|\downarrow\downarrow\rangle = \begin{pmatrix} g_1(\mathbf{k}) & g_2(\mathbf{k}) \\ g_2(\mathbf{k}) & g_3(\mathbf{k}) \end{pmatrix} \tag{2.15}$$

Here

$$g_\alpha(\mathbf{k}) = \sum_{m=-l}^{l} a^\alpha_{lm} Y^m_l(\hat{\mathbf{k}}) \qquad \alpha = 1, 2, 3 \tag{2.16}$$

are the amplitudes of states with $S_z = 1$, 0 and -1, respectively.

The quantum number l in Eqn. 2.16 can be equal to 1, 3, ... The respective states are called p, f, ...-wave superconducting states. Another form of Eqn. 2.16 is obtained using the basis of the symmetric matrices $i\boldsymbol{\sigma}\sigma_y = (i\sigma_x\sigma_y, i\sigma_y\sigma_y, i\sigma_z\sigma_y)$. We have

$$\begin{aligned} \Psi^l_{pair} &= i(\mathbf{d}(\mathbf{k})\boldsymbol{\sigma})\sigma_y = (d_x(\mathbf{k})\sigma_x, d_y(\mathbf{k})\sigma_y, d_z(\mathbf{k})\sigma_z)i\sigma_y \\ &= \begin{pmatrix} -d_x(\mathbf{k}) + id_y(\mathbf{k}) & d_z(\mathbf{k}) \\ d_z(\mathbf{k}) & d_x(\mathbf{k}) + id_y(\mathbf{k}) \end{pmatrix}. \end{aligned} \tag{2.17}$$

The components of the vector $\mathbf{d}(\mathbf{k})$, which are linearly related to the amplitudes $g_\alpha(\mathbf{k})$ through the equalities

$$g_1 = -d_x + id_y, \quad g_2 = d_z, \quad g_3 = d_x + id_y, \tag{2.18}$$

can be expanded in terms of the spherical harmonics:

$$d_\alpha(\mathbf{k}) = \sum_{m=-l}^{l} b^\alpha_{lm} Y^m_l(\hat{\mathbf{k}}). \tag{2.19}$$

The coefficients b^α_{lm} play the role of the order parameter in a superconductor with a particular type of pairing, i.e. with a given value of quantum number l. So, in the simplest case of

p-wave pairing, the order parameter is expressed as a set of nine complex functions b_{lm}^{α} (m = -1,0,1; α = x,y,z).

We shall illustrate the $l = 1$ case. The spherical harmonics $Y_l^m(\hat{\mathbf{k}})$ with $l = 1$ can be expressed as linear functions of the vector $\hat{\mathbf{k}}$,

$$Y_1^1(\hat{\mathbf{k}}) \sim \hat{k}_x + i\hat{k}_y, \quad Y_1^{-1}(\hat{\mathbf{k}}) \sim \hat{k}_x - i\hat{k}_y, \quad Y_1^0(\hat{\mathbf{k}}) \sim \hat{k}_z \tag{2.20}$$

which allows one to write the vector $\mathbf{d}$ of Eqn. 2.19 in a different form:

$$d_\alpha(\mathbf{k}) = A_{\alpha i}\hat{k}_i. \tag{2.21}$$

The complex 3×3 matrix $A_{\alpha i}$ is the order parameter in superfluid p-wave Fermi liquids. This is the type of pairing which takes place in superfluid ^{3}He [12]. A few possible phases of superfluid p-wave liquid distinguished by the configurations of the spin vector $\mathbf{d}$ (or matrix $A_{\alpha i}$) are listed below.

For the B-phase of superfluid ^{3}He,

$$\mathbf{d}(\mathbf{k}) \sim \hat{\mathbf{k}} \qquad \text{(B-phase)}, \tag{2.22}$$

i.e. $A_{\alpha i} \sim \delta_{\alpha i}$ (in an arbitrary reference frame $A_{\alpha i} \sim R_{\alpha i}$, where $\hat{R}$ is the matrix of three-dimensional rotations). The pair wave function (Eqn. 2.17) takes the form

$$\begin{aligned}
\Psi_{pair}^B &\sim \begin{pmatrix} -\hat{k}_x + i\hat{k}_y & \hat{k}_z \\ \hat{k}_z & \hat{k}_x + i\hat{k}_y \end{pmatrix} \\
&= (-\hat{k}_x + i\hat{k}_y)|\uparrow\uparrow\rangle + \hat{k}_z(|\uparrow\downarrow\rangle + |\downarrow\uparrow\rangle) + (\hat{k}_x + i\hat{k}_y)|\downarrow\downarrow\rangle \\
&\sim -Y_1^{-1}|S_z = 1\rangle + Y_1^0|S_z = 0\rangle + Y_1^1|S_z = -1\rangle.
\end{aligned} \tag{2.23}$$

Thus, the B-phase is described by a linear combination of three equiprobable states $|S_z = +1, m = -1\rangle$, $|S_z = 0, m = 0\rangle$, and $|S_z = -1, m = +1\rangle$. Note that S_z refers to the *spin* part of the pair wave function, while m (as well as l) refers to the *orbital* part of the pair wave function.

For the A-phase of superfluid ^{3}He,

$$\mathbf{d}(\mathbf{k}) \sim (\hat{k}_x + i\hat{k}_y, 0, 0) \qquad \text{(A-phase)}, \tag{2.24}$$

the pair wave function has the form

$$\Psi^A_{pair} \sim (\hat{k}_x + i\hat{k}_y) \begin{pmatrix} -1 & 0 \\ 0 & 1 \end{pmatrix} \sim (\hat{k}_x + i\hat{k}_y)(|\uparrow\uparrow\rangle - |\downarrow\downarrow\rangle). \tag{2.25}$$

Thus the A-phase is a linear combination of two equiprobable states $|S_z = +1, m = 1\rangle$ and $|S_z = -1, m = 1\rangle$.

To summarize, the pair spin wave function of a state with even parity (s: singlet)

$$\Psi^s_{pair} \sim g(\mathbf{k}) i\sigma_y, \tag{2.26}$$

$$g(\mathbf{k}) = g(-\mathbf{k}), \tag{2.27}$$

corresponds to $S = 0$, and that of a state with odd parity to $S = 1$, i.e. (t: triplet)

$$\Psi^t_{pair} \sim (\mathbf{d}(\mathbf{k})\boldsymbol{\sigma}) i\sigma_y, \tag{2.28}$$

$$\mathbf{d}(\mathbf{k}) = -\mathbf{d}(-\mathbf{k}). \tag{2.29}$$

The superconducting gap function for the singlet and triplet case is given by

$$\Delta^s_{k,\alpha\beta} = \Delta g(\mathbf{k})(i\sigma_y)_{\alpha\beta}, \tag{2.30}$$

$$\Delta^t_{k,\alpha\beta} = \Delta \mathbf{d}(\mathbf{k})(i\boldsymbol{\sigma}\sigma_y)_{\alpha\beta} \tag{2.31}$$

respectively. Δ is the $\mathbf{k}$-independent part of the gap. In the case of a superconductor with singlet pairing, we have for the quasiparticle excitation energy

$$E_{\mathbf{k}} = \sqrt{\xi_k^2 + \Delta^2 |g(\mathbf{k})|^2}, \tag{2.32}$$

i.e. the spectrum of elementary excitations has a gap. In the triplet case, if $\mathbf{d}$ is *unitary* it can be shown that

$$E_{\mathbf{k}} = \sqrt{\xi_k^2 + \Delta^2 |\mathbf{d}(\mathbf{k})|^2}. \tag{2.33}$$

If $\mathbf{d}$ is *non-unitary*, the excitation spectrum generalizes to

$$E_{\mathbf{k},\pm} = \sqrt{\xi_k^2 + \Delta^2 (|\mathbf{d}(\mathbf{k})|^2 \pm |\mathbf{d}^*(\mathbf{k}) \times \mathbf{d}(\mathbf{k})|)}, \tag{2.34}$$

i.e. if $\mathbf{d}$ is non-unitary then $\mathbf{d}^*$ points in a different direction than $\mathbf{d}$ and their cross-product is non-zero. The excitation spectrum splits into two branches for the plus and minus cases. The cross-product term can be taken as a measure of the non-unitarity of the order parameter. When $\mathbf{d}$ is maximally non-unitary $|\mathbf{d}^*(\mathbf{k}) \times \mathbf{d}(\mathbf{k})| = |\mathbf{d}|^2$ and the gap of the minus branch of the excitation spectrum vanishes.

In Chapter 5 we will find that the gap structure of $PrOs_4Sb_{12}$ is analogous to the A-phase of ^{3}He. Later in Chapter 9, we will look into the various thermodynamic and electrodynamic properties of the spin-triplet superconductor Sr_2RuO_4, and find that the gap that opens up on the active γ-band is also analogous to the A-phase of ^{3}He.

2.3 Basic Theory of Penetration Depth

Suppose I have an uniform external magnetic field $\mathbf{H}$ applied in the x direction, parallel to the surface of a superconductor, such that $H_x = H_x(z)$, and z is the coordinate perpendicular to

the surface. Starting from the Josephson relation between the current density $\mathbf{j}$ and applied vector potential $\mathbf{A}$ for a superfluid density n_s, we have

$$\mathbf{j} = -\frac{n_s e^2}{m^* c}\mathbf{A}, \tag{2.35}$$

where m^* is the effective mass of the charge carriers. We can combine it with Maxwell's equations to find

$$\nabla^2 \mathbf{B} = \frac{4\pi n_s e^2}{m^* c^2}\mathbf{B}. \tag{2.36}$$

Since $B_x = B_x(z)$, we have

$$\frac{d^2}{dz^2}B_x = \frac{1}{\lambda^2}B_x, \tag{2.37}$$

where we define the *London penetration depth*

$$\lambda = \left(\frac{4\pi n_s e^2}{m^* c^2}\right)^{-1/2}. \tag{2.38}$$

The solution to equation (2.37) has the form

$$B_x(z) = H_x(0) exp(-z/\lambda), \tag{2.39}$$

and we see that the field penetrates into the sample a distance of order λ. If the field were to remain constant to a certain depth and then suddenly vanish, this depth would be just λ (this variation is of course implausible, but is sometimes useful as a crude assumption for qualitative arguments). From Eqn. 2.38 we see that λ provides a means of measuring n_s/m^*, the ratio of the superfluid density to the effective mass of the charge carriers.

Let us consider a particular configuration — an infinite slab of thickness $2d$ placed in a uniform applied magnetic field H_0 parallel to its surface. Assume that the plane $z = 0$ is in the center of the slab and that its surfaces coincide with the planes $z = \pm d$. The magnetic field is along the x axis.

In the interior of the slab, the magnetic field B must satisfy Eqn. 2.36. Then, from symmetry arguments, B is along the x-axis and depends only on the z coordinate. Therefore Eqn. 2.36 can be rewritten as Eqn. 2.37, with the boundary conditions $B(\pm d) = H_0$. The general solution of Eqn. 2.37 is [13]

$$B(z) = B_1 \cosh(z/\lambda) + B_2 \sinh(z/\lambda), \tag{2.40}$$

where B_1 and B_2 are integration constants. Substituting the boundary conditions into Eqn. 2.40, we get two algebraic equations with two unknowns that can be solved. The final result is

$$B(z) = H_0 \frac{\cosh(z/\lambda)}{\cosh(d/\lambda)}. \tag{2.41}$$

Later in Section 3.4 we shall extend Eqn. 2.41 to the case when (1) the applied field is oriented perpendicular to the sample basal plane, i.e. in the z-direction, and (2) the sample has finite dimensions in the x and y directions.

2.4 Quasiparticle Density of States (QDOS)

This section also follows closely the approach of Mineev *et al.* [11]. The single-(quasi)particle density of states (QDOS) is, by definition,

$$N(E) = \sum_{\mathbf{k}} \delta(E - E_k). \tag{2.42}$$

Using the expression for quasiparticle energy in Eqn. 2.1 for the excitation spectrum, we obtain from Eqn. 2.42

$$\begin{aligned} N(E) &= \int \frac{d^3k}{(2\pi)^3} \delta(E - E_k) = N_0 \int \frac{d\Omega}{4\pi} \int d\xi \delta(E - E_k) \\ &= N_0 \int \frac{d\Omega}{4\pi} \int \frac{dE' E'}{\sqrt{E'^2 - \Delta_k^2}} \delta(E - E') = N_0 \int \frac{d\Omega}{4\pi} \frac{E}{\sqrt{E^2 - \Delta_k^2}}, \end{aligned} \tag{2.43}$$

where N_0 is the density of states (DOS) at the Fermi level in the normal state per one spin projection, and the integration over angles is performed within the limits $\Delta_k^2 < E^2$. Eqn. 2.43 is the working equation for calculating the QDOS for any arbitrary gap function. We will use it extensively in Chapter 5, where we calculated the QDOS, and hence superfluid density ρ_s, for several candidate gap functions for $PrOs_4Sb_{12}$.

It follows from Eqn. 2.43 that for a conventional isotropic s-wave superconductor ($\Delta_k = \Delta$),

$$N(E) = N_0 \begin{cases} 0 & (E < \Delta) \\ \frac{E}{\sqrt{E^2-\Delta^2}} & (E > \Delta) \end{cases}, \tag{2.44}$$

i.e. the density of quasiparticle states drops abruptly to zero for $E < \Delta$.

For a d-wave superconductor, $\Delta_k = \Delta_0 \cos(2\phi)$. So the d-wave QDOS is

$$\begin{aligned} \frac{N(E)}{N_0} &= \int_0^{2\pi} \frac{d\phi}{2\pi} \frac{E}{\sqrt{E^2 - \Delta_k^2}} \\ &= \int_0^{2\pi} \frac{d\phi}{2\pi} \frac{E}{\sqrt{E^2 - \Delta_0^2 cos^2(2\phi)}}. \end{aligned} \tag{2.45}$$

The last integral is a complete elliptic integral of the first kind, and can be looked up in Gradsteyn or computed with Mathematica or Mathcad code for the full range of values of E/Δ_0. The result is

$$\frac{N(E)}{N_0} = \begin{cases} \frac{2}{\pi}\frac{E}{\Delta_0}\kappa(\frac{E}{\Delta_0}) & (E < \Delta_0) \\ \frac{2}{\pi}\kappa(\frac{\Delta_0}{E}) & (E > \Delta_0). \end{cases} \tag{2.46}$$

For small argument ($E \ll \Delta_0$), $\kappa(\frac{E}{\Delta_0}) \approx \frac{\pi}{2}$, so

$$\frac{N(E)}{N_0} \approx \frac{E}{\Delta_0} \quad (E \ll \Delta_0). \tag{2.47}$$

Eqn. 2.47 applies to any gap with line nodes, for example, the d-wave gap of the cuprates, or the polar phase of ^{3}He.

In general, for point and line nodes in 3D and point nodes (the only possibility) in 2D, we have for E $\ll \Delta_0$ (or T $\ll$ T$_c$)

$$N(E) \propto \begin{cases} E^2 & \text{(3D point node)} \\ E & \text{(3D line node)} \\ E & \text{(2D point node)} \end{cases} . \tag{2.48}$$

Such a power-law dependence of the QDOS results in power-law (not exponential) temperature dependences of thermodynamic and kinetic characteristics of unconventional superconductors.

Note that in Eqn. 2.48, the conclusion $N(E) \propto E$ in a *d*-wave superconductor with gap function given by Eqn. 2.4 is dependent upon the fact that there is a *linear* dispersion of the gap in the neighborhood of the nodes (i.e. $\Delta(\phi) \propto \phi$ near the nodes), since the gap function is a sinusoidal one. The same applies to a point-node gap. The next question is: if $\Delta(\phi) \propto \phi^x$ near the nodes, then what is the relationship between $N(E)$ and E?

Let $\Delta(\phi) = \Delta_0 \phi^x$. Then from Eqn. 2.43,

$$\frac{N(E)}{N_0} = \int_0^{\frac{E}{\Delta_0}^{1/x}} \frac{d\phi}{2\pi} \frac{E}{\sqrt{E^2 - \Delta_0 \phi^{2x}}}, \tag{2.49}$$

where the upper limit of the integral comes from the condition $E^2 - \Delta_0 \phi^{2x} > 0$. Changing to a dimensionless variable $u = E/\Delta_0$, we get

$$\begin{aligned} \frac{N(E)}{N_0} &= \int_0^{\left(\frac{E}{\Delta_0}\right)^{1/x}} \frac{d\phi}{2\pi} \frac{E/\Delta_0}{\sqrt{\left(\frac{E}{\Delta_0}\right)^2 - \phi^{2x}}} \\ &= \int_0^{u^{1/x}} \frac{d\phi}{2\pi} \frac{u}{\sqrt{u^2 - \phi^{2x}}}. \end{aligned} \tag{2.50}$$

We perform another change of variable $\phi^x = u \sin\theta$, then

$$\begin{aligned} \frac{N(E)}{N_0} &= \int_0^{\pi/2} \frac{u^{1/x}}{x} (\sin\theta)^{-\frac{x-1}{x}} d\theta \\ &\propto u^{1/x} = \left(\frac{E}{\Delta_0}\right)^{\frac{1}{x}}. \end{aligned} \tag{2.51}$$

The conclusion is thus: *when* $\Delta(\phi) \propto \phi^x$ *near the nodes, then* $N(E) \propto E^{1/x}$.

2.5 Derivation of Superfluid Density and Penetration Depth from QDOS

The temperature dependence of the superfluid density n_s can be calculated from QDOS. The normal fluid density (i.e. number of quasiparticle excitations) in a superconductor at temperature T is [14]

$$n_n = n \int_{-\infty}^{\infty} d\xi \left(-\frac{\partial f}{\partial E_k}\right), \tag{2.52}$$

where $E_k = \sqrt{\xi_k^2 + \Delta_k^2}$ is the Bogoliubov quasiparticle energy, f is the Fermi function. Assuming that a two-fluid description holds, we have $n = n_n + n_s$, the density of superconducting electrons in the limit $T \to 0$, as well as of normally conducting electrons above T_c.

From Eqn. 2.52, the *normalized* superfluid density $\rho_s \equiv n_s/n$ is

$$\rho_s = 1 + 2 \left\langle \int_0^{\infty} \frac{\partial f}{\partial E} d\xi \right\rangle_{FS}, \tag{2.53}$$

or, in terms of E,

$$\begin{aligned} \rho_s &= 1 + 2 \left\langle \int_0^{\infty} dE \frac{N(E)}{N_0} \frac{\partial f}{\partial E} \right\rangle_{FS} \\ &= 1 + 2 \left\langle \int_0^{\infty} \frac{E dE}{\sqrt{E^2 - \Delta_k^2}} \frac{\partial f}{\partial E} \right\rangle_{FS}, \end{aligned} \tag{2.54}$$

where $\langle ... \rangle_{FS}$ denotes the average over the FS, which entails another integral over the solid angle $\mathrm{d}\Omega/4\pi$. Equations 2.53 and 2.54 are applicable for all gap functions Δ_k in the pure local limit. *These equations, together with Eqn. 2.43, are the working equations for calculating QDOS and ρ_s for any arbitrary gap function Δ_k.*

For an s-wave superconductor at $T \ll T_c$, the normal fluid density, after integrating Eqn. 2.52 by parts, we get for $T \ll T_c$

$$n_n(T) = n\sqrt{\frac{2\pi\Delta(0)}{k_B T}} exp\left(-\frac{\Delta(0)}{k_B T}\right) \quad (T \ll T_c), \tag{2.55}$$

where $\Delta(0)$ is the magnitude of the superconducting gap at $T = 0$.

Hence

$$\begin{aligned} \rho_s(T) &= \frac{n_s(T)}{n} = \frac{n - n_n(T)}{n} = 1 - \frac{n_n(T)}{n} \\ &= 1 - \sqrt{\frac{2\pi\Delta(0)}{k_B T}} exp\left(-\frac{\Delta(0)}{k_B T}\right) \quad (T \ll T_c). \end{aligned} \tag{2.56}$$

So we have essentially an $\exp(-\Delta/\mathrm{T})$ behavior of the superfluid density when $T \ll T_c$. From Eqn. 2.38 we can write

$$\rho_s(T) = \frac{\lambda^2(0)}{\lambda^2(T)}, \tag{2.57}$$

where $\lambda(0)$ is the penetration depth at $T \to 0$. Therefore the penetration depth is given by

$$\begin{aligned} \lambda(T) &= \left(\frac{4\pi(n - n_n)e^2}{mc^2}\right)^{-1/2} \\ &\approx \lambda(0)\left[1 + \sqrt{\frac{\pi\Delta(0)}{2k_B T}} exp\left(-\frac{\Delta(0)}{k_B T}\right)\right] \quad (s\text{-wave}, T \ll T_c). \end{aligned} \tag{2.58}$$

For the line-node case,

$$n_n = n\int_0^{2\pi} \frac{d\phi}{2\pi} \int_{-\infty}^{\infty} d\xi \left(-\frac{\partial f}{\partial E_k}\right) = 2n\int_0^{\infty} dE \frac{N(E)}{N_0}\left(-\frac{\partial f}{\partial E}\right), \tag{2.59}$$

	3D point node	3D line node
Penetration depth λ	T^2	T
Specific heat C_s	T^3	T^2
NMR relaxation $1/T_1$	T^5	T^3
Thermal conductivity κ	T^3	T^2

Table 2.1: Theoretical temperature dependencies for low-temperature measurements, assuming a spherical Fermi surface and either line of point nodes in the superconducting gap function. Taken from Ref. [15].

which, after substituting for the QDOS from Eqn. 2.47, gives

$$n_n \approx 2n \ln 2 \frac{T}{\Delta_0} \qquad (T \ll T_c). \tag{2.60}$$

Thus

$$\lambda(T) \approx \lambda(0) \left(1 + \ln 2 \frac{T}{\Delta_0}\right) \quad \text{(line node, } T \ll T_c\text{)}, \tag{2.61}$$

or

$$\lambda(T) - \lambda(0) \propto T \qquad \text{(line node, } T \ll T_c\text{)}. \tag{2.62}$$

In general,

$$\lambda(T) \propto \begin{cases} T^2 & \text{(3D point nodes)} \\ T & \text{(3D line nodes or 2D point nodes)} \end{cases}. \tag{2.63}$$

Thus we see a fundamental difference between the asymptotic behavior ($T \ll T_c$) of superconductors with and without nodes on the FS: At the lowest temperatures $\lambda(T)$ obeys an exponential law for nodeless superconductors, and a power law for nodal ones. Other thermodynamic quantities also display a similar difference. One can easily verify that other thermodynamic quantities also vary according to a power law as $T \to 0$, for example, in the electronic specific heat C_s, NMR relaxation rate $1/T_1$ and thermal conductivity κ. Table 2.1 shows the power exponent of some thermodynamic quantities in the $T \to 0$ limit. In the case of specific heat one has to subtract the phonon contribution from the raw data, which is a tedious and at times ambiguous process, whereas for penetration depth one is directly

measuring the superfluid part of the response. Therefore penetration depth is a very direct way of probing the pairing symmetry of a superconductor. In subsequent chapters we call ρ_s the "superfluid density", dropping the word "normalized".

Once again, we wish to stress that the temperature exponents in Table 2.1 are derived for sinusoidal gap functions, i.e. near the nodes, the gap disperses linearly away from the nodes. The temperature exponent depends not only on the dimensionality of the nodes (i.e. points, lines, etc), but also on the rate at which the gap vanishes in the neighborhood of the nodes [9]. In a similar spirit to the end of Section 2.4, we now answer the question: if $N(E) \propto E^x$, then what is the power exponent in the expression for ρ_s?

Let $N(E) \propto E^x$, then from Eqn. 2.54

$$\begin{aligned}
\rho_n &\propto \left\langle \int_0^\infty dE \frac{N(E)}{N_0} \frac{\partial f}{\partial E} \right\rangle_{FS} \\
&\propto \left\langle \int_0^\infty dE E^x \frac{\partial f}{\partial E} \right\rangle_{FS} \\
&\propto \int_0^\infty dE \frac{E^x}{T} \frac{e^{E/T}}{(e^{E/T}+1)^2} \\
&= \int_0^\infty dE \frac{E^x}{T} \frac{1}{(e^{E/2T}+e^{-E/2T})^2} \\
&= \int_0^\infty dE \frac{E^x}{4T} \frac{1}{\cosh^2\left(\frac{E}{2T}\right)}.
\end{aligned} \tag{2.64}$$

We change to a dimensionless variable $u = E/2T$, then

$$\begin{aligned}
\rho_n &\propto \int_0^\infty du (2T) \frac{y}{4T} (2uT)^x \frac{1}{\cosh^2 u} \\
&\propto T^x.
\end{aligned} \tag{2.65}$$

Our conclusion is thus: *if $N(E) \propto E^x$, then $\rho_n \propto T^x$, and hence $\rho_s \sim T^x$ also.* The next question to ask is: since $\rho_s(T) = \lambda^2(0)/\lambda^2(T)$, does ρ_s and λ exhibit the same power exponent?

Let us take the d-wave model for illustration purposes. In the d-wave model, even if ρ_s varies strictly with T, i.e. $\rho_s = 1 - \alpha T/T_c$, the penetration depth is non-linear:

$$\lambda(T) = \lambda(0)\left[1 + \frac{1}{2}\left(\frac{\alpha T}{T_c}\right) + \frac{3}{8}\left(\frac{\alpha T}{T_c}\right)^2 + ...\right]. \tag{2.66}$$

Hence there is always a quadratic component to λ (for example in Eqn. 2.61) whose strength depends on α, which in the d-wave model, is inversely proportional to $d\Delta(\phi)/d\phi|_{node}$, the angular slope of the energy gap at the nodes [16]. Therefore, strictly speaking, for a d-wave superconductor, it is ρ_s, *not* λ, that should be linear, and one should always convert λ to ρ_s before making any conclusions. Fortunately, α is small enough that the quadratic component can usually be ignored. In this thesis we will convert λ to ρ_s whenever possible, and analyze the ρ_s data.

2.6 Perturbing Effects

From the previous sections, for a superconductor with line nodes, e.g. a d-wave superconductor, the low-temperature penetration depth should give a linear temperature-dependence. However, earlier measurements on the cuprates show a crossover from linear to quadratic behavior at the lowest temperatures [17]. There is now general consensus that the quadratic behavior is due to resonant impurity scattering [18]. Later measurements on very clean YBCO single crystals did yield the expected linear behavior down to 3 K [19]. Recently however, Kosztin and Leggett [20, 8] proposed that since the coherence length diverges near the nodes, the quadratic behavior seen in the cuprates is due to nonlocal corrections to the penetration depth, not impurities. They also suggested that the actual temperature dependence of the penetration depth in the $T \to 0$ limit is quadratic and not linear.

2.6.1 Resonant Impurity Scattering

In Hirschfeld and Goldenfeld's (HG) Resonant Impurity Scattering (RIS) model [18], they proposed that the dominant scattering mechanism in thin films and single crystals of YBCO is resonant scattering, not Born scattering. If the scattering responsible for the change in power law of the penetration depth were Born scattering, there would be a large suppression of T_c, which is not observed. For a *pure* superconductor in a d-wave-like state at temperatures well below T_c, the deviation $\Delta\lambda$ of the penetration depth from its zero-temperature value $\lambda(0)$ is proportional to T. However, when the concentration n_{imp} of strongly scattering impurities is nonzero, $\Delta\lambda(T) \propto T^n$, where $n = 2$ for $T < T^*_{imp} \ll T_c$ and $n = 1$ for $T^*_{imp} < T \ll T_c$.

In the RIS model, the scattering rate parameter

$$\Gamma = \frac{n_{imp} n}{\pi N_0} \tag{2.67}$$

is dependent only on the impurity concentration n_{imp}, the electron density n, and the normal-state density of states N_0. In the strong-scattering limit, a relatively small concentration of defects can lead to a substantial residual density of states, within a range where the relative T_c suppression $(T_{c0}-T_c)/T_{c0}$ is of order $\Gamma/\Delta_0 \ll 1$. Here Δ_0 is the maximum superconducting gap amplitude, and T_{c0} is the superconducting transition temperature in the purest sample. HG estimated that resonant defect concentrations of order 1% would lead to gapless behavior ($\Delta\lambda \sim T^2$) over a temperature range T^* of order 10% of T_c, but negligible ($< 1\%$) T_c suppression. Concentrations of order 0.1% would also lead to negligible T_c suppression, and the gapless range would be restricted to temperatures below 2–3% of T_c, below the lowest temperatures where penetration depth experiments on HTSC have been measured.

In the strong-scattering limit, one obtains for the crossover temperature

$$T^*_{imp} \approx \frac{6 \ln 2\gamma}{\pi}, \tag{2.68}$$

where $\gamma \sim \sqrt{\Gamma\Delta_0}$. In the low-defect-concentration limit $\Gamma/\Delta_0 \ll 1$, $\gamma \approx 0.63\sqrt{\Gamma\Delta_0}$, it becomes (taking $\hbar = k_B = 1$)

$$T^*_{imp} \approx 0.83\sqrt{\Gamma\Delta_0}, \tag{2.69}$$

or, if one puts in $\hbar$ and k_B explicitly, Eqn. 2.69 becomes

$$T^*_{imp} \approx 0.83\frac{\sqrt{\hbar\Gamma\Delta_0}}{k_B}. \tag{2.70}$$

Experimentally, we can estimate the *experimental* crossover temperature T^*_{expt} from the superfluid density data by using the interpolation formula

$$\rho_s(T) = 1 - \frac{\alpha T^2/T_c}{T^*_{expt} + T}, \tag{2.71}$$

where α and T^*_{expt} are parameters to be varied.

2.6.2 Nonlocal Corrections to Penetration Depth

This subsection follows closely the Ph.D thesis of Ioan Kosztin [8]. Under certain conditions, the very low temperature behavior of the electromagnetic penetration depth $\lambda(T)$ of a pure d-wave superconductor (or any anisotropic superconductor with nodes in the gap) is determined by nonlocal electrodynamics. The physical reason for this is as follows. The low temperature properties of an anisotropic superconductor, with nodes in the gap on the FS, are determined by the low-lying (gapless) excitations, which are located in the vicinity of the nodes. On the other hand, the effective coherence length (proportional to the inverse of the anisotropic gap function) corresponding to these low lying excitations is very large and, sufficiently close to the nodes, it may well exceed the value of the London penetration depth. Therefore, it is necessary to use nonlocal electrodynamics to properly account for the contribution of the low-lying excitations to the temperature dependence of the penetration depth in these superconductors. The results is that, contrary to the general belief,

the low-temperature deviation $\Delta\lambda(T)$ of $\lambda(T)$ from its zero-temperature value $\lambda(0)$ varies quadratically and *not* linearly with the temperature. The crossover temperature T^*_{NL} below which nonlocal electrodynamics is dominant is

$$T^*_{NL} = \Delta_0 \frac{\xi_0}{\lambda_0}, \tag{2.72}$$

where Δ_0 is the (maximum) amplitude of the anisotropic gap function, ξ_0 is the corresponding coherence length, and λ_0 is the zero-temperature London penetration depth.

In contrast to the penetration depth, which can be measured more or less directly, the coherence length ξ_0 cannot be determined experimentally and, in fact, is estimated in terms of the maximum value of the anisotropic gap function $\Delta_0 = \max\{\Delta(\hat{\mathbf{p}})\}$ by using the usual BCS expression $\xi_0 = v_F/\pi\Delta_0$ ($\xi_0 = \hbar v_F/\pi\Delta_0$ in SI units). Thus, in the case of a clean, anisotropic superconductor it is more appropriate to introduce an anisotropic coherence length $\xi(\hat{\mathbf{p}}) \equiv v_F/\pi\Delta(\hat{\mathbf{p}})$. If the anisotropic OP has nodes on the FS, it is clear that sufficiently close to the nodes $\xi(\hat{\mathbf{p}}) > \lambda$, and therefore, the contribution of these regions of the FS to the penetration depth $\lambda(T)$ must be determined by using nonlocal electrodynamics. How large the value of λ_0/ξ_0 is determines how small a fraction of the FS, of order $\alpha_0 \equiv \xi_0/\lambda_0$, violates the applicability of local electrodynamics. Since the whole FS contributes to the zero temperature penetration depth $\lambda(0)$, one expects no significant nonlocal corrections to this quantity. On the other hand, the low temperature dependence of $\lambda(T)$ must be dominated by nonlocal effects because this dependence is determined by only a small region of the FS concentrated around the nodes of the OP. The crossover temperature below which nonlocal effects are important is given by $T^*_{NL} = \alpha_0\Delta_0$. For $T \gg T^*_{NL}$ the local limit is applicable. Around T^*_{NL}, however, the crossover from linear to quadratic may not be so obvious, and so one has to use the interpolation formula (Eqn. 2.71) to estimate T^*_{expt} either from $\Delta\lambda(T)$ or superfluid density (ρ_s) data. As a typical example consider a YBCO single crystal with $\Delta_0 \approx 250$ K, $\xi_0 \approx 14$ Å, and $\lambda_0 \approx 1400$ Å; this gives $\alpha_0 \approx 10^{-2}$ and $T^*_{NL} \approx 2.5$ K. Thus nonlocality represents

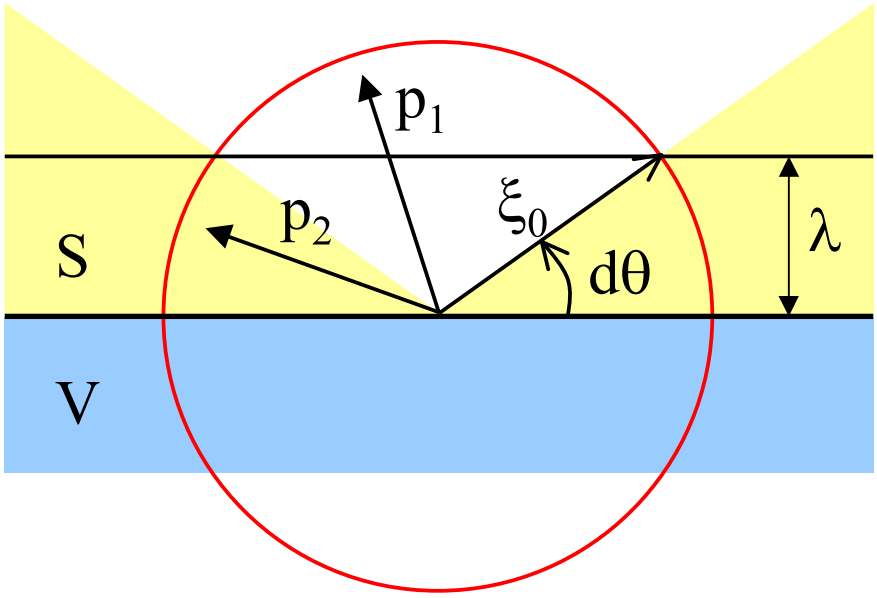

Figure 2.2: Pippard limit for an s-wave superconductor. S = superconductor, V = vacuum. Taken from Ref. [8].

a second possible mechanism, beside strongly scattering impurities, that may account for the experimentally observed deviation from the linear T-dependence of the penetration depth at the lowest measured temperatures in nominally clean HTSC.

Besides rigorously deriving the T^2 behavior, Kosztin [8] also put forward a qualitative argument, called the *inefficiency concept* [21], to explain the influence of nonlocality on the magnetic penetration depth in the extreme nonlocal limit, also known as the Pippard limit, characterized by $\xi_0 \gg \lambda$. We also checked the validity of this qualitative explanation with Professor A. Leggett.

In conventional superconductors, the basic idea is to apply for the magnetic penetration depth the same formula as in the local limit but with the density of the Cooper pairs n replaced by an effective density n_{eff} which takes into consideration the fact that even at zero temperature not all the carriers participate effectively in screening out the magnetic

field from the bulk of the superconducting sample. If one denotes $\lambda \equiv \lambda_P$ the penetration depth in the Pippard limit, then one can write

$$\frac{\lambda_P}{\lambda_0} = \sqrt{\frac{n}{n_{eff}}}, \tag{2.73}$$

where n is once again the total electron density in the superconductor.

To estimate n_{eff} consider the situation depicted in Fig. 2.2 where the circle represents the spatial extent $\sim \xi_0$ of a Cooper pair which is scattered from the plane superconductor-vacuum boundary. Since $\xi_0 \gg \lambda$ it is clear that Cooper pairs with momentum $\mathbf{p}_1$ which form a large angle with the interface will spend only a short time in the skin region (λ) where the magnetic field is confined to and therefore will interact only slightly with this field. On the other hand, Cooper pairs with momentum $\mathbf{p}_2$ oriented within a small angle $\theta \lesssim d\theta \sim \lambda/\xi_0$ to the interface will spend a longer time in the field and hence participate effectively in the Meissner effect. Thus, one may conclude that

$$n_{eff} \sim n d\theta \sim n\frac{\lambda_P}{\xi_0}. \tag{2.74}$$

The combination of Eqns. 2.73 and 2.74 gives an estimate of the Pippard penetration depth

$$\lambda_P \sim \lambda_0 \times n_{eff} \sim \lambda_0 \left(\frac{\xi_0}{\lambda_0}\right)^{1/3}, \tag{2.75}$$

which shows that λ_P is larger than the corresponding London (local limit) penetration depth λ_0, showing that the Meissner effect is less effective in the nonlocal limit compared with the local limit.

Finally, note that at sufficiently high temperatures the penetration depth will eventually become bigger than the BCS coherence length and therefore close to T_c all superconductors behave like London (local) superconductors.

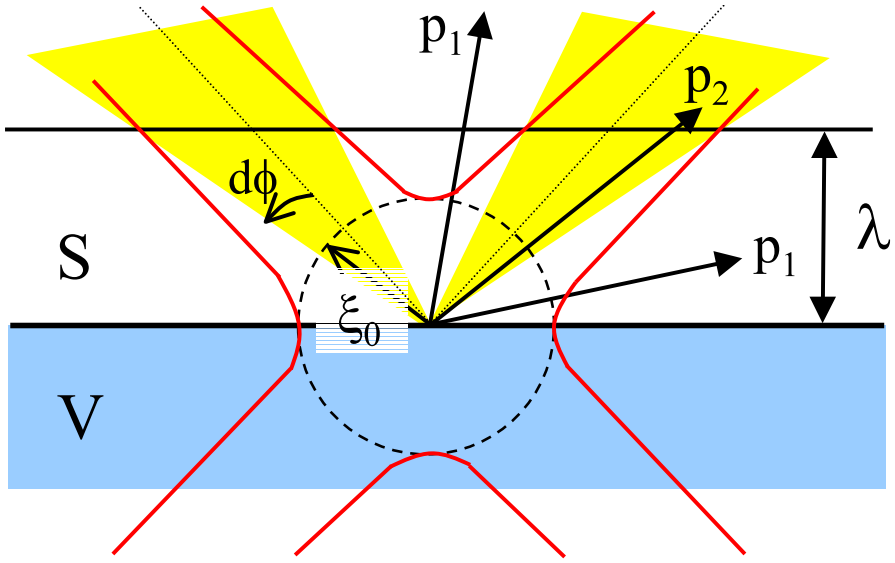

Figure 2.3: Superconductor(S)-Vacuum(V) interface of a $d_{x^2-y^2}$ superconductor, in the Pippard limit. The dotted lines denote the angular position of the nodes ($\phi = \pi/4, 3\pi/4$). The shaded region inside the superconductor shows the gap opens up linearly close to the nodes. The distance between the origin and a point on the hyperbolas is the anisotropic coherence length $\xi(\phi)$. Note that near the nodes $\xi(\phi)$ diverges. This figure is a modification from Ref. [8].

The situation is similar in d-wave superconductors, where there are nodes in the superconducting gap. The basic idea is to replace the QDOS $N(E)$ in the local result Eqn. 2.59 by an effective one, $N_{eff}(E)$, which takes into account that not all the quasiparticles participate with the same weight in the expression of $\Delta\lambda(T)$. The simple picture is this: Once the temperature is increased above $T = 0$, thermally excited quasiparticles are created in the system as a result of the thermal breakup of Cooper pairs. Since the gap is anisotropic, the breakup of Cooper pairs is preferential in momentum space and at the lowest temperatures the pairs affected are only those which correspond to electronic momenta oriented within a small angle ϕ about the nodes of the gap function. The effective coherence length (anisotropic "spatial extent") of these Cooper pairs, represented schematically in Fig. 2.3, is

$$\xi(\phi) = \xi_0 \frac{\Delta_0}{\Delta(\phi)} \sim \frac{\xi_0}{\phi}. \tag{2.76}$$

Here we have assumed that close to the nodes the gap function varies as $\Delta(\phi) \sim \phi$ (ϕ is the angle measured from one of the nodes of the gap function). For a $d_{x^2-y^2}$ gap function one has $\Delta(\phi) \approx 2\Delta_0\phi$. If the excitation energy $E \lesssim T^*$ (here $k_B = 1$), i.e.

$$E \sim \Delta(\phi) \lesssim \Delta(\phi^*) \sim T^* \equiv \alpha_0\Delta_0, \tag{2.77}$$

where $\alpha_0 = \xi_0/\lambda_0$, then the corresponding coherence length $\xi(\phi) \gtrsim \lambda_0$, i.e.

$$\xi(\phi) \sim \xi_0\frac{\Delta_0}{E} \gtrsim \xi_0\frac{\Delta_0}{\alpha_0\Delta_0} = \xi_0\frac{\lambda_0}{\xi_0} = \lambda_0, \tag{2.78}$$

i.e. $E \lesssim T^* \Rightarrow \xi(\phi) \gtrsim \lambda_0$. If E is the thermal energy available at temperature T, then for $T < T^*$, one needs to employ nonlocal electrodynamics to account for the nodal regions on the FS. Similar to the reasoning for s-wave superconductors, the effective superfluid density n_{eff} will be reduced by a factor $\lambda_P/\xi(\phi) \sim \lambda_P\Delta(\phi) \sim T$, using Eqns. 2.74, 2.76 and 2.77. *This therefore introduces an additional factor T to the temperature dependence of penetration depth in the London limit.* Hence the removal of quasiparticles from the condensate leads to a *lesser* increase of $\Delta(T)$ in the penetration depth than one would expect based on local electrodynamics. We introduce an effective DOS $N_{eff}(E)$ which takes into account that for $E \lesssim T^*$ only a fraction $E/T^* \lesssim 1$ of $N(E)$ contributes to the temperature dependent part of the penetration depth, i.e.

$$N_{eff}(E) \sim N(E)\ \min(1, \frac{E}{T^*}). \tag{2.79}$$

According to Eqn. 2.59, $\Delta\lambda(T) \sim N(T)$, therefore

$$\Delta\lambda(T) \sim N_{eff}(T) \sim T\ \min(1, \frac{T}{T^*}). \tag{2.80}$$

In conclusion

$$\Delta\lambda(T) \sim \begin{cases} T & \text{for} \quad T \gg T^* \quad \text{(London limit)} \\ \frac{T^2}{T^*} & \text{for} \quad T \ll T^* \quad \text{(Pippard limit)} \end{cases} . \tag{2.81}$$

In Chapter 4, when we discuss the results on $CeCoIn_5$, we will calculate the experimental crossover temperature from linear to quadratic, T^*_{expt}, from the superfluid graph. Then we compare this value to T^*_{imp} and T^*_{NL}, and see that nonlocality explains the crossover better than resonant impurity scattering.

There is another, more direct, way of distinguishing the crossover caused by impurity scattering and nonlocality. For a *d*-wave superconductor *with line nodes along the c-axis*, nonlocality is expected to be relevant only when the applied magnetic field is oriented parallel to the *c*-axis, while the effect of impurities should not depend on the orientation of the field. As KL noted, if T^*_{expt} in $\Delta\lambda_\parallel(T)$ is noticeably smaller in the $H \perp c$ than in the $H \parallel c$ configuration, then we may conclude that the observed effect is due mainly to nonlocal electrodynamics and not to impurities. This dependence on field orientation appears as a factor $\hat{\mathbf{q}} \cdot \mathbf{p}$ in the electromagnetic kernel, where $\hat{\mathbf{q}}$ is the direction of penetration of the magnetic field, and $\mathbf{p}$ is the electron momentum. Nonlocality manifests itself only when $\hat{\mathbf{q}} \cdot \mathbf{p} \neq 0$. In the $H \parallel c$ orientation, both $\hat{\mathbf{q}}$ and $\mathbf{p}$ lie along the basal *ab*-plane, and so nonlocal effects should be noticeable. If $H \perp c$, things are a bit more complicated, as now the measured $\lambda(H \perp c)$ is an admixture of $\lambda_\parallel^{H\perp c}$ and $\lambda_\perp$. One therefore has to subtract the $\lambda_\perp$-component to extract out $\lambda_\parallel^{H\perp c}$. The direction of penetration $\hat{\mathbf{q}}$ due to $\lambda_\parallel^{H\perp c}$ is now perpendicular to $\mathbf{p}$, hence $\mathbf{q} \cdot \mathbf{p} = 0$, and so the crossover due to nonlocality should not be observable, which translates into a smaller T^*. Unfortunately, in our measurement on $CeCoIn_5$ we were unable to extract $\lambda_\perp$ from $\lambda(H \perp c)$. Hence we cannot determine the temperature dependence of $\lambda_\parallel^{H\perp c}$. This will be explained in greater detail in Chapter 4.

Chapter 3

Experimental Method

3.1 Tunnel Diode LC Oscillator Circuit

This system was developed by Dr.Ismardo Bonalde and Dr. Brian Yanoff. The setup was first designed by Van Degrift [22], and described in great detail in Dr. Brian's Yanoff's Ph.D thesis [23]. Figs. 3.1 and 3.2, taken from Ref. [23], show the schematic of the cold end of the apparatus. We used an Oxford 25 Dilution Refrigerator to provide cooling of our sample down to $\sim$ 80 mK. Fig. 3.3 shows the various components of the room-temperature circuit. The dc bias for the tunnel diode is generated at room temperature by a semiconductor reference voltage source (Burr-Brown model REF10), which provides a very stable 10 V output. This voltage is buffered with a low-noise op-amp and filtered before passing out to the cryostat through a semi-rigid coaxial cable. Maintaining a constant voltage across the stable 5 kΩ resistor makes the voltage source act as a precision current source. The same semi-rigid coaxial cable is used to carry the very small rf output signal back up to the room-temperature electronics. The oscillator output signal goes into a mixer (Hewlett-Packard model 10514A) outside the refrigerator. The mixer output (in the kHz range) is the difference between the (fixed) frequency f_{syn} of a synthesizer (Stanford Research Systems model DS345), and the frequency of the oscillator circuit, which varies with temperature. The mixer output is then amplified and filtered, before being read by a universal frequency counter (Hewlett-Packard model 53131A). The frequency counter is equipped with an optional high stability time base,

which provides a stability of 1 ppb. This 10 MHz time base signal is also used to generate the synthesized local oscillator signal.

The amplification and filter of the mixer output was carried out by the input stage of a lockin amplifier (Stanford Research Systems model SR530). The usual lockin output is not used, instead an output on the back of the instrument provides access to the preamplified, filtered signal (called "signal monitor"), and is connected to the frequency counter. The filter is a bandpass filter centered at the lockin reference frequency f_{LI}, with a bandwidth of $f_{LI}/5$. f_{LI} is set by another Stanford Research DS345 synthesizer (also synchronized with the frequency counter time base) connected to the lockin reference frequency input. The signal frequency should stay within the pass band as it shifts due to the temperature dependence of the sample. f_{LI} is usually set to be 20 kHz, so the bandwidth is 4 kHz. If the frequency shift over the temperature range of interest is greater than 4 kHz, then f_{syn} and f_{LI} can be easily adjusted to a larger value. We usually set f_{LI} to be 40 kHz for measurements close to T_c.

The sample, which is thermally connected to the mixing chamber, is placed inside the primary coil (Fig. 3.2). The tapping coil, together with the tunnel diode and other parts of the low-temperature electronics, is housed inside a copper casing. Fig. 3.4 shows the components of the low-temperature electronics. Resistor R_1 serves as an rf isolation, as well as letting the direct current pass from the room-temperature current supply to the tunnel diode. R_2 forms a voltage divider with R_1 to provide the proper dc bias for the tunnel diode. The bypass capacitor C_B is so large ($\sim$nF) that it almost appears as a short circuit at the operating frequency of $\sim$21 MHz. Resistor R_p prevents the (parasitic) oscillation of the tuned circuit unintentionally formed by the tapping coil and the stray capacitance of the tunnel diode; it should not be so large as to disturb the fundamental oscillation. The coupling capacitor C_c allows only a small portion of the rf signal to pass up the coax to the room-temperature electronics. If C_c is too large, the external electronics will distort the oscillation waveform, so C_c has to be small enough that only a small fraction of the rf signal is

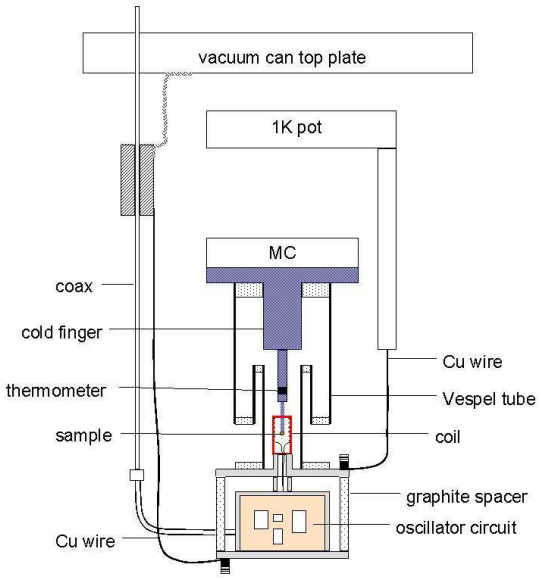

Figure 3.1: Schematic of the cold end of the apparatus. MC is the mixing chamber of the dilution refrigerator. The 1K pot and vacuum can top plate are also shown. For clarity, the vacuum can itself is not shown. Taken from Ref. [23].

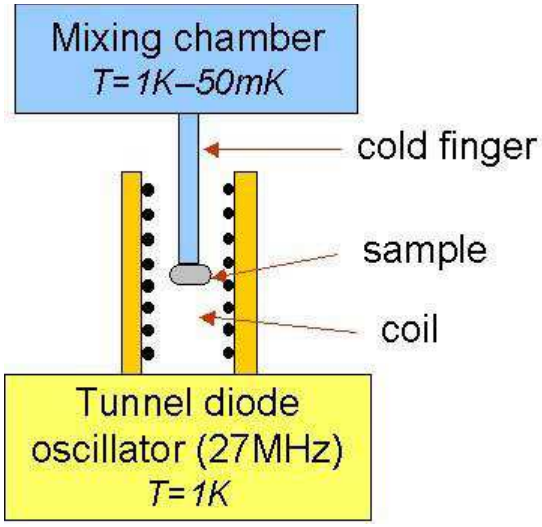

Figure 3.2: The primary coil with coldfinger and sample inserted. Taken from Ref. [23].

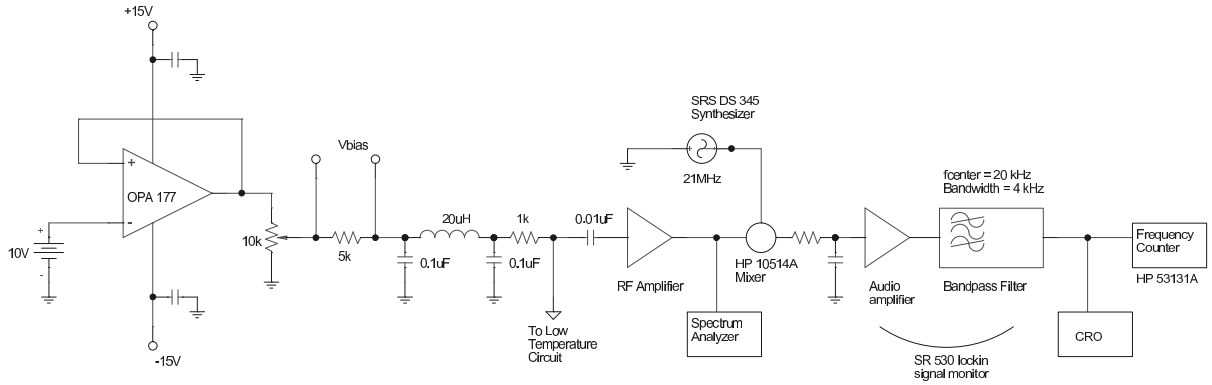

Figure 3.3: Room temperature electronics

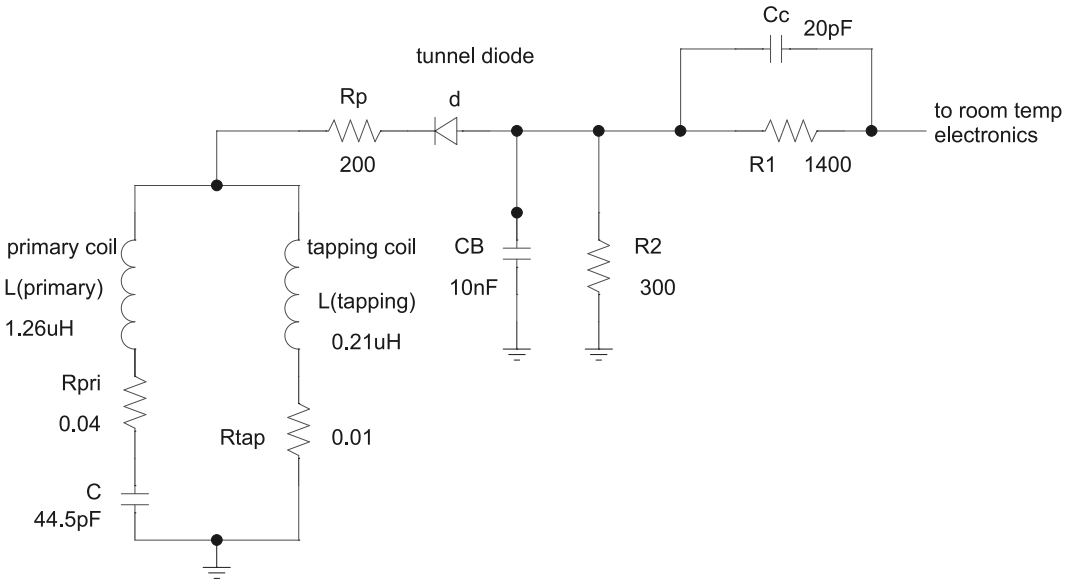

Figure 3.4: Low-temperature electronics

coupled out. Therefore the tunnel-diode oscillator circuit is almost completely isolated from the room-temperature electronics. For our oscillator, the operating values are $R_1 = 1400\ \Omega$, $R_2 = 300\ \Omega$, $C_c = 20$pF, $C_B = 10$nF, and $R_p = 200\ \Omega$.

The current-voltage behavior of a tunnel diode can be explained by a combination of quantum mechanical tunnelling and the usual forward-biased characteristic of a semiconductor diode (see for example, Ref. [24]). Fig. 3.5 shows the I-V characteristic of the tunnel diode used in our system, at room temperature, 77 K and 4 K. Notice the region of V where the *differential (or ac) resistance*, dV/dI, is negative. This is the region where the tunnel

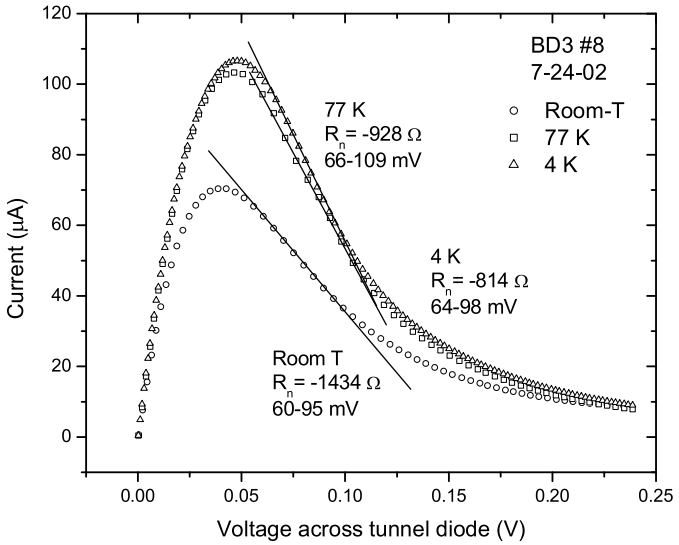

Figure 3.5: I-V curves of tunnel diode BD3 #8, at room temperature (◯), 77 K (□) and 4 K (△). The values of R_n $(= (dI/dV)^{-1})$ are calculated from the inverse slopes of the solid lines shown.

diode must operate to cancel the dissipative losses in the tuned circuit, so as to sustain the oscillation. The dc bias supply serves to bias the tunnel diode into the negative-dV/dI region. The process to locate the oscillation (resonant) frequency is as follows: (1) cool the system down to 4 K, (2) set the center frequency of the bandpass filter to say 20 kHz, (3) vary the bias voltage via the helipot until the spectrum analyzer reveals a very sharp and strong peak, (4) note the location (f_s) of the peak, (5) set the synthesizer frequency such that it is 20 kHz above f_s. The CRO should show a sinusoidal oscillation pattern with a frequency of 20 kHz.

We can estimate the value of the bias current, and hence bias voltage, required to bias the tunnel diode into the negative ac-resistance region. Fig. 3.6 shows the dc equivalent of the low-temperature circuit, which is in effect a potential divider. We have ignored the small dc resistance of the tapping coil ($\sim 1\ \Omega$). From Fig. 3.5 we know the upper and lower limits of the required bias voltage across the tunnel diode. From them we can calculate, from Fig. 3.5, the dc resistances $(= V/I)$ of the tunnel diode (R_{TD}). It is then trivial to calculate

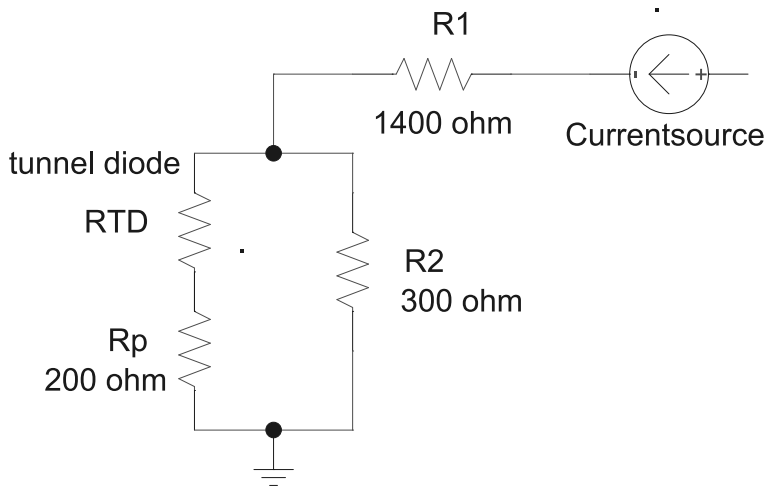

Figure 3.6: DC equivalent of low-temperature electronics. The resistance of the tapping coil ($\sim 1\ \Omega$) has been ignored. RTD is the dc resistance of the tunnel diode.

the value of the voltage that needs to be provided by the bias voltage source. Our calculated values using this method agree well with the experimental values obtained in the preceding paragraph. Finally, we usually disconnect the spectrum analyzer and the CRO when taking data.

Thermometers are placed near the sample, at the top and bottom, of the oscillator circuit to monitor the temperatures of the sample, the primary coil and the oscillator electronics respectively. The coil and electronics sensors are calibrated Cernox and Silicon diode sensor, respectively, from Lakeshore. The sample temperature is monitored using a RuO_2 resistor at low temperatures (0.08–1.8 K), and a calibrated Cernox thermometer at higher temperatures (1.3–20 K). The RuO_2 sensor was calibrated against a calibrated Germanium sensor from Lakeshore. Heaters are also placed in the vicinity of these three thermometers to change or maintain the temperatures. G10-spacers are used to maintain a temperature difference between the primary coil and the electronics. Temperature stability of the primary coil and the oscillator electronics is of utmost importance in our experiments, as they determine the noise level of our signal, especially at low temperatures, where our signal is very small. Usually we can achieve a temperature stability of ± 1 mK in both thermometers. We also found that for the same temperature change away from the set-point of the thermometer,

say +1 mK, the frequency jump caused by the electronics is about 50 times that caused by the primary coil. Hence it is far more important to keep the electronics temperature stable, than for the primary coil.

The tunnel diode oscillator has a noise level of 2 parts in 10^9 and low drift. Using a method from Ref. [25], the magnitude of the ac field is estimated to be between 30 and 50 mOe, depending on the value of the bias voltage. The cryostat was surrounded by a bilayer Mumetal shield that reduced the dc field to less than 1 mOe. The sample can be aligned inside the probing coil in all three crystallographic directions. The sample was mounted, using a small amount of GE varnish, on a single crystal sapphire rod. The other end of the rod was thermally connected to the mixing chamber of an Oxford Kelvinox 25 dilution refrigerator.

We seek to measure $\Delta\lambda(T)$ by measuring $\Delta f(T) \equiv \delta f(T) - \delta f(T_{min})$, where $\delta f(T) = f_{syn} - f_s(T)$, f_{syn} = (fixed) frequency of a Stanford Research DS345 synthesizer, f_s = resonant frequency of the tuned oscillator circuit. The superconductor sample is placed inside an primary coil — the inductor-part of a parallel-LC resonator circuit. As the temperature of the sample changes below T_c, magnetic field is expelled from the sample in various amounts, changing the inductance of the primary coil. This changes the resonant frequency of the oscillator circuit f_s, and hence Δf changes.

3.2 Inductance of the Primary Coil

The construction of the primary coil was described in detail in Ref. [23]. I constructed a 32-turn coil made of 44 AWG wires (wire diameter = 0.00508 cm), with the turns spaced two-wire-diameters apart. From Ref. [26], the inductance of a single-layered, tightly wound, long, thin solenoidal coil is

$$L = \frac{4\pi^2 r^2 N^2}{l} \times 10^{-9} \quad \text{henries}, \tag{3.1}$$

where N is the number of turns, l (in cm) is the length of the coil, and r (in cm) is the radius of cross-section of the wires.

As the solenoid is made shorter, the field inside is no longer uniform, and the inductance becomes a function of the ratio of length to radius. Eqn. 3.1 must then be multiplied by a correction factor K_1, whose value is

$$K_1 = \frac{1}{1 + 0.9(\frac{r}{l}) - 0.02(\frac{r}{l})^2}. \tag{3.2}$$

Next, if the turns are spaced well apart, another correction must be made for the fact that the current is concentrated in the wires and not uniformly distributed over the coil. This introduces another correction factor K_2

$$K_2 = \left[1 - \frac{l(A+B)}{\pi r N K_1}\right], \tag{3.3}$$

$$\text{where} \quad A = 2.3 \log_{10} 1.73 \frac{d}{c} \tag{3.4}$$

$$\text{and} \quad B = 0.336 \left(1 - \frac{2.5}{N} + \frac{3.8}{N^2}\right). \tag{3.5}$$

d is the diameter (in cm) of the circular wire, and c is the winding "pitch", i.e. the center-to-center distance between successive turns. Then the final inductance of the coil L is

$$L = L_0 \times K_1 \times K_2. \tag{3.6}$$

For my primary coil $r \approx 0.127$ cm, $N = 32$, $l \approx 0.4$ cm, $d = 0.00508$ cm, and $c = 2d = 0.01016$ cm. Hence $L_0 = 1.63$ μH, $K_1 = 0.78$, $K_2 = 0.99$, giving $L_p = 1.26$ μH. A similar calculation for the tap coil gives $L_T = 0.21$ μH. Hence the total inductance of the oscillator circuit is $L = L_p + L_T = 1.47$ μH. When we tested the circuit at 4 K, we obtained a (empty coil) resonant frequency f_0 of 29.6248 MHz, giving $L = 1.43$ μH (using $C = 20.2$ pF). This agrees very well with the calculated value of 1.47 μH. When we changed the capacitance C to

≈ 44.5 pF (nominal value 47 pF), however, we get $f_0 = 20.7609$ MHz and thus $L = 1.32$ μH, which differs more from the calculated value, but still comparable to it. We stuck to using the 47 pF-capacitor in our final configuration.

3.3 Relation between Inductance and Susceptibility

The subsection follows closely that of Ref. [27]. If the inductance of the primary coil is L_0 when the coil is empty, i.e. when no sample is inside, then we want to know its inductance when containing the sample, L_s. In general the self inductance of a coil is related to the total stored energy in it by

$$u = \frac{1}{2} L_s I^2 \tag{3.7}$$

when a current I flows in it. This energy is also equal to the total field energy (in Gaussian units)

$$U = \frac{1}{8\pi} \int \mathbf{B} \cdot \mathbf{H} d^3 r. \tag{3.8}$$

Since we are only interested in the *change* in inductance, we need to find

$$\Delta U = \frac{1}{8\pi} \int (\mathbf{B} \cdot \mathbf{H} - \mathbf{B}_0 \cdot \mathbf{H}_0) d^3 r, \tag{3.9}$$

where $\mathbf{H}_0$ and $\mathbf{B}_0$ are the initial fields without any sample. Eqn. 3.9 can be written in terms of an integral only over the sample [28]

$$\Delta U = \frac{1}{2} \int_{V_s} \mathbf{M} \cdot \mathbf{B}_0 d^3 r, \tag{3.10}$$

where $\mathbf{M}$ is the magnetization in the sample. But

$$\Delta U = \frac{1}{2} \Delta L I^2. \tag{3.11}$$

Therefore the change in inductance is given by

$$(L_s - L_0)I^2 = \int_{V_s} \mathbf{M} \cdot \mathbf{B}_0 d^3r. \tag{3.12}$$

If the sample is an ellipsoid of revolution and is small enough to be in the uniform part of the coil field, then the magnetization inside the sample is uniform and equal to

$$M = \frac{\chi}{1 + N\chi} B_0, \tag{3.13}$$

where N is the demagnetization factor, and χ is the volume susceptibility. Hence we get

$$\frac{L_s - L_0}{L_0} = \frac{4\pi\chi}{1 + N\chi} \frac{V_s}{V_c}, \tag{3.14}$$

where V_s is the sample volume, V_c is the coil volume, and we have taken $\frac{1}{2}L_0 I^2 = B_0^2 V_c / 8\pi$ (i.e. the coil is assumed long compared to its diameter). If the field inside the coil is not uniform then the ratio V_s/V_c should be replaced by the *geometrical filling factor* F, where

$$F = \frac{\int_{V_s} B_0^2(\mathbf{r}) d^3r}{\int_{V_c} B_0^2(\mathbf{r}) d^3r}, \tag{3.15}$$

which in the limit of a very long coil compared to the diameter, gives V_s/V_c. The numerator and denominator of the right-hand-side (RHS) of Eqn. 3.15 are sometimes called the *magnetic* volume of the sample and coil, respectively. Eqn. 3.14 then becomes

$$\frac{L_s - L_0}{L_0} = \frac{4\pi\chi}{1 + N\chi} F. \tag{3.16}$$

I wish to clarify the sometimes confusing notation of Eqn. 3.16 in the literature. It is written in CGS units, but the product $N\chi$ in the denominator can be in either CGS or SI units, i.e. $N_{cgs}\chi_{cgs} = N_{SI}\chi_{SI}$, where $N_{cgs} = 4\pi N_{SI}$ and $\chi_{SI} = 4\pi\chi_{cgs}$. This is important because in the superconducting state at $T = 0$, $\chi_{cgs} = -1/4\pi$ or $\chi_{SI} = -1$. In Ref. [29], the

authors obtained the factor $1/(1-N)$ in their expression for χ, though the expression was written in CGS units. Their empirical expression for N is also in SI units. This must mean that the authors used $\chi_{SI} = -1$ implying that the factor is really $1/(1-N_{SI})$. In all our subsequent discussion the demagnetization factor N is really N_{SI}, i.e. $0 < N_{SI} < 1$. I shall rewrite Eqn. 3.16 as

$$\frac{L_s - L_0}{L_0} = \frac{4\pi\chi_{cgs}}{1 + N_{SI}\chi_{SI}}F. \tag{3.17}$$

Below the superconducting transition temperature T_c, $\chi_{SI} \approx -1$ — the value for perfect Meissner screening. We substitute this value into the denominator of the RHS of Eqn. 3.17 to get

$$\frac{L_s - L_0}{L_0} = \frac{4\pi\chi_{cgs}}{1 - N_{SI}}F. \tag{3.18}$$

Note that we have used the perfect Meissner value, or equivalently, the $T = 0$ value, of χ in the denominator, while leaving χ in the numerator intact. We use this approximation because we want a *linear* relationship between inductance and susceptibility, one that forms the basis of our calibration method described later.

We see therefore that what we are really measuring is the susceptibility of the sample, which translates to inductance via Eqn. 3.18. Since the resonant frequency of our LC-oscillator circuit is $f_s = \frac{1}{2\pi\sqrt{LC}}$, where $L = L(\text{primary coil}) + L(\text{tapping coil})$, a change in the inductance of the primary coil thus results in a change of f_s. If the resonant frequency of the oscillator when the primary coil is empty is

$$f_0 = \frac{1}{2\pi\sqrt{L_0 C}}, \tag{3.19}$$

then when the sample is inserted, the resonant frequency will *decrease* to

$$f_s = \frac{1}{2\pi\sqrt{L_s C_s}}, \tag{3.20}$$

where L_0 and L_s are defined above, and $(C_s - C)$ is the change in stray capacitance when inserting the sample. If one assumes $(L_s - L_0)/L_0 \ll 1$ and $(C_s - C)/C \ll 1$, then we obtain

$$\frac{f_0 - f_s}{f_0} = \frac{1}{2}\frac{L_s - L_0}{L_0}. \tag{3.21}$$

Hence Eqn. 3.18 becomes

$$\frac{f_0 - f_s}{f_0} = \frac{4\pi\chi_{cgs}}{2(1 - N_{SI})}F. \tag{3.22}$$

In our experimental setup, our samples have the typical dimensions of $1\times1\times0.1-0.4$ mm^3, with the last dimension (thickness) parallel to the axis of the coil. Compare this with the coil — it has a length of 4 mm and radius 1.27 mm. Our calculations show that the empty-coil magnetic field $B_0(\mathbf{r})$ within 0.4 mm away from the coil center has a non-uniformity of only up to 1.3%. Thus we conclude that the empty-coil-field $B_0(\mathbf{r})$ is almost constant inside the sample, and the ratio V_s/V_c can be used to represent the filling factor F. Also, we measure the resonant frequency $f_s(T)$ of the oscillator circuit at a temperature T *relative to* $f_s(T_{min})$ *at the base temperature* T_{min}, i.e. we measure $\delta f(T) = f_s(T) - f_s(T_{min})$. So Eqn. 3.22 becomes

$$\frac{\delta f(T)}{f_0} \equiv \frac{f_s(T) - f_s(T_{min})}{f_0} = -\frac{4\pi\Delta\chi(T)}{2(1 - N_{SI})}\frac{V_s}{V_c}, \tag{3.23}$$

where $\Delta\chi(T) = \chi(T) - \chi(T_{min})$.

The next question is: how is $\delta f(T)$ related to $\Delta\lambda(T)$, the change in penetration depth of the sample? The answer: $\Delta\lambda$ appears in the expression for χ.

3.4 Relation between Susceptibility and Penetration Depth

In Section 2.3 we considered an infinite slab of thickness $2d$ placed in a uniform applied magnetic field H_0 parallel to its surface, subject to the boundary conditions $B(\pm d) = H_0$.

The solution of Eqn. 2.37 is [13]

$$B(z) = H_0 \frac{\cosh(z/\lambda)}{\cosh(d/\lambda)}. \tag{3.24}$$

Let us now derive the susceptibility χ from Eqn. 3.24. The magnetization M (magnetic moment per unit volume) of the slab can be obtained from [30]

$$4\pi M = \frac{1}{2d} \int_{-d}^{d} (B - H_0) dz, \tag{3.25}$$

which gives

$$M = -\frac{H_0}{4\pi} \left(1 - \frac{\lambda}{d} \tanh \frac{d}{\lambda} \right). \tag{3.26}$$

The susceptibility $\chi = M/H_0$ is thus

$$-4\pi\chi = 1 - \frac{\lambda}{d} \tanh \frac{d}{\lambda}. \tag{3.27}$$

For our single crystals $\lambda \ll d$, thus $\tanh(d/\lambda) = 1$, and hence

$$-4\pi\chi = 1 - \frac{\lambda}{d} \quad (\lambda \ll d). \tag{3.28}$$

Our measurements were almost always taken when the applied magnetic field is oriented *perpendicular* to the sample surface. This introduces an additional factor $1/(1-N)$ (from now on $N \equiv N_{SI}$), but is absorbed into the definition of $\chi = \frac{M}{H_0/(1-N)}$ in Eqn. 3.27, so it doesn't explicitly appear there. Moreover, Eqn. 3.27 applies only to an infinite slab. For a $2w \times 2w$ slab, thickness $2d$ and field perpendicular to the plane, field penetration is in the $2w$-directions. The quantity d in Eqn. 3.27 must be replaced by R_{3D}, the *effective* dimension of the sample. The motivation for R_{3D} will be explained in the next section. Here we will just mention that R_{3D} is of the same order of magnitude as w. With these two corrections,

Eqn. 3.27 becomes

$$-4\pi\chi = 1 - \frac{\lambda}{R_{3D}} \tanh\left(\frac{R_{3D}}{\lambda}\right) \tag{3.29}$$

which, in the $\lambda \ll R_{3D}$ limit, gives

$$-4\pi\chi = 1 - \frac{\lambda}{R_{3D}} \quad (\lambda \ll R_{3D}), \tag{3.30}$$

or

$$4\pi\Delta\chi = \frac{\Delta\lambda}{R_{3D}} \quad (\lambda \ll R_{3D}). \tag{3.31}$$

Combining Eqn. 3.23 and Eqn. 3.31, we finally get

$$\frac{\delta f(T)}{f_0} = -\frac{V_s}{2V_c(1-N)} \frac{\Delta\lambda(T)}{R_{3D}} \quad (\lambda \ll R_{3D}), \tag{3.32}$$

where $\Delta\lambda(T) = \lambda(T) - \lambda(T_{min})$. Eqn. 3.32 hence relates δf to the actual change in penetration depth $\Delta\lambda$.

From Eqn. 3.32 we can write

$$\Delta\lambda(T) = G\delta f(T), \tag{3.33}$$

where

$$G = -\frac{2R_{3D}(1-N)}{V_s} \frac{V_c}{f_0}. \tag{3.34}$$

The negative sign in G comes from the fact that as temperature increases, field penetration increases ($\Delta\lambda > 0$). But as field penetration increases, the stored energy inside the coil increases, hence the inductance increases, and the corresponding resonant frequency f_s *decreases*, i.e. $\delta f < 0$. We want to work with a positive G, so we subtract the signal from that of a synthesizer (with frequency f_{syn}) using a mixer, as described in Section 3.1, and adjust f_{syn} so that $f_{IF} = f_{syn} - f_s$ is positive and roughtly in the 20–40 kHz range (IF denotes

"intermediate frequency"). Therefore $\Delta f \equiv f_{IF}(T) - f_{IF}(T_{min}) > 0$ when $T > T_{min}$, with the calibration factor G now being positive, with the same magnitude as in Eqn. 3.34.

3.5 Calibration

As described in the preceding paragraph, the deviation $\Delta\lambda(T) = \lambda(T) - \lambda(T_{min})$ is proportional to the change in resonant frequency $\Delta f(T)$, with the proportionality factor G dependent on sample and coil geometries. In Ref. [23] a method of obtaining G for an arbitrary sample was (1) to cut out a piece of high-purity Al platelet to have the same dimensions as the sample, (2) take Δf measurements of this Al platelet, (3) adjust G such that the superfluid data fits the nonlocal BCS expression (Eqn. 3.39), and finally (4) use this value of G for the sample. Though this method works, it is a very tedious process to cut out a Al platelet of exactly the same dimensions every time we run a new sample. We tried two other methods to determine G.

For a square sample of side $2w$, thickness $2d$, demagnetization factor N, and volume V, G is, from Eqn. 3.34

$$G = +\frac{2R_{3D}(1-N)}{V_s}\frac{V_c}{f_0}, \tag{3.35}$$

where

$$R_{3D} = \frac{w}{2f(2d/w)} \tag{3.36}$$

is the effective sample dimension [29], and the correction factor $f(2d/w)$ is

$$f\left(\frac{2d}{w}\right) = \left[1 + \left(1 + \frac{2d}{w}\right)^2\right] \arctan\left(\frac{w}{2d}\right) - \frac{2d}{w}. \tag{3.37}$$

In Eqn. 3.35 the quantities R_{3D}, N and V_s can be determined with reasonable accuracy. The empty-coil resonant frequency f_0 differs from run to run ($\sim 10^3$ Hz), but the fractional error is negligible ($\Delta f_0/f_0 \sim 10^3/10^7 \sim 0.1\%$). What remains to be determined is V_c, the coil volume. We tried to determine V_c by measuring $\Delta f(T)$ of an Al sphere of known

dimensions (1/32"-diameter) and adjusted G such that the superfluid data fits the nonlocal BCS expression (Eqn. 3.39). This enables us, from Eqn. 3.35, to calculate V_c. However, this value of V_c gives us a value of G about 4 times too small for conventional BCS samples (such as Pb) to fit the empirical BCS expression for superfluid density. We attribute the error to the low T_c of the Al sphere ($\sim$ 0.8 K), compared to 1.2 K in the purest sample. With this low T_c we can no longer assume that the zero-temperature penetration depth $\lambda(0)$ of this Al sphere is $\sim$ 500 Å, the commonly accepted value, due to the decrease of the mean free path with impurities. Energy dispersive X-ray (EDX) analysis on the surface of the sphere revealed the presence of Mn impurities, explaining the low T_c. The use of a wrong value of $\lambda(0)$ directly affects the value of the calculated superfluid density.

Alternatively, to eliminate the error of determining V_c, we instead make use of the proportionality relation from Eqn. 3.35

$$G \propto \frac{R_{3D}(1-N)}{V_s}, \tag{3.38}$$

which eliminates the need to determine V_c and f_0 altogether. The motivation for R_{3D} is as follows: Most single-crystal superconductors have rectangular basal planes, with aspect ratios typically ranging from 1 to 30. A consequence of the high aspect ratio is that for fields applied perpendicular to the basal plane, in addition to screening currents flowing along the sides of the sample, there is also a contribution from the currents flowing on the *top* and *bottom* surfaces. These currents are due to the shielding of the in-plane component of the applied magnetic field that appears due to demagnetization. The correction factor *f(2d/w)* accounts for this additional contribution. For example, in the infinitely-thin limit, $\mathrm{R}_{3D} \approx 0.16w$. Compare this with $0.5w$ if the top and bottom screening current contributions are ignored — the "infinite-slab" value. This method has been shown to work for Nb cylinders and foils, as well as single crystals of YBCO and BSCCO [29]. When we used the infinite-slab value on single-crystal Pb, our calculated values of G are smaller than what is required

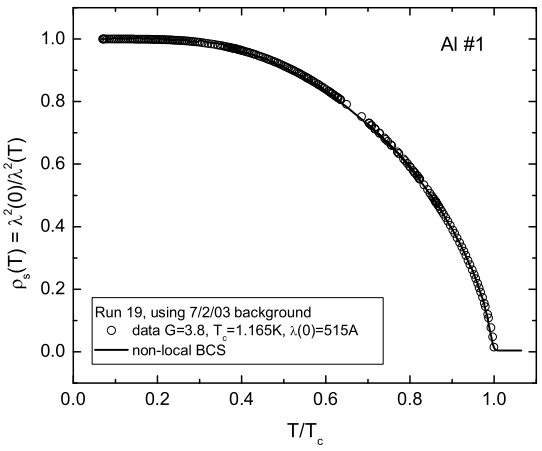

Figure 3.7: Superfluid density of Al single crystal. Circles: data. Line: Fit to non-local limit yields G = 3.8 Å/Hz.

to fit the superfluid data. All but one of our samples are *thin* cylinders or platelets, so this method is applicable to us, and the calculated calibration factors have been shown to be consistent with one another.

We first determine G for a single-crystal sample of high-purity Al (99.9995%) platelet by fitting the Al data to the superfluid density in the pure extreme-nonlocal limit [14]

$$\rho_s(T) = \left[\frac{\Delta(T)}{\Delta(0)} tanh \frac{\beta\Delta(T)}{2}\right]^{-1/3}, \tag{3.39}$$

where the temperature dependence of the superconducting gap, $\Delta(T)$, is given by the interpolation formula [9]

$$\Delta(T) = \delta_{sc} k T_c tanh\left\{\frac{\pi}{\delta_{sc}}\sqrt{a\left(\frac{\Delta C}{C}\right)\left(\frac{T_c}{T}-1\right)}\right\}. \tag{3.40}$$

In Eqn. 3.40 $\delta_{sc} \equiv \Delta(0)/k_B T_c$, $a = 2/3$ for a weak-coupling superconductor, and $\Delta C/C$ is the specific heat jump at T_c. Fig. 3.7 shows the superfluid data for a high-purity (99.999%) single-crystal Al platelet. For the data to fit the extreme nonlocal expression (Eqn. 3.39),

we find G(Al) to be 3.8 Å/Hz. Then, explicitly writing out Eqn. 3.38 (s: sample)

$$\frac{G_s}{G_{Al}} = \frac{R_{3D,s}}{R_{3D,Al}} \frac{1 - N_s}{1 - N_{Al}} \frac{V_{Al}}{V_s}, \tag{3.41}$$

and substituting for sample dimensions, we can obtain the value of G for an arbitrary sample. The demagnetization factor N can be calculated in two ways: For samples with $T_c \geq 2$ K, N can be obtained from the deviation, from $-1/4\pi$, of the (linear negative) slope of magnetization-field measurements ($H < H_{c1}$), using a MPMS SQUID, according to the equation

$$\frac{m}{H} = \frac{V_s}{4\pi} \frac{-1}{1 - N}, \tag{3.42}$$

where m = magnetic moment (in emu), H = applied field (in Oe), and V_s = sample volume (in cm^3). Once again $N = N_{SI}$.

For samples with any T_c, especially if $T_c \leq 2$ K, N can be estimated from the expression [29]

$$\frac{1}{1 - N} \approx 1 + \frac{w}{2d}. \tag{3.43}$$

Eqn. 3.43 works especially well for samples with large aspect ratios [29]. We calculated the value of N using both methods for samples with $T_c \geq 2$ K, and found that they agree very well with each other. Using Eqn. 3.41 on a single crystal of Pb, we found excellent agreement with conventional BCS expressions. Also, we tried this method on the Sr_2RuO_4 sample in Refs. [4] and [23], and obtained $G = 2.4$ Å/Hz. This agrees very well with the value of $G = 2.5$ Å/Hz stated in Ref. [23], once again validating our method of obtaining G.

One possible flaw of this method is that it might *overestimate* the contribution of screening currents from the top and bottom faces of *thicker* samples, so that the calculated value of G is *underestimated* in this configuration. We see a hint of this in Chapter 10, where for the thick Pb#2 sample with aspect ratio $w/d \approx 1.6$, G has to be 20% larger than the calculated value in order for the superfluid data to fit the theoretical expression, whereas

the G obtained for the thinner Pb#1 sample (aspect ratio 6.3) fits the theory extremely well. The samples in Ref. [29] all have very large aspect ratios ($w/d \geq 15$), so this problem does not exist there. However, even in Ref. [29] two of their samples have a deviation of 20% below the expected value, which the authors attributed to the rectangular shape of the samples. This reasoning does not apply to our Pb *cylinders*. Fortunately, among all the samples we have run, only sample Pb#2 has a comparatively small aspect ratio, so this method is applicable in all of our other samples. We should keep in mind, however, that even for our thin platelet samples, because they do not have a perfectly square basal area, the calculated values of G should have an error of about $\pm$ 20% anyway.

3.6 Drift, Noise and Background Signal

There are three sources of error in our frequency data points: (1) Drift, (2) noise, and (3) sample-holder background.

Even at a constant temperature, Δf drifts upwards or downwards, monotonically or non-monotonically, linearly or non-linearly, with rates ranging from $\pm$0.01 Hz/minute to as high as $\pm$1 Hz/minute. The drift usually becomes very small if we wait many hours after topping up the dewar with liquid He, preferably overnight. In order to account for the drift, we include the "drift run" in our data run, monitoring the frequency drift during the first five minutes of any run at base temperature, cancelling the run if the drift is too large or too non-linear, and letting the run proceed if otherwise. We prefer a positive drift, since that is usually its direction. We also found that the magnitude and direction of the drift depends on the value of the bias voltage, so we adjust the bias voltage to ensure that the drift is small and positive. We also prefer to take a quick run ($\sim$ 1 hour), so that the drift is linear during the duration of that run. After the completion of the run, we then subtract the (linear) drift and the background signal (described later) from the raw data to obtain the true signal.

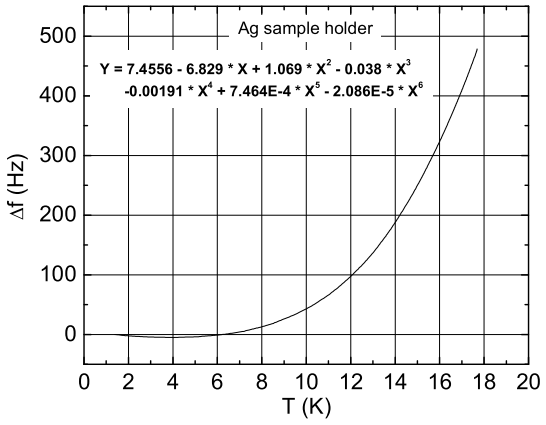

Figure 3.8: Background signal from the silver sample holder: 0.1 K to 18 K. The total signal here is about 500 Hz.

Noise is another source of error. The main source of noise is the vibration of the lines due to the flow of the ^{3}He–^{4}He mixture through the lines, and the vibration of the pumps. Various vibration isolation methods have been used. The pumps are situated outside the screened room, and the pump lines securely bolted to the walls of the screened room. The lines are also wrapped by short lengths of rubber hose at certain points, on both sides of the screened room, to damp out the high-frequency vibrations. Finally, an easy but extremely effective way to reduce the signal noise from ± 0.2 Hz to ± 0.05 Hz is to place the ^{4}He cold trap line *on top* of the dolly that supports the dewar, instead of letting it lie on the ground. In this configuration any vibration (from the floor, flowing mixture, etc) merely causes the cold trap line and the dewar to move *in phase*. There is thus very little relative movement between the line and dewar, causing only negligible noise. If the cold trap line were to lie on the floor, any vibration on the floor (due to footsteps or a host of other possible reasons) would cause the line and the dewar to move *out of phase*, resulting in significant signal noise.

Lastly, even without any sample attached to the end of the sample holder, there is a non-zero signal, i.e. Δf still changes with temperature T. This signal must come from the sample holder itself. We must therefore determine what this "background" signal is, and subtract it from the raw signal to get the true signal.

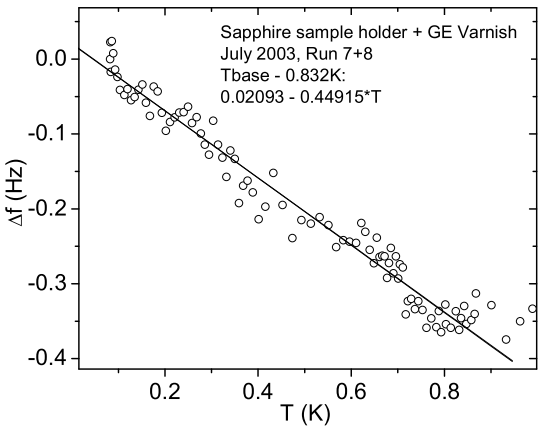

Figure 3.9: Background signal from the sapphire sample holder: Low-temperature blowup

Fig. 3.8 shows the background signal of the silver sample holder constructed by Yanoff *et al.* [23], built from nine silver rods embedded in Stycast 1266 to form a 1-mm-diameter sample rod. It is clear that the silver background signal is very large — the low-T signal is about -5 Hz at 4 K, and the total signal from 0.1 K to 15 K is about 250 Hz. The entire signal is non-monotonic, and its reproducibility at the lowest T, where the real signal can be very small, is only about ± 0.5 Hz. Hence with this silver sample holder, small signals cannot be accurately determined, especially for isotropic s-wave superconductors where the low-T response is exponential, i.e. basically flat.

So I built another coldfinger, with a single-crystal sapphire rod replacing silver as the sample holder. Figs. 3.9 and 3.10 show the background signal from the sapphire holder, at the lowest temperatures and up to $\sim$15 K, respectively. Though the signal is still non-monotonic, the total signal from 0.1 K to 15 K is only about 2 Hz. This is more than 100 times smaller than the silver background signal. In particular, the low-T signal is less than 0.4 Hz, as compared to 5 Hz in the silver-case. This small background enables us to measure very small signals, thus removing any doubt that a small signal might come from the sample holder itself.

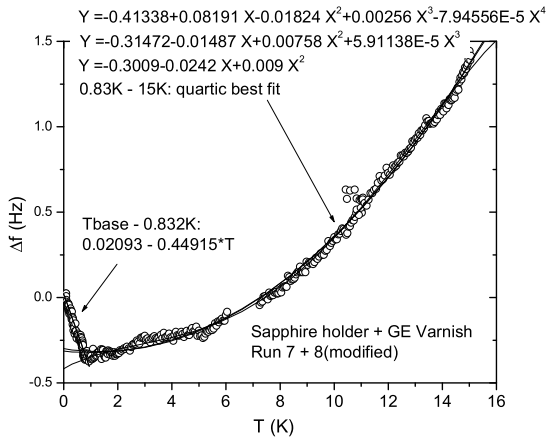

Figure 3.10: Background signal from the sapphire sample holder: 0.1 K to 15 K. Notice that the total signal is less than 2 Hz.

Chapter 4

$CeCoIn_5$

4.1 Introduction

Heavy-fermion superconductors (HFSC) are superconductors whose effective conduction-electron mass m^* is typically more than 100 free-electron masses. The large effective mass has a pronounced effect on several properties of superconducting materials since it enters into the expression for the electron DOS at the Fermi level, $N(0)$ (in SI units)

$$N(0) = \frac{1}{2\pi^2}\left(\frac{2m^*}{\hbar^2}\right)^{3/2} E_F^{1/2}. \tag{4.1}$$

For example, the HFSC $CeCu_2Si_2$ has a value of $N(0)$ that corresponds to $m^* \approx 220m_0$, where m_0 is the free-electron mass [15]. Much of the evidence for the large effective mass comes from the experimental observations in the normal state. For example, from the low-temperature electronic specific heat $C_{el} = \gamma T$, we can obtain the electronic specific heat coefficient γ. From

$$\gamma = \frac{1}{3}\pi^2 N(0) k_B^2, \tag{4.2}$$

we can calculate $N(0)$, and hence m^* from Eqn. 4.1. γ is unusually large for heavy-fermion compounds — typically about 10 times larger than those of other superconductors. Hence a large γ implies a large effective mass.

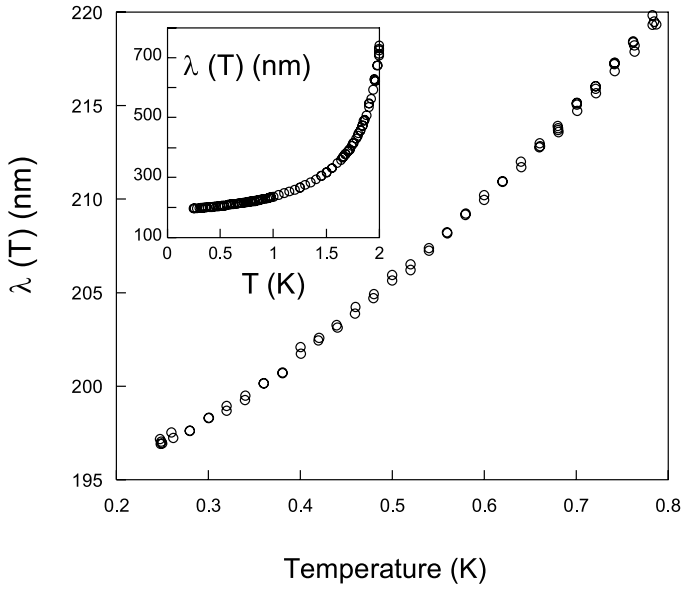

Figure 4.1: The change in penetration depth $\Delta\lambda$ below 0.8 K. Note the obvious upward curvature. Inset: $\Delta\lambda$ over a wider temperature range. Taken from Ref. [34].

The compounds $CeMIn_5$ (M = Co, Ir, Rh) have recently been added to the heavy-fermion family, and have attracted much interest due to their similarity with the cuprates: quasi-2D structure and proximity to magnetic order [31]. $CeCoIn_5$, in particular, is a good candidate for study: its superconductivity is not sensitive to small changes in unit-cell volume or composition, unlike $CeCu_2Si_2$, and it has the highest T_c ($\sim$2.3 K) among the heavy-fermion superconductors. The heavy-fermion nature of $CeCoIn_5$ is evidenced by the large value of the electronic specific heat coefficient $\gamma = 0.29$ J/mol K^2, giving $m^* \approx 83m_0$. $CeCoIn_5$ has tetragonal $HoCoGa_5$ crystal structure, consisting of alternating layers of $CeIn_3$ and '$CoIn_2$' [31]. De Haas-van Alphen (dHvA) data revealed that the Fermi surface (FS) is quasi-2D, with an open 2D undulating cylinder extending along the [001] direction, as well as the large effective masses of electrons on this FS [32]. Nonetheless, the superconducting properties are not very anisotropic [33].

Recently, there has been mounting evidence for unconventional superconductivity in $CeMIn_5$. Specific heat data reveal a T^2 term at low temperature, consistent with the presence of 3D line nodes in the superconducting energy gap [35]. Thermal conductivity measure-

ments with in-plane applied field show four-fold symmetry, consistent with nodes along the ($\pm\pi$, $\pm\pi$) positions [36]. NQR measurements find no Hebel-Slichter peak just below T_c [37]. Below T_c the spin susceptibility is suppressed, indicating singlet pairing [37, 38]. However, there are some ambiguities in some of the measurements. Thermal conductivity data yield a $T^{3.37}$ low-temperature behavior, that the authors claim is close to T^3 behavior predicted for unconventional superconductors with line nodes in the clean limit [35]. NQR measurements did not show the T^3 low-temperature behavior of $1/T_1$ that is expected for a line node gap; instead $1/T_1$ saturates below 0.3 K [37]. Microwave measurements on a dirtier sample ($T_c = 2.17$ K) down to ~0.2 K showed a non-exponential behavior, and the authors claimed that $\lambda(T) \sim T$ below 0.8 K [34], though the data clearly show some curvature in that temperature range (see Fig. 4.1). Further, the field was applied along the *ab*-plane, so the shielding currents have both in-plane and inter-plane components. In this chapter, we present high-precision measurements of in-plane $\lambda_\parallel$ and inter-plane $\lambda_\perp$ penetration depths of $CeCoIn_5$ at temperatures down to 0.14 K. We find that $\lambda_\parallel$ is best treated as a crossover from $\sim T$ to $\sim T^2$ at a temperature T^*. We propose two mechanisms for the crossover — Hirschfeld and Goldenfeld's Resonant Impurity Scattering (RIS) theory [18], and Kostzin and Leggett's [KL] [20] nonlocal theory, with their respective crossover temperatures T^*_{imp} and T^*_{NL}. We find that the crossover temperature obtained from the superfluid data T^*_{expt}, is closer to T^*_{NL} than to T^*_{imp}. This gives evidence for nonlocal behavior in a *d*-wave superconductor. This is a significant result, providing experimental support for the well-known and widely mentioned KL nonlocal theory. It provides an entirely different explanation, with totally different physics compared to the widely-accepted RIS theory, of the frequently observed crossover from linear to quadratic behavior in penetration depth measurements of unconventional superconductors. However, we must point out that since the coefficients calculated in the RIS theory are approximations, it is still possible that impurity scattering can explain the crossover effect [39]. Some of the results of this chapter have been published in Physical Review B, volume 67, article number 014527 (2003).

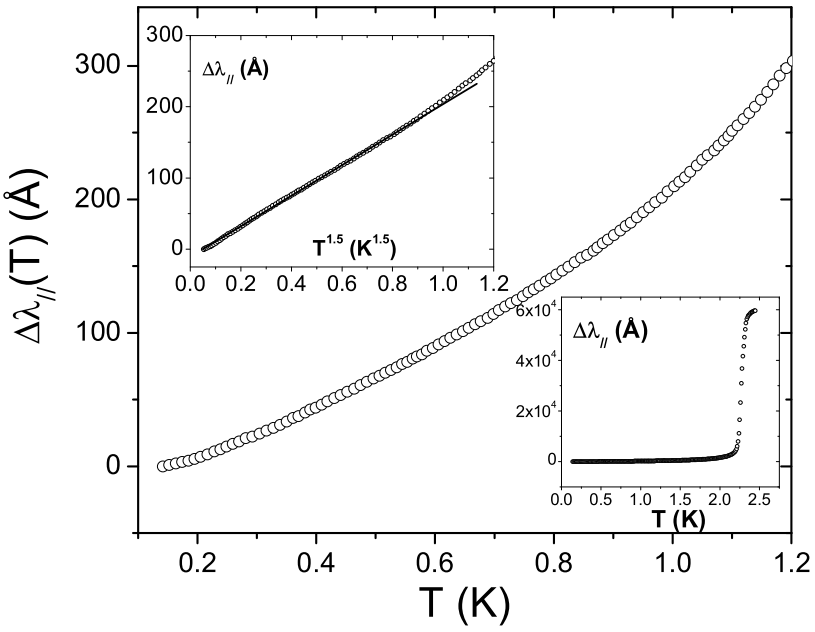

Figure 4.2: Low-temperature dependence of the in-plane penetration depth $\Delta\lambda_{\parallel}(T)$. Lower inset shows $\Delta\lambda_{\parallel}(T)$ over the full temperature range. Upper inset shows $\Delta\lambda_{\parallel}(T)$ vs $T^{1.5}$ in the temperature range (0.14–1.13) K. The solid line is a guide to the eye.

4.2 Data and Analysis

Details of sample growth and characterization are described in Refs. [31, 40]. The samples arrived as very nice rectangular (almost square) platelets of dimensions $\sim 0.75 \times 0.75 \times 0.09$ mm^3. SEM/EDX analysis on the surface did not reveal any impurities. The samples were run "as is", i.e. we did not attempt to cut, polish or clean the surface. Fig. 4.2 shows $\Delta\lambda_{\parallel}(T)$ as a function of temperature. We see that $\Delta\lambda_{\parallel}(T)$ varies strongly at low temperatures, inconsistent with the exponential behavior expected for isotropic *s*-wave superconductors. On the other hand, the variation is not linear, but has an obvious upward curvature, unlike the low-temperature behavior expected for pure *d*-wave superconductors. A fit of the low temperature data to a variable power law, $\Delta\lambda_{\parallel}(\mathrm{T}) = a + bT^n$ yields $n = 1.43 \pm 0.01$ for sample 1 and 1.57 ± 0.01 for sample 2. The upper inset of Fig. 4.2 shows this approximate $T^{3/2}$ behavior for sample 1. Kosztin *et. al.* [41, 42, 43] have proposed a

theory that gives a $T^{3/2}$ term from the gradual evolution of the pseudogap above T_c to the superconducting gap below T_c. While resistivity measurements suggest the possibility of a pseudogap in $CeCoIn_5$ [44], which renders this interpretation feasible, a decrease in Knight shift was observed only starting at T_c [38]. We take the latter to rule out a pseudogap mechanism.

Before considering novel excitation processes, we note the important distinction between $\Delta\lambda(T)$, which is directly measured, and the superfluid density $[\rho(T) = \lambda^2(0)/\lambda^2(T)]$ which can be inferred only with the knowledge of $\lambda(0)$ [45]. In the *d*-wave model, even if ρ_s varies strictly with T, i.e. ρ_s=1 $-$ $\alpha T/T_c$, the penetration depth is non-linear: $\lambda(T) = \lambda(0)[1+1/2\ (\alpha T/T_c) + 3/8\ (\alpha T/T_c)^2+...]$. Hence there is always a quadratic component to λ whose strength depends on α, which in the *d*-wave model, is inversely proportional to $d\Delta(\phi)/d\phi|_{node}$, the angular slope of the energy gap at the nodes [16]. If $\rho_s(T)$ is linear in T, there is no need to invoke another mechanism.

To extract the in-plane superfluid density from our data, we need to know $\lambda_\parallel(0)$. For a quasi-2D superconductor with a cylindrical Fermi surface and the material parameters in Ref. [35] and [46], we obtain $\lambda_\parallel(0) = 2600$ Å, considerably larger than the experimentally obtained value of 1900 Å [34]. This along with a large heat-capacity jump at T_c leads us to consider strong-coupling corrections as listed below [47, 48]:

$$\eta_{Cv}(\omega_0) = 1 + 1.8\left(\frac{\pi T_c}{\omega_0}\right)^2\left(\ln\left(\frac{\omega_0}{T_c}\right) + 0.5\right), \tag{4.3}$$

$$\eta_{\Delta}(\omega_0) = 1 + 5.3\left(\frac{T_c}{\omega_0}\right)^2\ln\left(\frac{\omega_0}{T_c}\right), \tag{4.4}$$

$$\eta_{\lambda}(\omega_0) = \frac{\sqrt{1 + (\frac{\pi T_c}{\omega_0})^2(0.6\ln(\frac{\omega_0}{T_c}) - 0.26)}}{1 + (\frac{\pi T_c}{\omega_0})^2(1.1\ln(\frac{\omega_0}{T_c}) + 0.14)}, \tag{4.5}$$

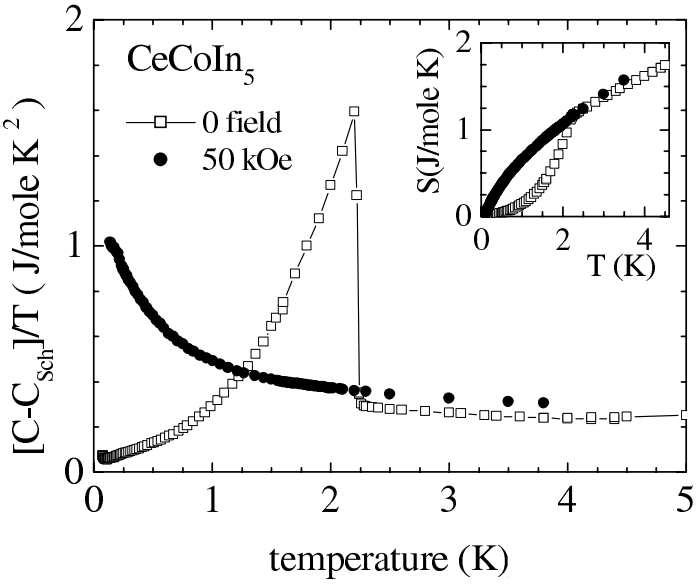

Figure 4.3: C/T vs T for $CeCoIn_5$. For both the zero-field (open squares) and 50 kOe (solid circles) data, a nuclear Schottky contribution, due to the large nuclear quadrupolar moment of In, has been subtracted. Notice that in the normal state, C/T is not a constant below T_c. The inset shows the entropy recovered as a function of temperature in the superconducting (open squares) and field-induced normal (solid circles) states. Taken from Ref. [31].

each η represents the correction to the corresponding BCS value

$$\left(\frac{\Delta C}{\gamma T_c}\right)^{sc} = \left(\frac{\Delta C}{\gamma T_c}\right)^{BCS} \eta_{Cv} \tag{4.6}$$

$$\Delta_0^{sc} = \Delta_0^{BCS} \eta_\Delta \tag{4.7}$$

$$\lambda^{sc}(0) = \lambda^{BCS}(0) \eta_\lambda. \tag{4.8}$$

If we take the experimental value of $\Delta C/\gamma T_c = 4.5$ [31], then Eqn. 4.3 gives the characteristic (equivalent Einstein) frequency $\omega_0 = 9.1$ K and $\lambda_{\|}^{sc}(0) = 1500$ Å. However, Petrovic *et. al.* [31] argued that since C/T increases with decreasing temperature (see Fig. 4.3), the specific heat coefficient γ is temperature-dependent below T_c. This effect calls into question simple estimates of strong-coupling corrections for $CeCoIn_5$. A better estimate is to use $\Delta C/\Delta S$ in place of $\Delta C/\gamma T_c$, where ΔS is the measured change in entropy of the sample from $T = 0$ to T_c. Ref. [31] then gives $\Delta C/\Delta S = 2.5$, so that $\omega_0 = 17.9$ K, resulting in

$\Delta_0^{sc} = 2.1 k_B T_c$ and $\lambda_\parallel^{sc}(0) = 2000$ Å. On the other hand, the larger ΔC of Ref. [33] yields $\Delta C/\Delta S = 2.8$ and $\omega_0 = 15.4$ K, leading to $\Delta_0^{sc} = 2.2 k_B T_c$ and $\lambda_\parallel^{sc}(0) = 1900$ Å. These values of $\lambda_\parallel^{sc}(0)$ are close to that obtained by Ormeno *et. al.* [34].

Although we will argue that nonlocal effects are important, we will refer to $(\lambda_\parallel(0)/\lambda_\parallel(T))^2$ as the "superfluid density." Fig. 4.4 shows the calculated behavior of that quantity using the three values of $\lambda_\parallel(0)$ obtained above. We follow the procedure in Ref. [45] to compute the experimental superfluid density, using the $T^{3/2}$ fit to estimate the small difference between $\lambda_\parallel(0)$ and $\lambda_\parallel(0.14\text{ K})$. In each case, $\rho(T)$ is clearly not linear in T.

Non-linearity in $\rho(T)$ can arise from a crossover from an intermediate-temperature (pure) linear-T behavior to, for example, low-temperature (impurity-dominated) quadratic behavior as pointed out by Hirschfeld and Goldenfeld [18]. Experimentally, i.e. from raw data, one can interpolate between these two regions using

$$\lambda = \lambda_0 + \frac{bT^2}{T^*_{expt} + T}, \tag{4.9}$$

where T^*_{expt} is the crossover temperature. In terms of superfluid density, one obtains [45]

$$\Delta\rho_\parallel(T) = \frac{\alpha T^2/T_c}{T^*_{expt} + T}. \tag{4.10}$$

In terms of material parameters, the RIS theory predicts for the crossover temperature, in the small-impurity-concentration limit $\Gamma/\Delta_0 \ll 1$ (see Section 2.6.1)

$$T^*_{imp} \approx 0.83\sqrt{\Gamma\Delta_0} \tag{4.11}$$

which is identical to Eqn. 2.69.

A much more provocative source of the crossover of Eqn. 4.10 was suggested by KL [20], who showed that for d-wave superconductors, nonlocal effects change the linear behavior to quadratic below a crossover temperature $T^*_{NL} = \Delta_0\xi_\parallel(0)/\lambda_\parallel(0)$.

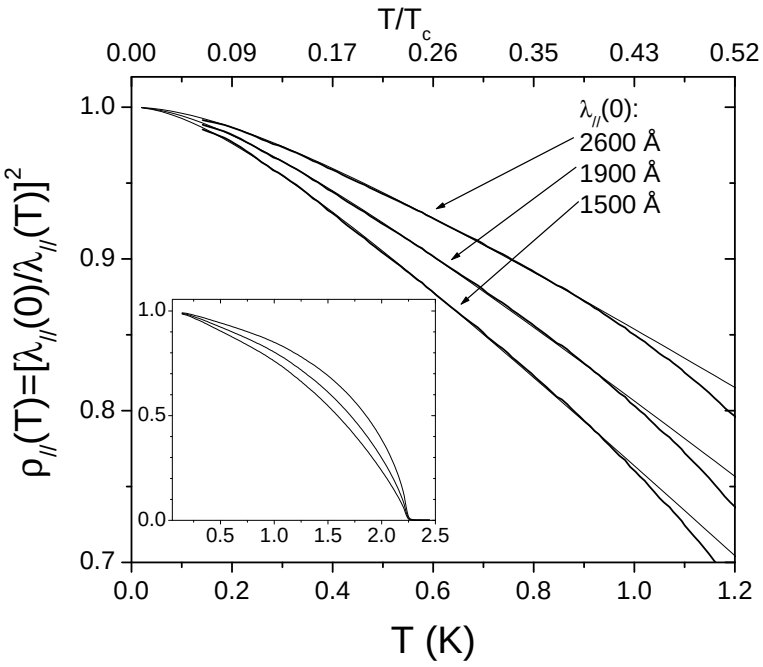

Figure 4.4: Low-temperature in-plane superfluid density $\rho_{\|}$(T) = $[\lambda_{\|}^2(0)/\lambda_{\|}^2$(T)] calculated from $\Delta\lambda_{\|}(T)$ data in Fig. 1 (thick lines). The thin lines correspond to fits to data using Eqn. 4.10, using three values of $\lambda_{\|}(0)$. Inset shows $\rho_{\|}$(T) over the full temperature range.

The solid lines in Fig. 4.4 are fits to Eqn. 4.10 and are very good for all three values of $\lambda_{\|}(0)$. The value of α varies from ∼0.5 to 0.7, the smallest value of α belonging to the largest value of $\lambda_{\|}(0)$. The value of α obtained is similar to that found for $YBa_2Cu_3O_{6.95}$ ($\alpha \sim 0.6$) [19, 49], but smaller than that of $Tl_2Ba_2CuO_{6+\delta}$ ($\alpha \sim 1.0$) [50] and K-$(ET)_2$Cu[N$(CN)_2$]Br ($\alpha \sim 1.2$) [45]. The value of T^*_{expt} varies less across the three $\lambda_{\|}(0)$ values, from 0.32 K to 0.42 K. These values of T^*_{expt}/T_c (∼0.14–0.18) differ from the cuprates [51, 19, 50] and the organic superconductor K-$(ET)_2$Cu[N$(CN)_2$]Br (∼0.05), where impurity scattering is presumed to be the source. Further, thermal conductivity measurements [35] puts an upper limit of 20 ppm on the impurity concentration, in the unitary (strong) scattering limit. This gives, in the RIS (or dirty *d*-wave) model [18], a unitary-limit scattering rate $\Gamma = \frac{n_{imp}n}{\pi N_0} \sim 1.5 \times 10^8$ s^{-1} from Eqn. 2.67. To get this value of Γ we used $n_{imp} = 20 \times 10^{-6}$

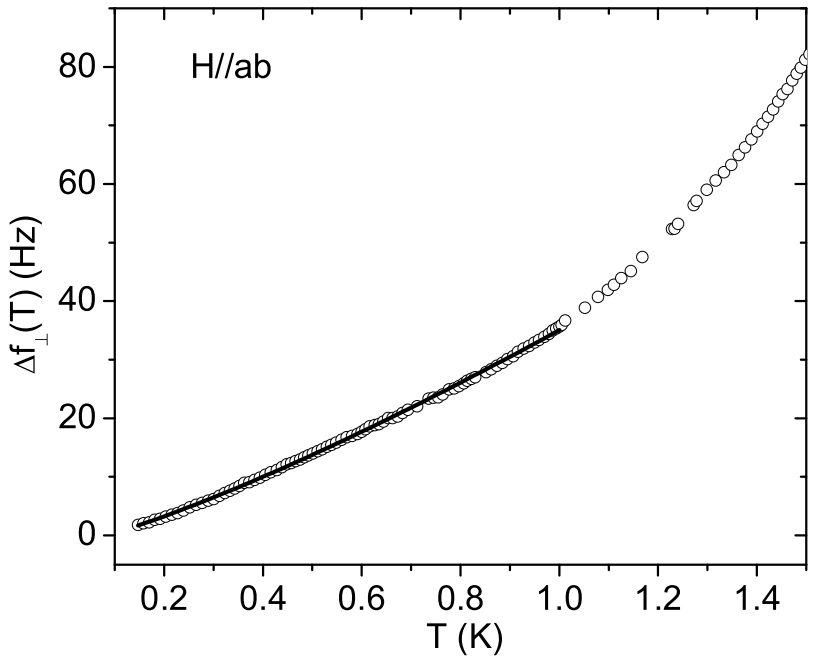

Figure 4.5: Low-temperature dependence $\Delta f_\perp(T)$ as defined in Eqn. 4.13, in the $H \perp c$ orientation. Note that this is raw data, without subtracting the $\lambda_\parallel$ component. Solid line is a variable-power law fit from 0.14 K to 1 K, where $n \approx 1.25$.

and $N_0 = 4.774 \times 10^{35}$ (erg cm^3)$^{-1}$ from Ref. [35]. We also estimated the value of n via the relation (in SI units)

$$\frac{1}{2} m_{eff} v_F^2 = \frac{\hbar^2}{2m_{eff}} (3\pi^2 n)^{2/3} \tag{4.12}$$

to obtain $n = 1.15 \times 10^{22}$ cm^{-3}. m_{eff} and v_F were also taken from Ref. [35]. This implies $\Gamma/\Delta_0 \sim 10^{-4} \ll 1$, enabling us to use Eqn. 4.11 to obtain an upper limit for $T^*_{imp} \sim 65$ mK. This is about 5 times smaller than the experimentally obtained values above, suggesting that the sample is too clean for the dirty d-wave model to be applicable. However, the coefficients calculated in RIS theory are approximations [39]. Hence impurity scattering can still be a possible explanation for the crossover effect.

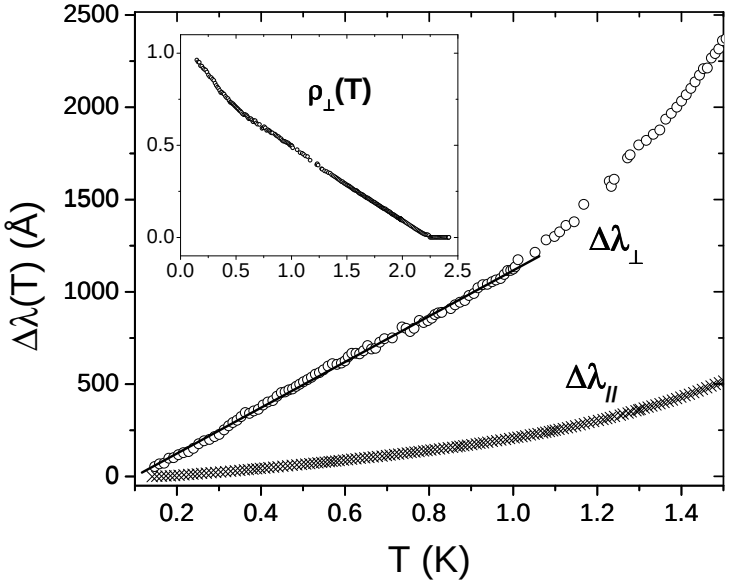

Figure 4.6: Low-temperature dependence of inter-plane (open circles) penetration depth $\Delta\lambda_\perp(T)$, after subtracting the in-plane component. In-plane $\Delta\lambda_\parallel(T)$ (crosses) data is also shown for comparison. Solid line is a linear fit from 0.14 K to 1 K. Inset shows inter-plane superfluid density $\rho_\perp(T)$ for the whole temperature range.

Besides impurity scattering, we turn to another effect — nonlocal electrodynamics, that might be the source of the crossover in $\rho_\parallel(T)$. For a *d*-wave superconductor *with line nodes along the c-axis*, nonlocality is expected to be relevant only when the applied magnetic field is oriented parallel to the *c*-axis, while the effect of impurities should not depend on the orientation of the field. As KL noted, if T^*_{expt} in $\Delta\lambda_\parallel(T)$ is noticeably smaller in the $H \perp c$ than in the $H \parallel c$ configuration, then we may conclude that the observed effect is due mainly to nonlocal electrodynamics and not to impurities. For $H \perp c$, screening currents flow both parallel and perpendicular to the *c*-axis, mixing $\lambda_\parallel$ and $\lambda_\perp$ with the frequency shift given by [29]

$$\frac{\Delta f_\perp}{f_0} = \frac{V_s}{2V_c}\left(\frac{\Delta\lambda_\parallel^{H\perp c}}{d} + \frac{\Delta\lambda_\perp}{w}\right), \tag{4.13}$$

where V_s is the effective sample volume, V_c is the effective coil volume, f_0 is the resonant frequency with the sample absent, and $\Delta f_\perp \equiv \Delta f(H \perp c)$.

Unfortunately, we do not know the temperature dependence of $\Delta\lambda_\perp$, hence we cannot extract out $\Delta\lambda_\parallel^{H\perp c}$ using this method. It is however, instructive to plot $\Delta f_\perp(T)$, as shown in Fig. 4.5. Fitting the data from 0.14 K to 0.9 K to the interpolation formula Eqn. 4.9 gives $T^* = 0.22$ K — this is less than 0.32 K obtained for the $H \parallel c$ orientation, though, once again, we emphasize that the graph is *not* proportional to $\Delta\lambda_\parallel^{H\perp c}$, but an admixture of $\Delta\lambda_\parallel^{H\perp c}$ and $\Delta\lambda_\perp$. Equivalently, fitting the same range of data to the variable-power law gives $n = 1.17$, while fitting to 1 K gives $n = 1.25$. Both fitted values of n are less than 1.5. This suggests that in this $H \perp c$ orientation, (1) $\Delta\lambda_\parallel(T) \propto T^n$, $n < 1.5$, *and/or* (2) $\Delta\lambda_\perp(T)$ $\propto T^n$, $n < 1.5$, to give a net power of ~ 1.2. It is thus possible that $\Delta\lambda_\parallel(T) \propto T$ in the $H \perp c$ orientation, lending credence to the KL theory.

It is interesting to use Eqn. 4.13 to extract $\Delta\lambda_\perp$, if we subtract out the $\Delta\lambda_\parallel^{H\perp c}$ from $\Delta f_\perp$, *assuming that* $\Delta\lambda_\parallel^{H\perp c}$ *follows the same temperature dependence as in the* $H \parallel c$ *case, i.e.* $\Delta\lambda_\parallel^{H\perp c} \propto T^{1.5}$. Fig. 4.6 shows the resulting inter-plane penetration depth $\Delta\lambda_\perp$ of $CeCoIn_5$ down to 0.14 K. It is clearly linear in T from 0.14 K to 1 K. So if one is able to measure $\Delta\lambda_\perp(T)$ and obtains a low-temperature linear behavior, it shows that $\Delta\lambda_\parallel^{H\perp c}(T)$ still follows a $T^{3/2}$-dependence. If this is the case, i.e. $\Delta\lambda_\parallel^{H\perp c}(T)$ and $\Delta\lambda_\parallel^{H\parallel c}(T)$ follow the same power law, then we can conclude that nonlocality is *not* the mechanism for the crossover from linear to quadratic penetration depth temperature dependence in $CeCoIn_5$. To obtain the superfluid density, we estimate $\lambda_\perp(0)$ from the H_{c2} anisotropy of $\sim$2.3 [33], and the fact that $\lambda(0) \propto \sqrt{H_{c2}(0)}$ [9], obtaining $\lambda_\perp(0) \sim 2700$ Å. This is close to the value of $\sim$2800 Å obtained from microwave measurements in the planar geometry [52]. A calculation of $\rho_\perp$ is shown in the inset of Fig. 4.6: the upturn below 0.5 K is an artifact of the choice of $\lambda_\perp(0)$. A larger value of $\lambda_\perp(0)$ would remove this feature, but there is no justification for doing so.

To test the validity of the nonlocal scenario, we have to resort to estimating T^*_{NL} using strong-coupling parameters, and comparing it with T^*_{expt} and T^*_{imp}. From the measured $H_{c2}(0)[001]$ value of 49.5 kOe, the coherence length $\xi_\parallel(0)$ is calculated to be 82 Å [33]. Together with the earlier-derived values of $\Delta_0^{sc} = 2.2 k_B T_c$ and $\lambda_\parallel^{sc}(0) = 1900$ Å, we find the

strong-coupling nonlocal crossover temperature $T^*_{NL} = \Delta^{sc}_0\ \xi_\parallel(0)/\lambda^{sc}_\parallel(0) = 0.22$ K. Using a weak-coupling d-wave $\Delta(0) = 2.14 k_B T_c$, we get $T^*_{NL} = 0.26$ K. We regard either value to be satisfactorily close to the experimental value of 0.32 K. Note that the value of $\xi_\parallel(0)$ is different from both the calculated BCS value of 58 Å [35] and the strong-coupling corrected value of ∼50 Å [47]. This is not surprising since the BCS expressions [47] assume a spherical FS, while LDA band structure reveals a very complicated FS with contributions from three different bands [53].

Finally, we point out that since since the normal-state electronic specific heat $C_{el} \neq \gamma T$ at low temperatures, as seen in Fig. 4.3, $CeCoIn_5$ thus exhibits non-Fermi-liquid (NFL) behavior. The impact of NFL on predictions of the superconducting state, particularly the applicability of the RIS and KL theories, is therefore not clear [39]. Özcan *et al.* attempted to explain their penetration depth data using non-Fermi-liquid behavior and quantum criticality [52].

4.3 Conclusion and Future Work

In conclusion, we report measurements of the magnetic penetration depth λ in single crystals of $CeCoIn_5$ down to ∼0.14 K using a tunnel-diode based, self-inductive technique at 28 MHz. The in-plane penetration depth ($\lambda_\parallel$) exhibits a crossover between linear (at high T) and quadratic (low T) behavior with a crossover temperature $T^*_{expt} \approx 0.32$ K. Such behavior can arise in a superconductor with nodes in the gap either in a dirty d-wave model or from nonlocal electrodynamics. We find that T^*_{expt} is closer to T^*_{NL} (0.26 K) than to T^*_{imp} ($\leq$ 0.065 K). We conclude, however, that *both* impurity scattering (T^*_{imp}) and nonlocality (T^*_{NL}) give values of the crossover temperatures which are comparable to experimental data, since the coefficients calculated in RIS theory are approximations [39]. Our data might provide experimental support for the well-known and widely mentioned KL nonlocal theory. We also demonstrate that strong-coupling corrections are required to reconcile various experimentally

determined superconducting parameters. The present result should reenergize the search for nonlocal effects in other unconventional superconductors.

Finally, for future work, Goldenfeld suggested the exploration of how the temperature dependence of λ depends on impurity concentration [39]. Firstly, if the superconducting transition temperature T_c varies dramatically with impurity concentration, then we can conclude that there is no resonant impurity scattering in this material. If the opposite is true, then resonant impurity scattering is present, and the assumption of RIS theory is valid, for this material. Secondly, with sufficient impurity concentration, any nonlocal effects would be washed out, since the effective coherence length becomes finite even at the nodes. If one still sees the crossover effect, this time with a larger T^*_{expt}, i.e. more of the $T^{3/2}$ region becomes T^2, then it must be due to impurity scattering rather than nonlocality.

For this project I acknowledge Professors R. Prozorov, Q. Chen and N. Goldenfeld for useful discussions. I thank Dr. J. Sarrao for providing the samples. Work at Los Alamos was performed under the auspices of the U.S. Department of Energy.

Chapter 5

$PrOs_4Sb_{12}$

5.1 Introduction

The recent discovery of the Heavy Fermion (HF) skutterudite superconductor (SC) $PrOs_4Sb_{12}$ [54, 55] has attracted much interest due to its differences compared with the other unconventional SC, and in particular, the HFSC. Conventional superconductivity is mediated by the electron-phonon interaction, whereas superconductivity in the unconventional SCs are widely thought to be magnetically-mediated, i.e. via interaction of the local magnetic moments with the conduction electrons. Because $PrOs_4Sb_{12}$ has a nonmagnetic ground state of localized f electrons in the crystalline electric field, its HF behavior, and consequently the origin of its superconductivity, has been attributed to the interaction between the electric quadrupolar moments of Pr^{3+} and the conduction electrons. It is thus a candidate for the first SC mediated by quadrupolar fluctuations, i.e. by neither electron-phonon nor, as with other HFSC, magnetic interactions.

Recent experiments on $PrOs_4Sb_{12}$ give conflicting evidences to the nature of the SC gap. Muon-spin rotation (μSR) measurements revealed a low-temperature exponential behavior, suggesting isotropic pairing (either s or p-wave) [56]. Scanning tunneling spectroscopy measurements also measured a density of states (DOS) with no low-energy excitations with a well-developed SC gap over a large part of the Fermi surface (FS) [57]. The absence of a Hebel-Slichter peak and the non-T^3 behavior of $1/T_1$ in nuclear quadrupolar resonance (NQR) experiments suggest that $PrOs_4Sb_{12}$ has either a full gap or point nodes, but not

line nodes, at zero field [58, 59]. If $PrOs_4Sb_{12}$ has an isotropic gap, then it is unique among HFSC, suggesting the possibility of (a) an important difference in superconducting properties between HFSC with magnetic and non-magnetic f-ion ground states, and (b) a correlation between pairing symmetry (isotropic or nodal gap) and mechanism (quadrupolar or magnetic fluctuations) of superconductivity [56].

Unlike the μSR and NQR results, angle-dependent thermal conductivity measurements [60] revealed two distinct SC phases with different symmetries, a phase transition between them, and presence of *point* nodes. In the high-field phase four point nodes ([100] and [010] directions) have been observed, whereas there are only two point nodes ([010] directions only) in the low-field phase. Specific-heat data [54] also show a low-temperature power law behavior, suggesting the presence of nodes. Another recent μSR experiment revealed the spontaneous appearance of static internal magnetic fields below T_c, providing evidence that the SC state is a time-reversal-symmetry-breaking (TRSB) state [61].

In this chapter, we present high-precision measurements of penetration depths $\lambda(T)$ of $PrOs_4Sb_{12}$ at temperatures down to 0.1 K. The ac field was applied along all three crystallographic axes. In all three field orientations both $\lambda(T)$ and superfluid density $\rho_s(T)$ tends to follow a quadratic power law, suggesting that the SC gap has nodes on the FS. ρ_s for various gap functions has been calculated, and data are best fit by the ^{3}He A-phase-like gap, with two point nodes in the [010] directions. Our data thus puts $PrOs_4Sb_{12}$ in line with other HFSC, in that they all have nodes on the FS, despite the proposed non-magnetic nature of the mechanism of its superconductivity. The results of this chapter have been published in Physical Review Letters, volume 91, article number 247003 (2003).

5.2 Data and Analysis

Details of sample growth and characterization are described in Ref. [62]. The de Haas-van Alphen (dHvA) effect was observed from samples of the same batch, reflecting the high

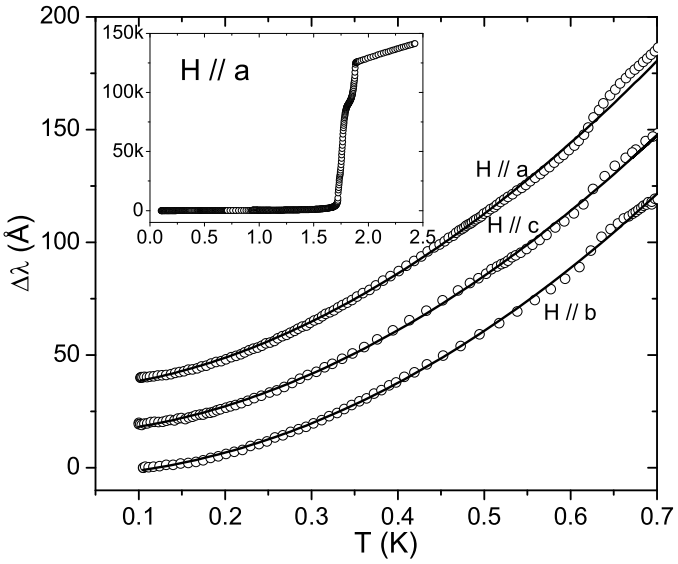

Figure 5.1: Low-temperature dependence of the penetration depth $\Delta\lambda(T)$ for field orientations $H \parallel a, b, c$. The curves have been offset for clarity. The solid lines are fits to $\Delta\lambda(T) = A + BT^n$ from 0.1 K to 0.55 K. Upper inset shows $\Delta\lambda_a(T)$ over the full temperature range.

quality of the samples [62]. Moreover, the mean free path was estimated from dHvA data to be ∼1300 Å, which is much larger than the coherence length ξ_0 (∼120 Å), showing that the sample is in the clean limit [63, 54]. Further, the samples were given to us "as is", i.e. they were not cut either mechanically, chemically or electrically; neither were they polished in any way. Previous samples which were cut using spark-cutting, and polished, did not give us a smooth signal.

I obtain the value of G_a using the method in Chapter 2. The value of G_a obtained this way has an error of ±10 %, since our sample has a rectangular basal area instead of square [29]. To obtain G_b and G_c we make use of the cubic symmetry of the crystal and assume that the total change in penetration depth from the three orientations are equal, i.e. $\Delta\lambda_a(T_c) = \Delta\lambda_b(T_c) = \Delta\lambda_c(T_c)$. From this equality, and the value of G_a, we can calculate G_b and G_c.

Fig. 5.1 shows $\Delta\lambda_i(T)$ as functions of temperature. All three curves vary strongly at low temperatures, inconsistent with exponential behavior expected for isotropic s-wave su-

perconductors. On the other hand, the variation is not linear, but has an obvious upward curvature, unlike the low-temperature behavior expected for pure d-wave superconductors. A fit of the low temperature data (up to 0.55 K $\approx 0.3\ T_c$) to a variable power law, $\Delta\lambda$(T) $= A + BT^n$ yields $n = 1.9 \pm 0.1$ for $H \parallel a, b$, and $n = 2.0 \pm 0.1$ for $H \parallel c$. The uncertainty in n is *not* a consequence of the uncertainty in G, but rather of the somewhat uneven faces of the crystal and the range of fit. Within the uncertainty in G the three curves are consistent with one another. There is also a small upturn near 0.62 K, which might distort the low-temperature fit and cause the power law to deviate from T^2. The NQR spin-lattice relaxation rate also changes around this temperature, however, the origin is not clear at present [58, 63]. A non-unitary state has the unique feature that spin-up and spin-down Cooper pairs have different excitation gaps [64]. If the SC state in $PrOs_4Sb_{12}$ is a TRSB state, then this upturn may be due to the contribution from the smaller gap [61]. It is interesting to note that a fit of the $\Delta\lambda(T)$ from 0.6 K to 1.1 K, to the same variable power law, gives an exponent of about 3, consistent with $n \approx 4$ obtained for specific-heat data over the same temperature range [54].

Using the value of $\lambda(0) = 3440$ Å from μSR measurements [56], we calculated the superfluid density ρ_s from our data. We follow the procedure in Ref. [65] to compute the experimental superfluid density, using the T^2 fit to estimate the small difference between $\lambda(0)$ and λ(0.1 K). Fig. 5.2a shows $\rho_s(T)$ for all three field orientations at low temperatures. In each case, a fit of $\rho_s(T)$ to a variable power law, $\rho_s(T) = 1 - \alpha T^n$ also yields n ≈ 2, from 0.1 K ($\sim 0.05\ T_c$) to 0.55 K. Once again this suggests the presence of low-lying excitations, incompatible with an isotropic SC gap.

Several theoretical proposals have been put forward to understand the two SC phases [66, 67, 59]. To explain the behavior of the angle-dependent, magneto-thermal-conductivity

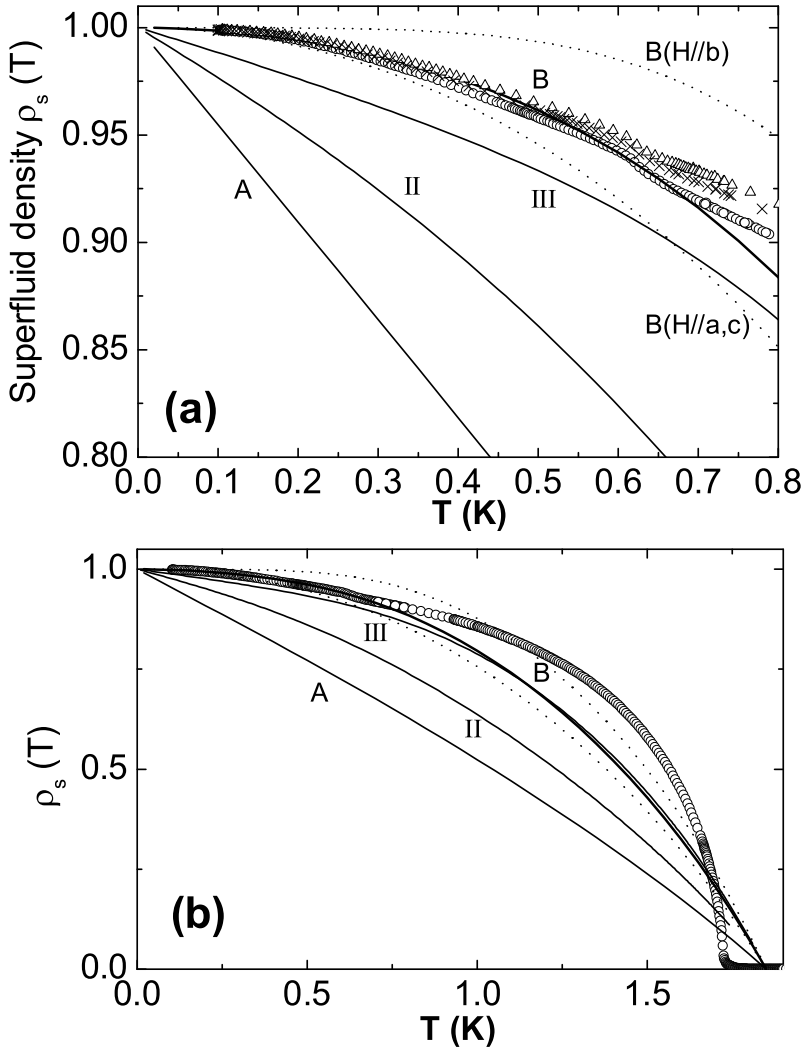

Figure 5.2: (a) Low-temperature superfluid density $\rho_s(T) = [\lambda^2(0)/\lambda^2(T)]$ calculated from $\Delta\lambda(T)$ data in Fig. 5.1, for all three field orientations. ($\bigcirc$) $H \parallel a$, ($\triangle$) $H \parallel b$, ($\times$) $H \parallel c$. Using $\Delta_0(0)/k_B T_c = 2.6$, the solid lines are the calculated effective superfluid density ρ_s^{eff} corresponding to gaps II, III, A and B. The dotted lines correspond to $\rho_s(H \parallel b)$ and $\rho_s(H \parallel a, c)$ for gap B. (b) The same calculated curves over the entire temperature range. Only the $\rho_s(T)$ data for $H \parallel a$ are shown.

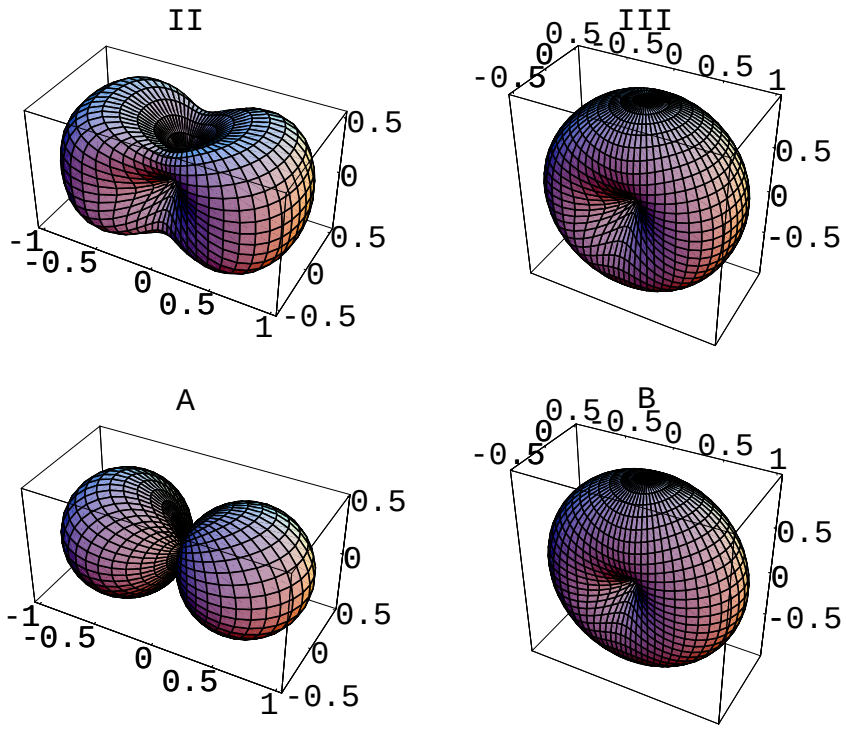

Figure 5.3: Polar plots of gap functions (II), (III), (A) and (B).

results [60], Maki *et al.* [66] proposed three possible SC gap functions for $PrOs_4Sb_{12}$. In particular, for the low-field (L) phase, two gap functions were proposed:

$$f(\mathbf{k}) = 1 - k_y^4 - k_z^4 \quad \text{(II)} \tag{5.1}$$

having four nodes, and

$$f(\mathbf{k}) = 1 - k_y^4 \quad \text{(III)} \tag{5.2}$$

with two point nodes. The gap function is $\Delta(\mathbf{k}) \equiv \Delta_0 f(\mathbf{k})$, with the form factor $f(\mathbf{k})$ normalized to unity and Δ_0 the temperature-*dependent* maximum gap value. As we will see, both

functions lead to a linear temperature dependence for the superfluid density. Consequently, we consider two further gap functions:

$$\mathbf{d}(\mathbf{k}) = \hat{y}k_a \quad \text{(A)}, \tag{5.3}$$

a line-node gap, and

$$\mathbf{d}(\mathbf{k}) = \hat{y}(k_a + ik_c) \quad \text{(B)}, \tag{5.4}$$

for which $\Delta(\mathbf{k}) = \Delta_0 \left|\boldsymbol{d}(\mathbf{k})\right|$. Gap B has two point nodes along the [010] directions and a gap dispersion identical to the superfluid ^{3}He A-phase, $\Delta(\mathbf{k}) = \Delta_0 \left|k_a \pm ik_b\right| = \Delta_0 \sin\theta$; hence, they give identical temperature dependences of ρ_s. Polar plots of these gap functions are shown in Fig. 5.3. We have assumed the gap maximum $\Delta_0(T)$ to have the form $\Delta_0(T) = \delta_{sc} k T_c tanh\left\{\frac{\pi}{\delta_{sc}}\sqrt{a(\frac{\Delta C}{C})(\frac{T_c}{T}-1)}\right\}$ [9], where $\delta_{sc} \equiv \Delta_0(0)/k_B T_c$ is the only variable parameter, $T_c = 1.85$ K, $a = 2/3$, and the specific heat jump $\Delta C/C = 3$ is an experimentally obtained value [68].

A problem arises immediately with point nodes. If there are only two point nodes in the [010] directions, breaking cubic symmetry, then one would expect $\Delta\lambda_b$ to tend toward an exponential temperature dependence at low temperatures. We show this in Fig. 5.2, where we have calculated the superfluid density for gap B for fields along [010] and either [100] or [001]. A measurement along [010] ($H \parallel b$) would indeed give exponential behavior while measurements in orthogonal directions ($H \parallel a, c$) give a strong temperature dependence. However, our experimental data show otherwise — there is an almost identical T^2 superfluid response in all three field orientations. While it is possible that, in the absence of an external agent, the sample will randomly choose one, *and only one*, axis along which to locate the nodes each time it becomes superconducting, it is much more likely to develop a domain structure. We attribute this to the fact that as the sample goes superconducting below T_c, cubic symmetry is broken due to the coupling between the SC order parameter and strain [67]. However, there is no guiding mechanism to suggest where in the *x, y* and *z* directions the point

nodes should be. The result is a domain structure in $PrOs_4Sb_{12}$ where each domain contains only two point nodes in one of the three possible crystallographic directions. The total superfluid response is thus the sum of T^2 contributions from each two-point-node domain, giving also a T^2 response, *independent of field orientation*. This coupling between the SC order parameter and strain is similar to the case of magnetostriction in ferromagnets. Such a situation also arises in Cromium (Cr) [69], where the coupling between the spin-density-wave (SDW) and strain wave causes the wave vector $\mathbf{Q}$ of the modulation to point along any $\{001\}$ direction in the bcc Cr lattice. In bulk Cr all three possible orientations occur with equal probability. A Cr single crystal thus has multiple domains, with each domain corresponding to one of three possible $\mathbf{Q}_x$, $\mathbf{Q}_y$ and $\mathbf{Q}_z$ regions [70] — the "poly-$\mathbf{Q}$" state. Tensile stress in applied along one cube axis while cooling through T_N, however, produces a "single-$\mathbf{Q}$" state with all domains having their $\mathbf{Q}$'s pointing in the same direction, along the stress axis [71]. Evidence that a domain with only two point nodes can form in $PrOs_4Sb_{12}$ was reported in Ref. [60], where nodes were seen only along a single [010] axis. We suggest that the experimental setup of Ref. [60] may have strained the sample to produce a single domain, analogous to the single-$\mathbf{Q}$ state of Cr.

Assuming the existence of domains, we plot an effective superfluid density ρ_s^{eff} by taking the average of [100], [010] and [001]-superfluid densities, with equal weight from each component. The superfluid densities in different directions are evaluated using the expression

$$\rho_s(H \parallel x) = 1 - \frac{3}{N_0}\sum_{\mathbf{k}}(\hat{k}_y^2 + \hat{k}_z^2)\frac{\partial f}{\partial E_{\mathbf{k}}}, \tag{5.5}$$

where *x, y, z* = any permutation of *a, b, c*. N_0 is the normal-state DOS at the FS, $f = [\exp(\mathrm{E}_{\mathbf{k}}/k_BT)+1]^{-1}$ is the Fermi function, and $E_{\mathbf{k}} = [\varepsilon^2(\mathbf{k}) + \Delta(\hat{\mathbf{k}}, T)^2]^{1/2}$ is the quasiparticle energy, and $\Delta(\hat{\mathbf{k}}, T)$ is each of the four gap functions mentioned earlier. For example, when

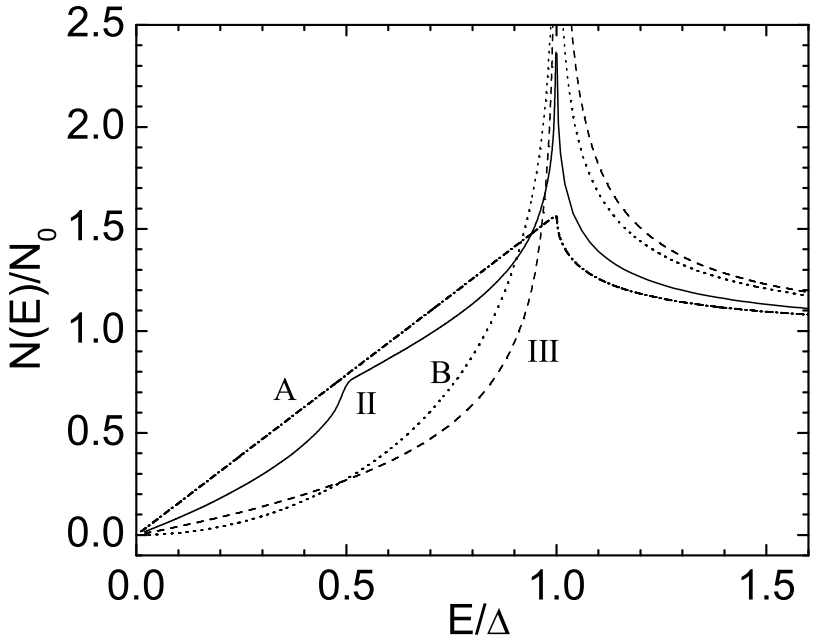

Figure 5.4: Quasiparticle DOS for the gap functions II (full line), III (short-dashed line), A (short-dash-dotted line) and B (short-dotted line).

$H \parallel a$, the screening currents are in the b and c directions. So for this case, $\hat{k}^2 = \hat{k}_y^2 + \hat{k}_z^2 = \sin^2\theta \sin^2\phi + \cos^2\theta$. Averaging it over the FS gives another factor $\frac{1}{2}$. Hence

$$\rho_s(H \parallel a) = 1 - \frac{3 \times 2}{2\pi} \int_0^{2\pi} \int_0^{\infty} \int_0^1 \frac{\partial f}{\partial E} \frac{1}{2} [(1 - \cos^2\theta) sin^2\phi + \cos^2\theta] d(\cos\theta) d\xi d\phi. \qquad (5.6)$$

The component superfluid densities for Gap B are shown as two dotted lines, and ρ_s^{eff} as a solid line, in Fig. 5.2. Clearly, the agreement between data and ρ_s^{eff} is very good. We chose the strong-coupling value $\delta_{sc} = 2.6$ here, taken from Ref. [58]. Using $\delta_{sc} = 2.1$ from Ref. [56] gives a worse fit. For the other gap functions, we also calculated ρ_s^{eff} (shown in Fig. 5.2) and $\rho_s(H \parallel a, b, c)$ (not shown here) — all of them give linear temperature dependences and fall far from the experimental data. The effective quasiparticle DOS for all four gap functions is also shown in Fig. 5.4. Our data therefore suggest that $PrOs_4Sb_{12}$ is a strong-coupling unconventional SC. The superfluid data are best fit with a ^{3}He A-phase-like gap, with two point nodes on its FS. Both the field-direction-independence of the superfluid data, *and* the nice fit of the data to ρ_s^{eff}, strongly suggest that $PrOs_4Sb_{12}$ has multidomains. Note that though Gap B is a unitary gap, our low-T data can also be fit [72] by the two-point-node L-phase *non-unitary* gap proposed by Ichioka *et al.* in Ref. [59], with similar DOS structure. Hence our data does not contradict the non-unitary result of Aoki *et al.* [61].

It is already apparent in Fig. 5.2a that the data deviate from the proposed gap function above 0.6 K. This is even clearer in Fig. 5.2b, which shows $\rho_s(T)$ for $H \parallel a$ from 0.1 K to T_c. The other two field orientations give almost identical temperature dependence. None of the four gap functions fits the data over this larger temperature range. This could be due to the opening up of the smaller gap caused by the non-unitarity of the SC state, as mentioned earlier. Also, strong changes in the mass renormalization in different sheets have been found in de Haas van Alphen experiments [62]. These changes may cause the distribution of values of the SC gap measured in tunneling measurements [57], and strengthens both the idea

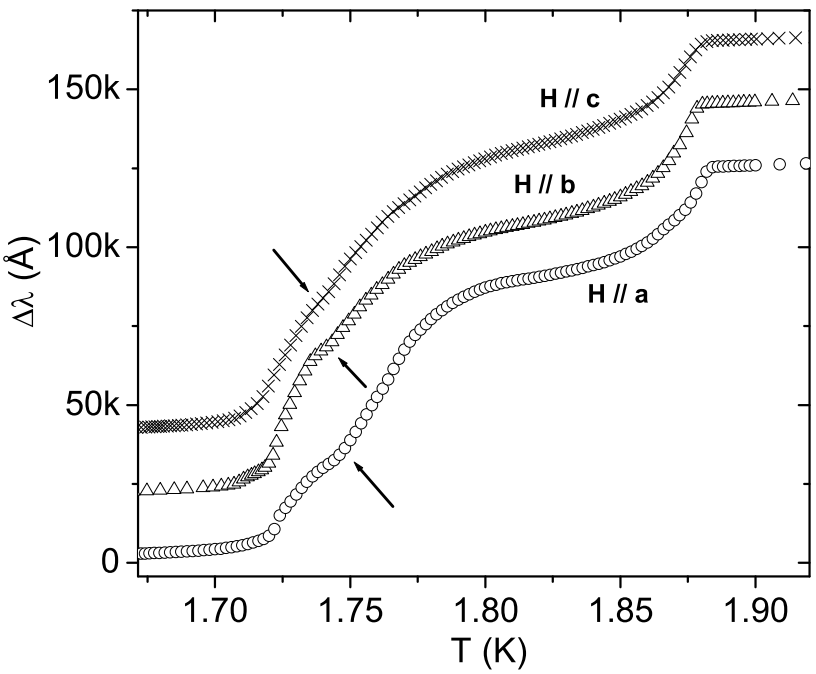

Figure 5.5: $\Delta\lambda(T)$ for all three field orientations near T_c. The curves have been offset for clarity. The arrows indicate the second superconducting transition at 1.74 K.

that the mass renormalization and superconductivity are of the same origin, i.e. that the quadrupolar fluctuations favor SC correlations, as well as the possible multiband character of superconductivity in this material [57]. Hence a multiband analysis, similar to those performed on MgB_2, might be required to fit the superfluid data over the entire temperature range.

Finally, we turn to the region near T_c. Fig. 5.5 shows $\Delta\lambda(T)$ near T_c for all three field orientations. Three features can be seen: the onset of superconductivity at 1.88 K, a strong but broad shoulder near 1.8 K, and finally a weak shoulder near 1.74 K (observable even in the $H \parallel c$ data). In another sample from the same batch, only the first and third features were observed. The 1.88 K and 1.74 K features confirm the two superconducting transitions seen in the specific-heat measurement [68], and suggested by angle-dependent thermal conductivity measurements [60]. The origin of the 1.8 K shoulder is unknown. In

the $\rho_s(T)$ plot, ρ_s already approaches zero near 1.7 K. So these features were not discernible there. Also, we did not see any anomaly around $T^* = 2.3$ K that was observed in Ref. [58].

5.3 Conclusion

In conclusion, we report measurements of the magnetic penetration depth λ in single crystals of $PrOs_4Sb_{12}$ down to 0.1 K using a tunnel-diode based, self-inductive technique at 21 MHz, with the ac field applied along the a, b and c directions. In all three field orientations λ and superfluid density ρ_s tend to follow a quadratic power law. We have calculated ρ_s for various gap functions, finding that the data are best fit by the ^{3}He A-phase-like gap function with two point nodes on the FS. We also observe the double transitions near 1.75 K and 1.85 K seen in other measurements.

For this project I acknowledge Dr. D. Lawrie and Professor Y. Matsuda for useful discussions. Special thanks to Professor K. Machida for significant contributions. I thank Professor H. Sugawara for giving us the samples.

Chapter 6

YNi_2B_2C & $LuNi_2B_2C$: Multi-band superconductors?

6.1 Introduction

The family of quarternary compounds $RENi_2B_2C$ (RE = rare-earth) have attracted much interest due to the considerable interaction among their superconducting and magnetic properties [73]. The non-magnetic members of the family, YNi_2B_2C and $LuNi_2B_2C$, serve as useful candidates for elucidating the symmetry of the order parameter, since there is no magnetic signal to interfere with the superconducting one. Generally it has been thought that the gap function of these materials exhibits an isotropic *s*-wave symmetry [74, 75, 76, 77]. However, some experiments have shown evidence of low-energy quasiparticle excitations: power-law temperature dependence, and$\sqrt{H}$-dependence, of the specific heat [78, 79]; non-BCS gap ratio from microwave impedance measurements [80]; scattering below the energy gap from Raman measurements [81]. Ultra-high resolution photoemission experiments on $Y(Ni_{1-x}Pt_x)_2B_2C$ [82] gave very strong evidence of an extremely anisotropic *s*-wave gap, though the gap parameters giving the best fit are *d*-wave-like. Thermal conductivity measured down to 70 mK also offered compelling evidence for the presence of delocalized quasiparticles at the lowest energies, suggesting that the gap minimum Δ_{min} is at least 10 times smaller than the gap maximum, and possibly going to zero at nodes [83]. Izawa et al. reported a field-directional-angle dependence of the thermal conductivity in YNi_2B_2C that

suggested point nodes along <100> directions [84]. Park *et al.* also reported field-directional-angle dependence of heat capacity in YNi_2B_2C that showed 4-fold symmetry [85]. Local density approximation (LDA) band structure calculations predict a rather complicated band structure near E_F, with at least four bands crossing the Fermi level [86]. DHvA data [87] also clearly showed the presence of six different sections $F_\alpha, \ldots, F_\eta$ with roughly two or three groups of Fermi velocities. However, the multiband character and the anisotropic Fermi surface have been widely ignored in various experimental analysis. One exception is Shulga *et al.* [88], who used an effective two-band model to quantitatively explain upper critical field peculiarities of superconducting YNi_2B_2C and $LuNi_2B_2C$. Moreover, Terashima et al. [89] observed dHvA oscillations from a small electron pocket (named α) in the vortex state down to 2 T. This surface encloses only 0.3% of the first BZ, and contributes little to the density of states (DOS), and so would hardly influence the average superconducting gap. They argue that the gap opening on this α Fermi sheet is much smaller than the gap on other parts of the FS.

Here we present and analyze theoretically data of the in-plane magnetic penetration depth $\lambda(T)$ in high-purity single crystals of YNi_2B_2C (T_c = 15.9 K) and $LuNi_2B_2C$ (T_c = 15.5 K) from T_c down to 97 mK. Besides the usual diamagnetic drop of $\lambda(T)$ at T_c, a second drop around 1 K was observed. The magnitude of this drop is $\sim$1% of the total signal. We show that this feature cannot be explained by a *single* anisotropic *s*-wave superconducting gap. We also consider a *second* gap with a much smaller magnitude that reveals itself at $\sim$1 K. We explore whether a two-gap model first suggested by Suhl *et al.* [90] can quantitatively explain the data.

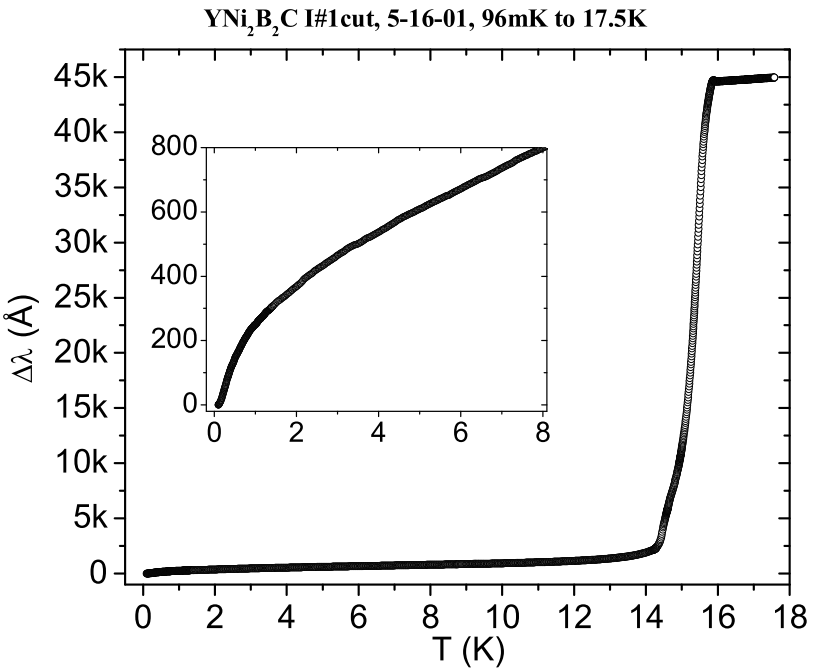

Figure 6.1: $\Delta\lambda(T)$ for $T = 0.1$ K–17.5 K. Inset shows the low-temperature region in greater detail.

6.2 Data and Analysis

6.2.1 YNi_2B_2C

Fig. 6.1 shows $\Delta\lambda(T)$ as a function of temperature for the sample. The inset shows the low-temperature region. We see that as T approaches 1 K, $\Delta\lambda(T)$ does not flatten off exponentially, but instead decreases further as T goes down to 100 mK. This might be indicative of either a second superconducting transition, or the opening up of a second superconducting gap at $\sim$1 K.

Suhl *et al.* considered a multi-band BCS model to explain certain experimental results of transition metals [90]. For the two-band case, the equations for the two gaps A and B are

$$\begin{aligned} A &= V_{11}N_1AF(A) + V_{12}N_2BF(B) \\ B &= V_{21}N_1AF(A) + V_{22}N_2BF(B)\ , \end{aligned} \tag{6.1}$$

where

$$F(A) = \int_0^{\hbar\omega} d\varepsilon \frac{\tanh\left[\frac{(\varepsilon^2+A^2)^{1/2}}{2k_BT}\right]}{(\varepsilon^2+A^2)^{1/2}}, \tag{6.2}$$

and similarly for $F(B)$. Subscripts 1 and 2 denote the band number. Gap A opens up on band 1 and gap B opens up on band 2. ε = electron kinetic energy relative to E_F, N_i = DOS of the i^{th} band at the Fermi level, and V_{ij} = the averaged interaction energy resulting from phonon emission and absorption by band *i-j* processes, minus the corresponding shielded Coulomb interaction terms [88]. The presence of interband coupling causes (a) both gaps to open up at the same T_c, (b) one gap to be larger than the BCS gap and the other smaller, and (c) deviations from BCS temperature dependence for each gap. Intraband coupling further modifies slightly the temperature dependence of the gaps.

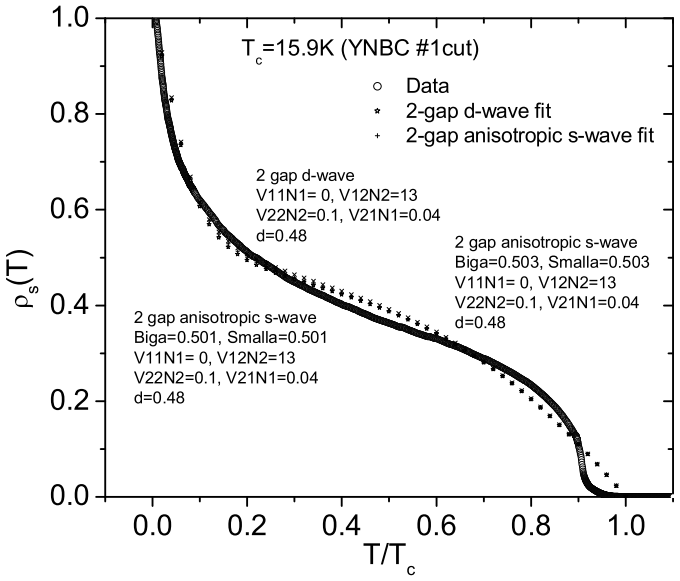

Figure 6.2: Superfluid density ρ_s(T) of YNi_2B_2C. (◯) Data. (×,+,⋆) Calculation using Suhl's multi-gap model. The parameters are listed inside the figure.

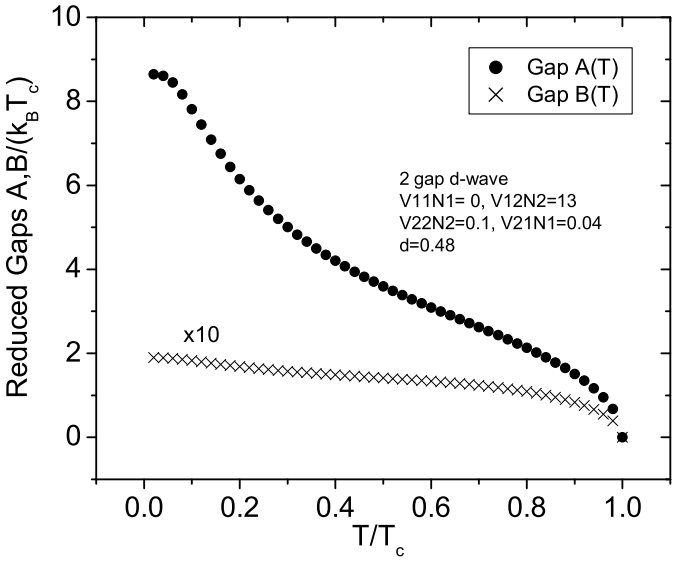

Figure 6.3: Reduced gaps A(T), B(T), in units of k_BT_c, for 2-d-wave-gap model mentioned in the main text, to fit the ρ_s data for YNi_2B_2C.

Fig. 6.2 depicts the superfluid density $\rho_s(T) \equiv \lambda^2(0)/\lambda^2(T)$ of YNi_2B_2C (circles). Notice the unambiguous upturn near 0.1–0.2 T_c. To fit the data, we tried the following gap symmetries: (1) 1-gap isotropic s-wave, (2) 1-gap d-wave, (3) 1-gap anisotropic s-wave (with $\Delta_{max}/\Delta_{min} \approx 10$), (4) 2-gap anisotropic s-wave, and (5) 2-gap d-wave. We fix T_c (15.9 K), using the onset of superconductivity from magnetization data. The parameters we vary are: $V_{11}N_1$, $V_{22}N_2$, $V_{12}N_2$, $V_{21}N_1$, as well as d_1 (the contribution of band 1 to the total superfluid density). We found that the one-gap pictures are inadequate to explain the upturn at 2 K. Turning to the two-gap models, we obtain a moderately good fit if we assume that (1) both gaps are d-wave, and (2) only interband coupling is present, with only 3 parameters required: $V_{12}N_2$=13, $V_{21}N_1$=0.04, and d_1=0.48. We obtain a better fit if we include a small amount of intraband coupling in band 2: $V_{22}N_2$=0.1, as shown in Fig. 6.2. Fig. 6.3 shows the temperature-dependence of the two d-wave gaps A and B according to Suhl's model. If both gaps were anisotropic s-wave gaps with $\Delta_{max}/\Delta_{min} \approx 13$, there would be virtually no difference in temperature dependence. Deviations between the data and fit might result from (1) the intermediate to strong-coupling nature of the electron-phonon interaction in this sample, whereas our model assumes weak-coupling; (2) there may be more than two gaps opening up at T_c due to the complicated Fermi surface. Shulga *et. al.* [88] already used 2 bands to explain the upper critical field data, specifically the positive curvature near T_c. The low-temperature $\Delta\lambda$ downturn is also observed in the magnetic counterpart, $HoNi_2B_2C$ [91]. Thermal conductivity data, which shows a rapid increase in quasiparticle density at very low temperature (70 mK) and field ($\leq H_{c1}$), could alternatively be explained by the presence of a second, smaller gap rather than a very large gap anisotropy, which is unprecedented for an s-wave superconductor [83]. If in our 2-gap model $V_{12} \approx V_{21}$, then $N_2/N_1 \approx 325$, which suggests that band 1 should be the α-band with a smaller DOS. This implies that the *larger* gap (A) opens up on the band with the smaller DOS (α), thus contradicting the results of Terashima *et al.* [89], which showed that the *smaller* gap opens up on the small α-pocket with a small DOS. The Suhl-Mattheiss model, which ascribes the pairing potential

to interband terms, thus causes the larger (smaller) gap to open on the band with the smaller (larger) DOS, contrary to experimental results. We must question, therefore, whether the downturn is intrinsic. Further evidence for an extrinsic effect comes from $\Delta\lambda(T)$ data taken recently on a floating-zone-grown YNi_2B_2C sample. The shape of the curve looks very different from the flux-grown sample above — the downturn of this sample is sharper and larger. When we converted $\Delta\lambda$ to ρ_s, the initial drop on ρ_s is absurdly large (of course we assumed that $\lambda_{0\alpha} = \lambda_{0\beta}$, which is not physical). We shall not bother to show those figures here. A fuller discussion of these low-T downturns is deferred to Section 6.3.

6.2.2 $LuNi_2B_2C$

We use the same method of analysis, i.e. the Suhl two-gap model, to explain the superfluid data for $LuNi_2B_2C$. Fig. 6.4 shows $\Delta\lambda(T)$ over the entire temperature range. Notice the downturn below $\sim$1 K. Fig. 6.5 shows the superfluid density $\rho_s(T)$, with the data in circles and the two-gap fit as a dotted line. As indicated in the figure, the best fit is obtained if one uses a 2-gap model with parameters $V_{12}N_2$=13, $V_{21}N_1$=0.04, $V_{11}N_1$=0.5 and d_1=0.83, with the smaller gap being an anisotropic s-wave gap, and the larger gap a d-wave gap. Fig. 6.6 shows the temperature dependence of the two gaps A and B. As is the case for YNi_2B_2C, the larger gap opens on the small α-pocket, making the fit unrealistic.

Considering the unreasonable values in the 2-band fits, we turn now to an alternative explanation. Two recent theoretical studies by Yuan *et al.* [92] and Maki *et al.* [93] showed that, if the borocarbides, in particular the non-magnetic members, have superconducting gaps with $s+g$ symmetry, a gap in the quasiparticle energy spectrum is found to open even for infinitesimal impurity scattering, giving rise to exponentially activated thermodynamic response functions, such as the specific heat, the spin susceptibility, the superfluid density,

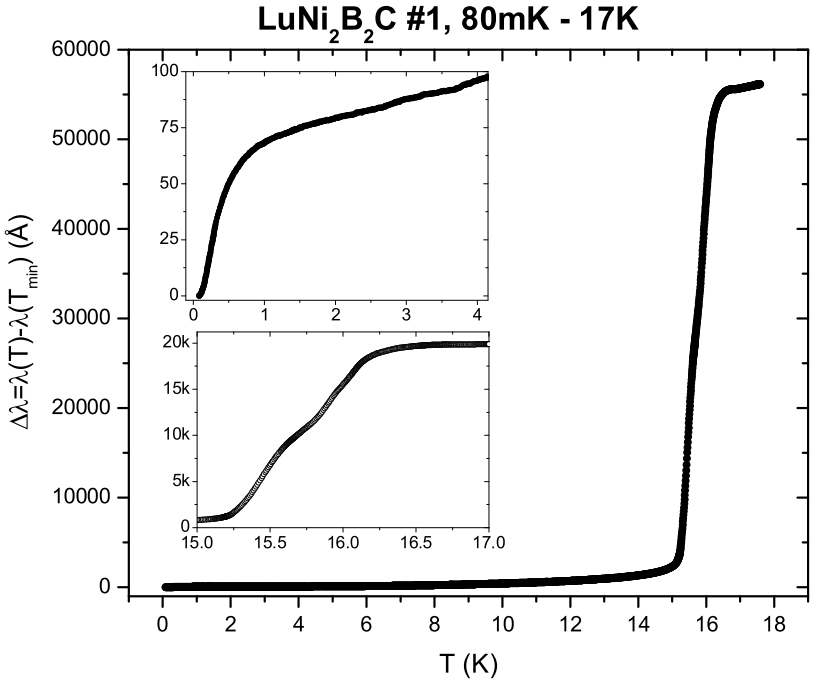

Figure 6.4: $\Delta\lambda(T)$ for $LuNi_2B_2C$. Notice the downturn near 1 K.

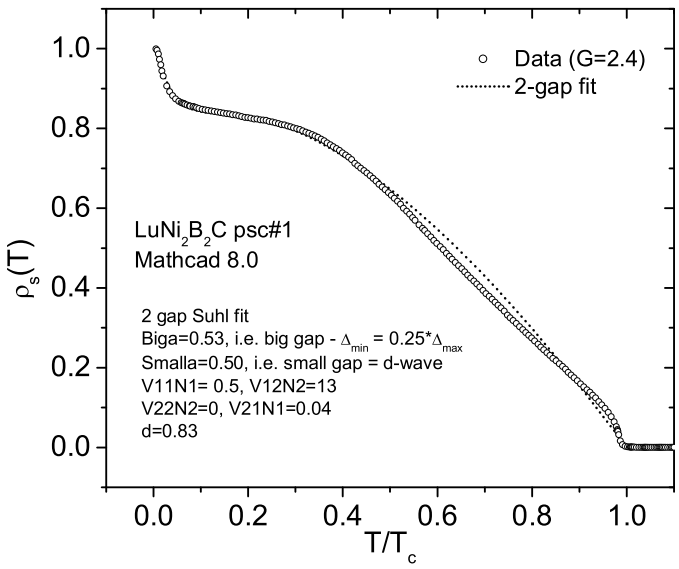

Figure 6.5: Superfluid density $\rho_s(T)$ for $LuNi_2B_2C$. (◯) Data. (Dotted line) Suhl's 2-band best fit, with parameters listed in the figure.

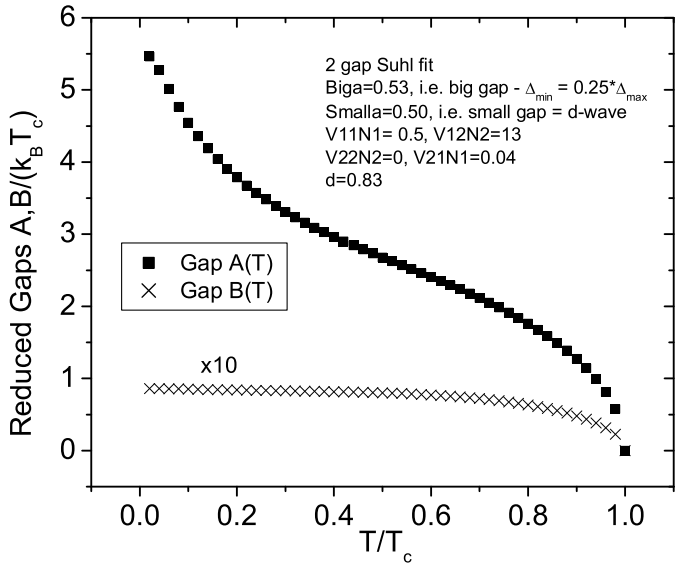

Figure 6.6: Reduced gaps A(T), B(T), in units of $k_B T_c$, for 2-gap model to fit ρ_s data for $LuNi_2B_2C$.

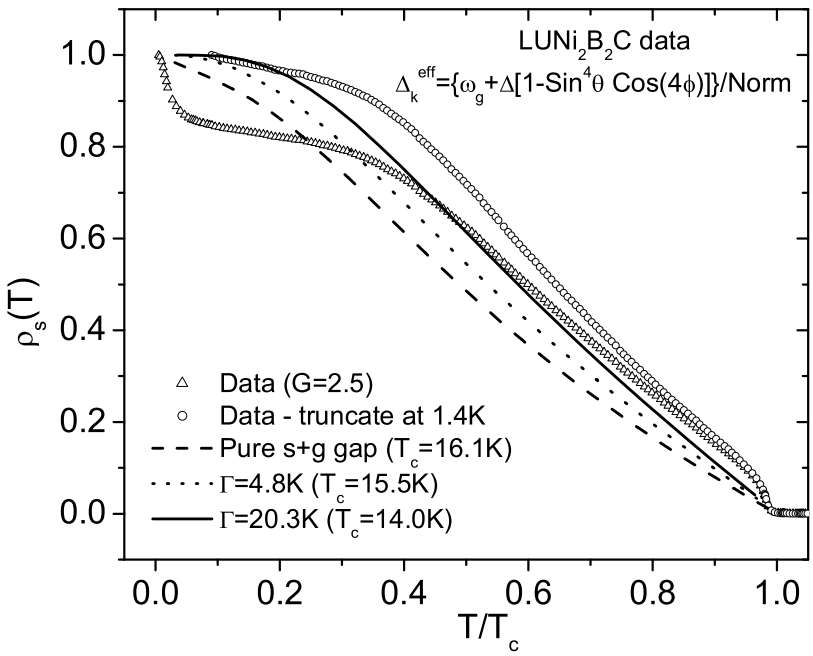

Figure 6.7: Superfluid density ρ_s(T) for different values of impurity scattering rate Γ. (◯) $LuNi_2B_2C$ data, assuming $\rho_s = 0$ at 0.1 K. (△) $LuNi_2B_2C$ data, assuming $\rho_s = 0$ at 1.4 K. Calculated ρ_s for (Dash) $\Gamma = 0$, (Dot) $\Gamma = 4.8$ K, (Solid line) $\Gamma = 20.3$ K.

and the nuclear spin lattice relaxation. In Maki's model, the s+g superconducting gap in the pure limit is given by [93]

$$\Delta_{\mathbf{k}}^{pure}(T) = \frac{\Delta(T)}{2}(1 - \sin^4\theta\cos 4\phi), \tag{6.3}$$

where $\Delta(T)$ is the **k**-independent, T-dependent gap.

The suppression of T_c by impurities follows the Abrikosov-Gorkov-like expression [93]

$$\ln\left(\frac{T_c}{T_{c0}}\right) = 0.169\left[\psi\left(\frac{1}{2}\right) - \psi\left(\frac{1}{2} + \frac{\Gamma}{2\pi T_c}\right)\right], \tag{6.4}$$

where the impurity scattering rate Γ can be calculated. ψ is the digamma function and T_{c0} is the superconducting transition temperature of the purest sample. One then substitutes Γ into the expression for the **k**-*independent* impurity gap ω_g

$$\omega_g(T,\Gamma) = \frac{2\Gamma}{1 + \frac{2\Gamma}{\Delta(T,\Gamma)}}. \tag{6.5}$$

The effective gap $\Delta_{\mathbf{k}}^{eff}$ is then [94]

$$\Delta_{\mathbf{k}}^{eff}(T,\Gamma) = \frac{\Delta(T,\Gamma)}{N}\left(1 - \sin^4\theta\cos 4\phi + \frac{\frac{2\Gamma}{\Delta(T,\Gamma)}}{1 + \frac{2\Gamma}{\Delta(T,\Gamma)}}\right), \tag{6.6}$$

where N is the normalization factor.

We try next to fit Maki's impurity s+g model to $LuNi_2B_2C$. Using T_{c0} = 16.1 K and T_c = 15.5 K from Ref. [85], and $\Delta_0 = 2.1k_BT_c$ [95], we obtain Γ = 4.8 K. We then substitute these values into Eqn. 6.6 and Eqn. 2.53 to calculate the superfluid density. Fig. 6.7 shows the calculated superfluid density for different values of Γ. We see that in the presence of impurities (and hence the impurity gap), there is a *gradual* evolution from linear to exponential at the lowest temperatures. The opening up of an energy gap in an impure sample, therefore, does *not* result in a *sudden* downturn (upturn) in the penetration depth

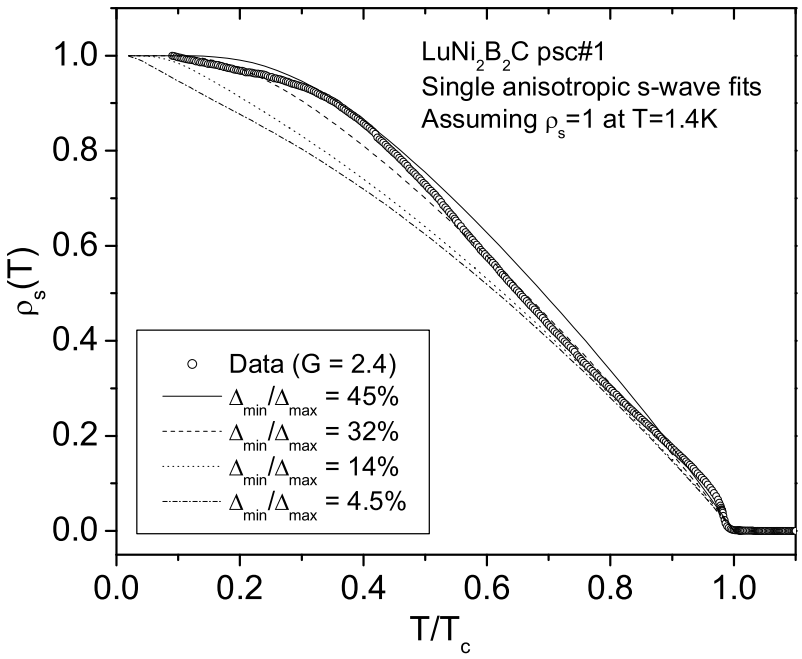

Figure 6.8: Superfluid density $\rho_s(T)$ for $LuNi_2B_2C$, assuming $\rho_s = 0$ at 1.4 K. (◯) Data. Lines = 1-gap anisotropic s-wave calculation for various values of $\Delta_{min}/\Delta_{max}$.

(superfluid density). However, this impurity model can at least qualitatively explain the data of Carrington *et al.*, as described in Paragraph 6 above — the process of annealing presumably removes interstitial vacancies in the sample, thus giving linear-T behavior.

Because the downturn may not be intrinsic, we take $\Delta\lambda = 0$ (and hence $\rho_s = 1$) at 1.4 K, to obtain the superfluid density shown in Fig. 6.8. The circles indicate data, and the lines indicate 1-gap anisotropic s-wave plots for various values of $\Delta_{min}/\Delta_{max}$. It seems that the best fit of the data is when $\Delta_{min}/\Delta_{max} = 0.45$. This does not agree with thermal conductivity data [83], which suggests that the gap minimum Δ_{min} is at least 10 times smaller than the gap maximum, and possibly going to zero at nodes. Fig. 6.7 also compares the "truncated" superfluid density with Maki's impurity model. To have a moderately good fit would require $\Gamma = 20.3$ K, implying $T_c = 14.0$ K. The $\Delta\lambda$ data do not indicate such a low T_c.

6.3 The Mystery of the Second Downturn

The comments in this section apply to all the rare-earth borocarbides that I have measured, namely $RENi_2B_2C$ (RE = Y, Lu, Er, Ho). In all these samples, the penetration depth data revealed an additional downturn near 1 K, for example, in Fig. 6.4 for $LuNi_2B_2C$. Much has been done to determine whether this downturn is extrinsic or intrinsic. Until today I am unsure. I will list down the arguments/observations that suggest both ways.

(1) The samples I have initially measured come from two sources: (a) Pohang University, South Korea (PSC), and (b) Ames Laboratory, Iowa State University. They are flux-grown single crystals, either annealed or non-annealed.

(2) The downturn is seen in all the borocarbide samples I measured. For each material I measured multiple samples from either the same or different batch, with similar results. This suggests that this downturn is intrinsic, and is not a magnetic effect, since it is seen in the non-magnetic samples (YNi_2B_2C and $LuNi_2B_2C$), as well as the magnetic ones ($ErNi_2B_2C$ and $HoNi_2B_2C$). One conjecture is that the low-temperature downturn is due to the opening up of the second superconducting gap in the borocarbides. This is not surprising because in the borocarbides there are at least 4 bands crossing the Fermi energy [96].

(3) Since the samples are flux-grown single crystals, Scanning Electron Microscope (SEM) photographs of the surface reveal regions of high concentration of Ni (Ni:Lu = 9:1), coming from the Ni_2B flux used to grow the single crystals. Dr. David Lawrie, a postdoctoral fellow from Professor Russ Giannetta's group, measured the penetration depth of an Ames $LuNi_2B_2C$ sample down to 0.3 K. He also observed a downturn below about 1.5 K, but of smaller magnitude than the PSC sample I measured. In a small dc field the downturn disappeared. Also, after etching the flux-rich regions from the surface, the downturn disappeared. But the downturn re-appeared when the etched sample was re-annealed. Etching the surface sometimes also revealed new regions of flux that sometimes penetrated through the sample! Dr. Lawrie guessed that the downturn is both extrinsic and intrinsic.

(4) A few months ago I obtained some $ErNi_2B_2C$ and YNi_2B_2C samples, grown by the floating zone method, from National Institute for Materials Science, Tsukuba, Japan. Samples grown using this method should contain far less flux than those grown by the flux method. Also, these samples were annealed after growth, and so the amount of flux should even be less. The penetration depth data on both samples, however, showed a huge downturn, at an even higher temperature! The $ErNi_2B_2C$ signal, for example, did not show the features that one would expect for this material, suggested by other measurements and confirmed by my measurement of the PSC sample. This is caused by the appearance of a very large paramagnetic-like upturn that started at $\sim$4 K that drowns out the fine features one would expect at 6 K and 2.3 K. So it seems that the flux-grown samples are *purer* than the floating-zone ones. Based on this observation, one would think that the downturns in the flux-grown samples are intrinsic, not due to flux, but perhaps related to the various amounts of impurities in the samples, particularly those on the surface. It has been shown that, at least for the magnetic members, the magnetic ordering depends very sensitively on surface composition, on whether the different magnetic states come from the same region of the sample's surface [97].

(5) Recently I took SEM images of the Japanese YNi_2B_2C and $ErNi_2B_2C$ samples, and performed a energy dispersive X-ray (EDX) analysis on the surface. I found an abundance of Yttrium or Erbium *oxide* on the surface. A normalized analysis of Y(Er) and Nickel for the surface yielded a ratio of Y(Er):Ni $\approx$ 9:1! The penetration depth data on these two samples also show a downturn below 1–4 K. So, whether there is an abundance of rare-earth over Ni (floating-zone grown samples), or Ni over rare-earth (flux-grown samples), one essentially sees the same qualitative features in $\Delta\lambda$. This seems to contradict the popular belief that the downturn is due to surface flux. When I performed the same EDX analysis on an exposed portion of the *bulk* of the sample, the Y(Er):Ni ratio gives the correct value of 2:1. Perhaps

the downturn in all these samples, irrespective of growth method, is due to the presence of rare-earth oxide on the surface.

Although all the borocarbides I have studied exhibited downturns below $\sim$ 1 K, the nature of the downturn is different. For the non-magnetic YNi_2B_2C and $LuNi_2B_2C$, there was either a flattening of $\Delta\lambda$ before the onset of the downturn (flux-grown $LuNi_2B_2C$ and floating-zone-grown YNi_2B_2C), or a slight change of curvature all the way to 100 mK (flux-grown YNi_2B_2C). Compare this with the magnetic borocarbides, where one sees an initial *upturn* in $\Delta\lambda$, before the onset of the downturn. Yttrium oxide, at least Y_2O_3, is an extremely stable ceramic. It is not known to be superconducting or even magnetic, but it probably was never studied to 1 K. The other oxides (Er, Ho) are antiferromagnets — that may explain the initial *upturn* in $\Delta\lambda$ (before the onset of the downturn) in these magnetic borocarbides, as will be described in subsequent chapters. The upturn may be where the Neel transition takes place. The Neel temperature of Er_2O_3 is 3.4 K [98].

(6) During the 2003 American Physical Society March Meeting, Dr. Andrew Carrington's group from UK reported penetration data for flux-grown $LuNi_2B_2C$ and YNi_2B_2C down to 1.4 K. They found that the temperature-dependence of λ depends markedly on surface preparation. For a polished surface, an exponential temperature dependence characteristic of an isotropic s-wave superconducting gap is measured. However, after annealing under high vacuum, $\lambda(T)$ exhibits close to a linear, power law behavior suggesting the presence of deep minima in the superconducting gap. To date, however, these results have not been published, suggesting, perhaps, difficulty in reproducing these results consistently.

(7) Upper critical field (H_{c2}) data near T_c of $LuNi_2B_2C$ [99] and YNi_2B_2C [95, 74] show a positive curvature. Palistrant [100] showed that in two-band superconductors the temperature dependence of H_{c2} in the vicinity of T_c has a positive curvature due to the relation $v_{F1} \neq v_{F2}$ (v_{Fn} = velocity of electrons on n-th FS sheet). Contrast this with the one-band case, where the curvature is negative.

(8) Terashima *et al.* [89] performed de Haas-van Alphen (dHvA) experiments on YNi_2B_2C, and found that there is a small superconducting gap opening on a small electron pocket (denoted α) part of the FS, and this gap is much smaller than the gap on other parts of the FS. Since this α surface is very small, enclosing only 0.3% of the first Brillouin zone (BZ), and contributes little to the density of states, it would hardly influence the average SC gap. Their conclusion therefore does not conflict with the results of tunneling spectroscopy, nor the specific-heat measurements, which determine a "DOS-weighted" average superconducting gap over all the pieces of the FS. Due to this very small area of the α surface, we would expect it to contribute negligibly to the total superfluid density. So even if this second superconducting gap does exist, it would be difficult to see it in my penetration depth measurements.

(9) Even if one uses a two-gap model to interpret the data, one might be able to ignore the contribution of the downturn to the total superfluid density. A pre-requisite of ignoring this downturn is that the second gap originates from a different part of the FS, *not* from the presence of impurities. Specifically, for a two-band system, the total superfluid density (not normalized) is the sum of superfluid density from the two bands, i.e.

$$\frac{m^*_{eff}}{\lambda^2(T)} = \frac{m^*_1}{\lambda^2_1(T)} + \frac{m^*_2}{\lambda^2_2(T)}, \tag{6.7}$$

where the subscripts denote bands "1" and "2", m^*_i denotes effective electron mass in the i^{th}-band. m^*_{eff}, which we denote to be the effective mass of the two-band system, will be derived later in this section.

At $T = 0$, Eqn. 6.7 becomes

$$\frac{m^*_{eff}}{\lambda^2(0)} = \frac{m^*_1}{\lambda^2_1(0)} + \frac{m^*_2}{\lambda^2_2(0)}. \tag{6.8}$$

So the *normalized* superfluid density is

$$\begin{aligned}
\frac{\lambda^2(0)}{\lambda^2(T)} &= \frac{\frac{m_1^*}{\lambda_1^2(T)} + \frac{m_2^*}{\lambda_2^2(T)}}{\frac{m_1^*}{\lambda_1^2(0)} + \frac{m_2^*}{\lambda_2^2(0)}} \\
&= \left[\frac{m_1^*}{\frac{m_1^*}{\lambda_1^2(0)} + \frac{m_2^*}{\lambda_2^2(0)}}\right] \frac{1}{\lambda_1^2(T)} + \left[\frac{m_2^*}{\frac{m_1^*}{\lambda_1^2(0)} + \frac{m_2^*}{\lambda_2^2(0)}}\right] \frac{1}{\lambda_2^2(T)} \\
&\equiv \frac{A}{\lambda_1^2(T)} + \frac{B}{\lambda_2^2(T)}. \qquad (6.9)
\end{aligned}$$

Next we express λ, λ_1 and λ_2 as

$$\begin{aligned}
\lambda &= \lambda_0 + \Delta\lambda(T) \\
\lambda_1 &= \lambda_{10} + \Delta\lambda_1(T) \\
\lambda_2 &= \lambda_{20} + \Delta\lambda_2(T), \qquad (6.10)
\end{aligned}$$

where the subscript "0" denotes the value at $T = 0$.

Expanding Eqn. 6.9 to first order in $\Delta\lambda$, and suppressing the T-dependent notation, one then obtains

$$\lambda_0^2 \left(\frac{1}{\lambda_0^2} - \frac{2\Delta\lambda}{\lambda_0^3}\right) = A\left(\frac{1}{\lambda_{10}^2} - \frac{2\Delta\lambda_1}{\lambda_{10}^3}\right) + B\left(\frac{1}{\lambda_{20}^2} - \frac{2\Delta\lambda_2}{\lambda_{20}^3}\right). \qquad (6.11)$$

But from Eqn. 6.9

$$1 = \frac{\lambda_0^2}{\lambda_0^2} = \frac{A}{\lambda_{10}^2} + \frac{B}{\lambda_{20}^2}. \qquad (6.12)$$

Hence Eqn. 6.11 becomes

$$\Delta\lambda = \left(\frac{\lambda_0 A}{\lambda_{10}^3}\right)\Delta\lambda_1 + \left(\frac{\lambda_0 B}{\lambda_{20}^3}\right)\Delta\lambda_2. \qquad (6.13)$$

One then sees, from Eqn. 6.13, that the contribution of $\Delta\lambda_1$ and $\Delta\lambda_2$ to $\Delta\lambda$ depends on the prefactors $(\lambda_0 A/\lambda_{10}^3)$ and $(\lambda_0 B/\lambda_{20}^3)$. For example, if $\lambda_0 A/\lambda_{10}^3 \ll \lambda_0 B/\lambda_{20}^3$, then a large

$\Delta\lambda_1$ would still not contribute much to $\Delta\lambda$. Hence the relative contribution of $\Delta\lambda_1$ and $\Delta\lambda_2$ to $\Delta\lambda$ depends on the quantities m^*_{eff}, m^*_1, m^*_2, λ_{10}, λ_{20} and λ_0. λ_{10} and λ_{20} are purely FS-quantities, i.e. they only depend on FS parameters of each of the two Fermi sheets. Specifically, for the i-th Fermi sheet, assuming spherical [46],

$$\lambda_{i0} \equiv \lambda_i(0) = \left(\frac{3c^2}{8\pi e^2 v_F^2 N(E_F)} \right)^{1/2}, \tag{6.14}$$

where v_F is the Fermi velocity and N(E_F) is the DOS at the Fermi level.

But

$$N(E_F) = \frac{m_i^{*2} v_F}{\hbar^3 \pi^2}, \tag{6.15}$$

where m_i^* is the effective mass of the electrons on the i-th Fermi sheet.

Hence

$$\lambda_i(0) = \left(\frac{3c^2\pi\hbar^3}{8e^2} \right)^{1/2} \left(\frac{1}{m^* v_F^{3/2}} \right). \tag{6.16}$$

m_1^* and m_2^* can be experimentally determined, for example, from dHvA measurements. We can estimate m^*_{eff} by considering two limits: (1) m^*_{eff} ($m_1^* = m_2^*$) $= m_1^*$, (2) m^*_{eff} ($m_1^* \ll m_2^*$) $\rightarrow m_2^*$. A suitable empirical expression for m^*_{eff} that fulfills the above two conditions is

$$m^*_{eff} = \frac{m_1^*}{m_1^* + m_2^*} m_1^* + \frac{m_2^*}{m_1^* + m_2^*} m_2^*. \tag{6.17}$$

From the values of m^*_{eff}, m_1^*, m_2^*, λ_{10} and λ_{20}, we can calculate λ_0 from Eqn. 6.8. Finally, we substitute all these values into Eqn. 6.13 to get the contribution of $\Delta\lambda_1$ and $\Delta\lambda_2$ to $\Delta\lambda$.

Take YNi_2B_2C, for example. dHvA measurements [87] reveal that the two largest FS sheets are the β-sheet ($m_\beta^* = 1.50$ m_0, $v_{F\beta} = 3.75 \times 10^5$ m/s, 22.5% of first BZ), and the α-sheet ($m_\alpha^* = 0.55$ m_0, $v_{F\alpha} = 1.93 \times 10^5$ m/s, 0.84% of first BZ). m_0 is the free-electron mass. From Eqn. 6.16 we get $\lambda_{\beta 0} = 740$ Å and $\lambda_{\alpha 0} = 5470$ Å. Eqn. 6.17 gives $m^*_{eff} = 1.25\, m_0$.

Finally, putting all these numbers into Eqn. 6.13 gives, for YNi_2B_2C (band 1 = α-band, band 2 = β-band)

$$\begin{aligned}\Delta\lambda(T) &= 0.0007\Delta\lambda_\alpha(T) + 0.79\Delta\lambda_\beta(T) \\ &\equiv A'\Delta\lambda_\alpha(T) + B'\Delta\lambda_\beta(T) \\ &\equiv \Delta\lambda'_\alpha(T) + \Delta\lambda'_\beta(T) \quad (YNi_2B_2C). \end{aligned} \tag{6.18}$$

We see thus that the total change in penetration depth $\Delta\lambda(T)$ is a *weighted* sum of change in penetration depth from the individual bands. Since $LuNi_2B_2C$ has similar band structure, we can take Eqn. 6.18 to be applicable to $LuNi_2B_2C$. Note that the experimentally-obtained value of the zero-temperature penetration depth for YNi_2B_2C and $LuNi_2B_2C$ are 1207 Å and 759 Å respectively [95]. If we take these values as that of the larger gap arising from the β-band, i.e. $\lambda_\beta(0)$, then for YNi_2B_2C, A' = 0.0003 and B' = 0.76, whereas for $LuNi_2B_2C$, A' = 0.0008 and B' = 0.79. This does not change our conclusion: the contribution of $\Delta\lambda_1$ to the total penetration depth $\Delta\lambda$ is negligible, i.e. we will not be able to observe any appreciable change in $\Delta\lambda$ due to the second, smaller gap from the α-band.

Our data for $LuNi_2B_2C$ reveal a downturn below 1 K of about 50 Å. If we attribute all of this downturn to $\Delta\lambda'_\alpha$, then $\Delta\lambda_\alpha \approx 6$ μm — an unreasonably large number. Any reasonable value for $\Delta\lambda_\alpha$ will give a negligible contribution to $\Delta\lambda$.

The only scenario where the downturn needs to be considered is if $\lambda(0)$ of the smaller FS-sheet is the same as that of the larger sheet. Then the contribution of the smaller sheet to ρ_s is significant — too significant, in fact, to be physically reasonable. Later in this chapter, for illustrative purposes, I will analyze the data for YNi_2B_2C and $LuNi_2B_2C$ using the two-band picture, assuming $\lambda_\alpha(0) = \lambda_\beta(0)$, and show that for the model to fit the data, the contribution from the α-band to the total superfluid density is too large compared to its area in the first BZ. Therefore, whether the downturn is extrinsic or intrinsic, it is safe to ignore it, as it contributes to the total superfluid density (ρ_s) negligibly. The consequence

of this is that we will not be able to determine the low-temperature behavior of $\Delta\lambda$, and hence, the nature of the low-energy excitations and the superconducting gap symmetry of this material.

6.4 Conclusion and Future Work

In conclusion, we report measurements of the magnetic penetration depth $\Delta\lambda(T)$ in single crystals of YNi_2B_2C and $LuNi_2B_2C$ down to $\sim$0.1 K using a tunnel-diode based, self-inductive technique at 28 MHz. Besides the usual drop of $\Delta\lambda(T)$ at T_c, a second drop around 1 K was observed. The magnitude of this drop is $\sim$1% of the total signal. We analyzed the data using a two-gap model first proposed by Suhl *et al.* [90], and obtained a good fit. However, (1) the fit assumes $\lambda_{0\alpha} = \lambda_{0\beta}$, which is not valid, (2) the larger gap opens up on the small α-pocket, which contradicts dHvA data [89] and (3) even if there is a second smaller gap opening up on the α-pocket, the fact that $\lambda_{0\alpha} = 7.4\lambda_{0\beta}$ will cause the second gap to be unobservable in the penetration depth data. We applied Maki's impurity-gap model [93] to $LuNi_2B_2C$, and found that it gives a good fit to data only down to 6 K, and so too, does not explain the 1 K-downturn. We therefore hypothesize that the downturn is not intrinsic to the bulk of the sample. In subsequent chapters, the same downturn is seen in $ErNi_2B_2C$ and $HoNi_2B_2C$, and we shall ignore them in our analysis.

As described in Section 6.3 Paragraph 5, the downturn may be due to the presence of the surface oxide layer. Our future work on the borocarbides will be to run the same samples *after* etching away this oxide layer (either chemically or mechanically), then quickly mount the sample and evacuate the system. We run the risk of creating dislocations on the surface, but this may be a lesser of two evils. I will also explore the possibility, from Ref. [101], of using aqua regia to etch away the surface oxide layer.

For this project I thank Professor S.-I. Lee for providing the YNi_2B_2C and $LuNi_2B_2C$ flux-grown samples, and Professor H. Takeya for the YNi_2B_2C floating-zone-grown samples. I also thank Dr. D. Lawrie for stimulating discussions.

Chapter 7

$ErNi_2B_2C$: Effect of magnetic order on superfluid response

7.1 Introduction

The magnetic members of the rare-earth (RE) nickel borocarbide family, $RENi_2B_2C$ (RE = Ho, Er, Dy, etc) have attracted much interest due to the interplay between magnetism and superconductivity. $ErNi_2B_2C$, in particular, is a good candidate for study: superconductivity starts at $T_c \approx 11$ K, before antiferromagnetic (AF) order sets in at $T_N \approx 6$ K [103]. In the AF state the Er spins are directed along the b-axis, forming a transversely polarized, incommensurate spin-density-wave (SDW) state, with modulation vector modulation vector $\delta = 0.553a^*$ ($a^* = 2\pi/a$) [104], before squaring up at lower temperatures [102]. Below T_{WFM} = 2.3 K a net magnetization appears, superposed on a modulation with a periodicity of $20a^*$, confirming the microscopic existence of spontaneous weak ferromagnetism (WFM) with superconductivity [102, 105]. The SDW and WFM states are illustrated in Fig. 7.1.

The fact that $T_N < T_c$ enables us to study the influence of magnetism on superconductivity. In particular, in this paper we study the pair-breaking effects of the various magnetic orders on the superfluid response of this material. There have been various previous penetration depth measurements on $ErNi_2B_2C$. Jacobs *et al.* [80] measured the microwave surface impedance of single-crystal $ErNi_2B_2C$ from T_c down to 4 K, but did not see the AF transition at 6 K (Fig. 7.2). They concluded that the AF transition is not accompanied by

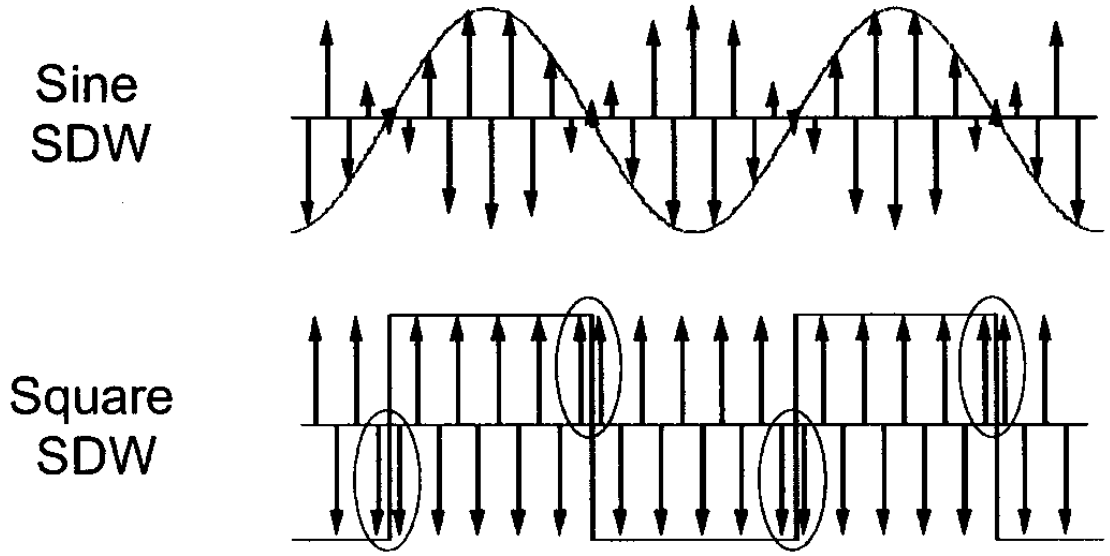

Figure 7.1: Schematic of the spin density wave for T just below T_N, and the (undistorted) wave when it squares up below T_{WFM}. Taken from Ref. [102].

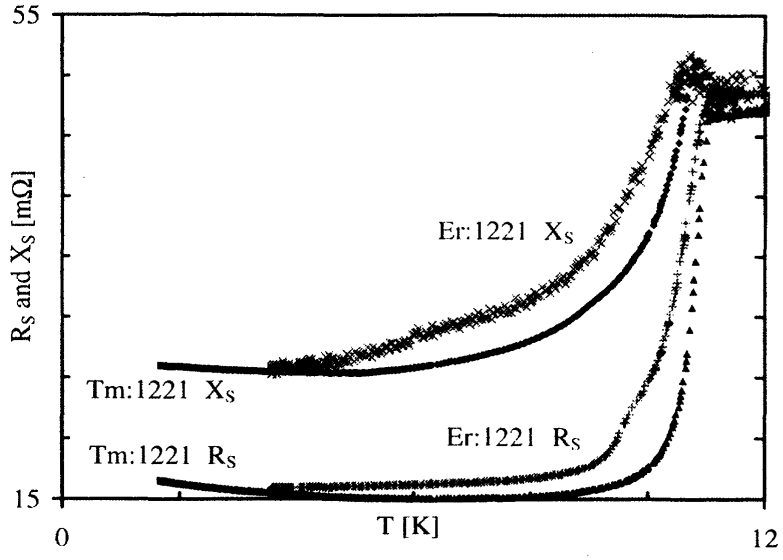

Figure 7.2: Surface impedance data for $ErNi_2B_2C$ single crystal. Taken from Ref. [80].

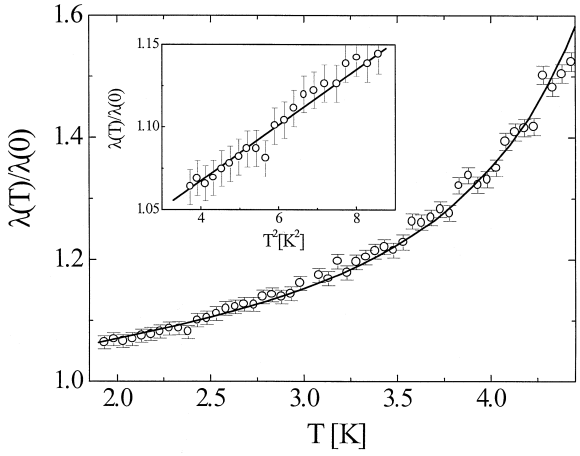

Figure 7.3: Normalized penetration depth $\lambda(T)/\lambda(0)$ for a $ErNi_2B_2C$ film for $T < T_c/2$. The solid line represents theoretical expression from a theory (not described in this chapter.) Inset = Data at the lowest temperatures plotted as a function of T^2 shows a linear slope. Taken from Ref. [106].

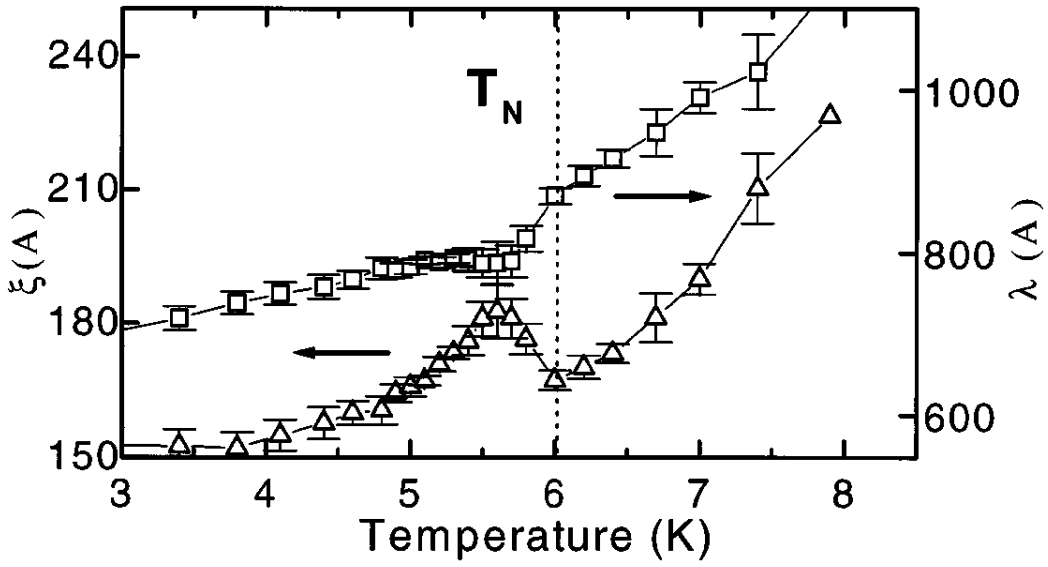

Figure 7.4: Temperature dependence of λ, the superconducting penetration depth ($\square$), and ξ, the superconducting coherence length ($\triangle$), as measured using the flux line form factor in a SANS experiment. Both quantities show distinct features near T_N. Taken from Ref. [107].

pair-breaking in zero field. Andreone *et al.* measured the microwave properties of $ErNi_2B_2C$ thin films — microwave surface resistance down to 2 K [108], and the change in penetration depth from 2–5 K [106] (Fig. 7.3). They too, did not see any feature at T_N, and attributed it to the smearing of the susceptibility $\chi(T)$. Small-angle neutron measurements (SANS) ware performed by Gammel *et al.* [107] on single-crystal $ErNi_2B_2C$ down to 4 K (Fig. 7.4). They observed a decrease of λ below T_N, but could not account for it quantitatively. In our paper we present high-precision measurements of the in-plane magnetic penetration depth of single-crystal $ErNi_2B_2C$ down to 0.1 K. We see features at T_N and T_{WFM}, and seek to ascribe these to the pair-breaking effects of AF order at $T_N = 6$ K and the weak ferromagnetic ordering at $T_{WFM} = 2.3$ K. In addition we also observe a small peak near 1.1 K. We attribute that to a second weak ferromagnetic component. The superfluid density graph indicates that these three magnetic orderings coexist with superconductivity, i.e. they do not destroy superconductivity in this material. The two WFM peaks are the first observations of its kind in penetration depth measurements.

7.2 Theory of Antiferromagnetic Superconductors

Various theories of antiferromagnetic superconductors have been proposed [109, 110, 111, 112, 113, 114, 115]. We shall follow that of Chi and Nagi [115], which is an extension of the mean-field model by Nass and Levin [113, 114] to the regime where the superconducting gap Δ is finite, and it includes the effects of spin-fluctuations, molecular field and impurities. In the Chi-Nagi-Nass-Levin (CNNL) model, which applies specifically to superconductors with $T_N < T_c$, two temperature regimes are separately considered. First, in the paramagnetic regime ($T_N < T < T_c$), the depression of T_c with respect to the non-magnetic counterparts, $LuNi_2B_2C$ or YNi_2B_2C, is due to the exchange scattering of the conduction electrons from the spins of the RE Er ions. Assuming that the exchange interaction is weak, this paramagnetic phase of $ErNi_2B_2C$ can be accounted for by the Abrikosov-Gorkov (AG) pair-breaking

theory [116]. Second, in the AF phase ($T < T_N$), the effect of pair-breaking depends on the competition [117] between the temperature-dependent AF molecular field (with parameter $\mathrm{H}_Q(T)$) and spin-fluctuation scattering of the conduction electrons, the latter by both magnetic RE ions (parameter $1/\tau_2^{eff}$) and non-magnetic impurities (parameter $1/\tau_1$). The molecular field opens AF gaps on parts of the Fermi surface (FS), hence destroying the superconducting gap in those areas. The non-magnetic impurities do not affect the BCS state for an s-wave superconductor [118], but weaken the effect of the AF field by destroying the pairing state for charge density wave or spin density wave [119]. Thus non-magnetic impurities promote the recovery of superconductivity in the material. Moreover, the effect of the molecular field and spin fluctuations are governed by a sum rule [117], and the competition between them determines whether the AF phase gives increased or decreased pair-breaking below T_N. The total electronic effective magnetic scattering rate, $1/\tau_2^{eff}$, is temperature-dependent and decreases with decreasing temperature (as the magnetic moments become more and more frozen). The assumptions of the CNNL model are: (1) the effect of inelastic scattering, which is relevant only for $T \ll T_N$, can be ignored; (2) BCS s-wave pairing and (3) a one-dimensional (1-D) electron band that satisfies the nesting condition $\epsilon_k = -\epsilon_{k+Q}$.

The following equations of the CNNL model were used [115]. The temperature-dependence of the superconducting gap is determined from

$$\text{(AG equation)} \qquad \ln\left(\frac{T_c}{T_{c0}}\right) = \psi\left(\frac{1}{2}\right) - \psi\left(\frac{1}{2} + \frac{1}{2\pi T_c \tau_2^{eff}}\right), \tag{7.1}$$

$$\text{(Renormalized frequency)} \qquad \widetilde{\omega}_{n\pm} = \omega_n + Y_{\mp}\frac{\widetilde{\omega}_{n+}}{2\lambda_+} + Y_{\pm}\frac{\widetilde{\omega}_{n-}}{2\lambda_-}, \tag{7.2}$$

$$\text{(Renormalized gap)} \qquad \widetilde{\Delta}_{n\pm} = \Delta \pm H_Q(T) + X_{\mp}\frac{\widetilde{\Delta}_{n+}}{2\lambda_+} + X_{\pm}\frac{\widetilde{\Delta}_{n-}}{2\lambda_-}, \tag{7.3}$$

$$\text{(Gap equation)} \qquad \ln\frac{T}{T_{c0}} = \pi T \sum \left\{ \frac{1}{\Delta}\left[\frac{1}{(U_{n+}^2+1)^{1/2}} + \frac{(sgn)(U_{n-})}{(U_{n-}^2+1)^{1/2}} \right] - \frac{2}{\omega_n} \right\}, \quad (7.4)$$

where T_{c0} is the transition of the non-magnetic member of the borocarbide family $LuNi_2B_2C$ or YNi_2B_2C, ψ is the digamma function, $X_\pm$ and $Y_\pm$ are linear combinations of the magnetic $(1/\tau_2^{eff})$, non-magnetic $(1/\tau_1)$ and spin-orbit $(1/\tau_{so})$, scattering rates

$$Y_\pm = \frac{1}{2}\left(\frac{1}{\tau_1} + \frac{1}{\tau_2^{eff}} + \frac{1}{\tau_{so}} \right) \pm \frac{1}{2}\left(\frac{1}{\tau_1} + \frac{1}{3\tau_2^{eff}} + \frac{1}{3\tau_{so}} \right), \quad (7.5)$$

$$X_\pm = \frac{1}{2}\left(\frac{1}{\tau_1} - \frac{1}{\tau_2^{eff}} + \frac{1}{\tau_{so}} \right) \pm \frac{1}{2}\left(\frac{1}{\tau_1} + \frac{1}{3\tau_2^{eff}} - \frac{1}{3\tau_{so}} \right). \quad (7.6)$$

$\lambda_\pm = [\widetilde{\omega}_{n\pm}^2 + \widetilde{\Delta}_{n\pm}^2]^{1/2}$; $U_{n\pm} = \widetilde{\omega}_{n\pm}/\widetilde{\Delta}_{n\pm}$; $\omega_n = \pi\, T(2\mathrm{n}{+}1)$ is the Matsubara frequency. In the paramagnetic phase $\widetilde{\omega}_{n\pm} = \widetilde{\omega}_n$, $\widetilde{\Delta}_{n\pm} = \widetilde{\Delta}_n$ and so $U_n = \widetilde{\omega}_n/\widetilde{\Delta}_n$.

The temperature-dependence of the superfluid density ρ_s is given by

$$\rho_s(T) \equiv \left[\frac{\lambda^2(0)}{\lambda^2(T)} \right]^2 = \left[\pi T \sum_{n\geq 0} A(\omega_n) \right], \quad (7.7)$$

where

$$A(\omega_n) = \frac{\widetilde{\Delta}_{n+}^2 - \widetilde{\omega}_{n+}^2}{4\varepsilon_1^3} + \frac{\widetilde{\Delta}_{n-}^2 - \widetilde{\omega}_{n-}^2}{4\varepsilon_2^3} + \frac{1}{4\varepsilon_1} + \frac{1}{4\varepsilon_2} + \frac{1}{\varepsilon_1+\varepsilon_2} + \frac{\widetilde{\Delta}_{n+}\widetilde{\Delta}_{n-} - \widetilde{\omega}_{n+}\widetilde{\omega}_{n-}}{\varepsilon_1\varepsilon_2(\varepsilon_1+\varepsilon_2)}, \quad (7.8)$$

$$\varepsilon_1 = \mid (\widetilde{\omega}_{n+}^2 + \widetilde{\Delta}_{n+}^2)^{1/2} \mid, \varepsilon_2 = \mid (\widetilde{\omega}_{n-}^2 + \widetilde{\Delta}_{n-}^2)^{1/2} \mid . \quad (7.9)$$

In the paramagnetic phase ($T_N < T < T_c$), ρ_s is given by (P: paramagnetic)

$$\rho_s^P(T) = \left[2\pi T \sum_{n\geq 0} \frac{1}{\varepsilon(1+U_n^2)} \right], \tag{7.10}$$

where $\varepsilon = \mid (\widetilde{\omega}_n^2 + \widetilde{\Delta}_n^2)^{1/2} \mid$.

We turn next to the parameters of the model. The effective magnetic scattering rate $(1/\tau_2^{eff})$ from RE ions $(1/\tau_2^R)$ and magnetic impurities $(1/\tau_2^i)$ is given by

$$\frac{1}{\tau_2^{eff}} = \begin{cases} \frac{1}{\tau_2^i} + \frac{1}{\tau_2^R} & (T > T_N) \\ \frac{1}{\tau_2^i} + \frac{1}{\tau_2^R}(1 - F^2(T)) & (T \leq T_N) \end{cases}, \tag{7.11}$$

$$\text{where} \qquad \frac{1}{\tau_2^R} = 2\pi n_R N(0) J(J+1)(g_J - 1)^2 I^2. \tag{7.12}$$

The AF molecular field is given by

$$H_Q(T) = H_Q(0) F(T), \tag{7.13}$$

$$\text{where} \qquad H_Q(0) = n_R I \mid g_J - 1 \mid \sqrt{J(J+1)}. \tag{7.14}$$

n_R is the concentration of RE ions, I is the exchange interaction constant, g_J is the Landé factor, and J is the total angular momentum of the RE ion. The function *F(T)* can be approximated by the empirical relation

$$F(T) = 1 - \left(\frac{T}{T_N} \right)^{\nu}, \tag{7.15}$$

where ν is a parameter obtained by fitting *F(T)* to sublattice magnetization data.

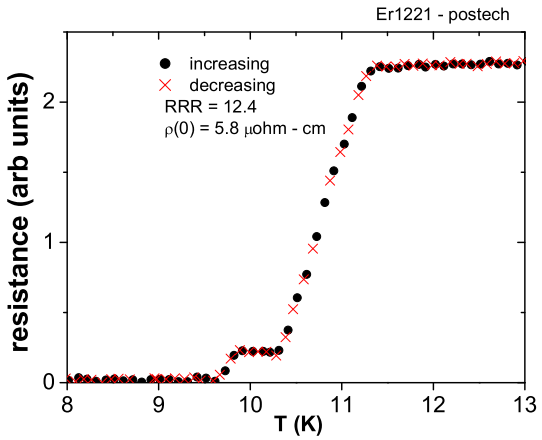

Figure 7.5: Resistivity from 0.1 K to 12 K. Data taken by T. Park.

The values of the renormalized frequency $\widetilde{\omega}_n$ and gap $\widetilde{\Delta}_n$ are determined self-consistently. For a fixed temperature T and Matsubara index n, one determines $\widetilde{\omega}_n$ and $\widetilde{\Delta}_n$ from Equations 7.2 and 7.3 such that they also satisfy Eqn. 7.4. After computing the $\widetilde{\omega}'_n$s and $\widetilde{\Delta}'_n$s for a fixed T, one then substitutes these values into Eqn. 7.7 or 7.10 to obtain the superfluid density ρ_s at that temperature T.

7.3 Data and Analysis

Details of sample growth and characterization are described in Refs. [103] and [120]. The superconducting transitions of our sample were measured by low-field ($H = 5$ G) magnetization, zero-field resistivity and zero-field specific-heat measurements. From magnetization data, the onset of superconducting diamagnetism appears at $T = 11.0$ K and 90% of the full diamagnetic magnetization is reached at $T = 9.6$ K. Resistivity data (Fig. 7.5) show a superconducting onset at a higher temperature of 11.3 K, a small shoulder at 10 K, and zero resistivity at 9.6 K. The mid-point of the specific-heat jump yields a T_c of 10.1 K [121]. A comparison of the three measurements show that bulk superconductivity occurs at $T_c \approx 10$ K, whereas the initial decrease of resistivity at ~ 11 K may be due to some sort of filamentary superconductivity.

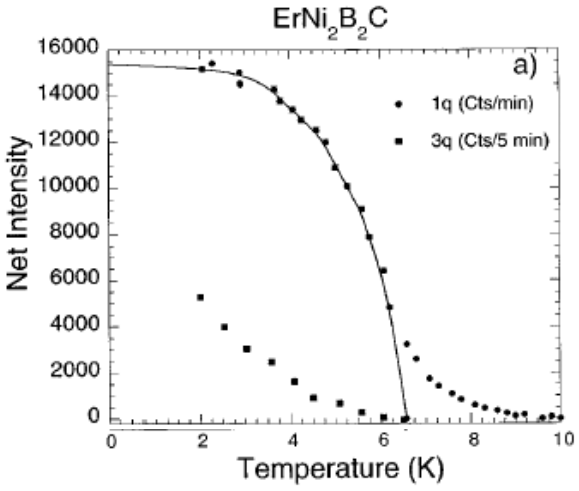

Figure 7.6: Intensity of the first and third-order satellite peaks for the spin-density wave in $ErNi_2B_2C$. Taken from Ref. [97].

The parameters of this model are determined as follows. We denote Δ_0 and $\Delta(0)$ to be the zero-temperature superconducting gap amplitude of YNi_2B_2C and $ErNi_2B_2C$, respectively. Tunneling measurements yield $\Delta_0 = 1.83T_{c0}$ [122]. From the experimental values of T_c (10.1 K for $ErNi_2B_2C$) and T_{c0} (15.5 K for YNi_2B_2C), Equation 7.1 gives $1/\tau_2^{eff}\Delta_0 = 0.227$. Taking $1/\tau_2^i = 0$, Eqn. 7.11 gives $1/\tau_2^R\Delta_0 = 0.227$. The molecular field $H_Q(0)$ is obtained as follows. For $ErNi_2B_2C$, using the values $n_R = 1/6$, $J = 7.5$, $g_J = 1.2$, $N(0) = 0.36$ states/eV-atom-spin [123], we obtain $I = 0.024$ eV from Eqn. 7.12 which is comparable with the experimental value of 0.031 eV [124]. This justifies our assuming $1/\tau_2^i = 0$, as any finite τ_2^i would make I even smaller than the experimental value. Eqn. 7.14 then gives $H_Q(0)/\Delta_0 = 2.6$. From the temperature-dependence of the magnetic Bragg peak intensity below T_N [97, 102] (Fig. 7.6) we obtain $\nu = 4.8$ in Eqn. 7.15. The only remaining free parameter of the theory is $1/\tau$, the non-magnetic scattering rate.

To see the pairbreaking effects of the various magnetic orders we need to convert $\Delta\lambda(T)$ to $\rho_s(T)$, the superfluid density. To determine $\rho_s(T)$ we need the value of $\lambda(0)$, which has

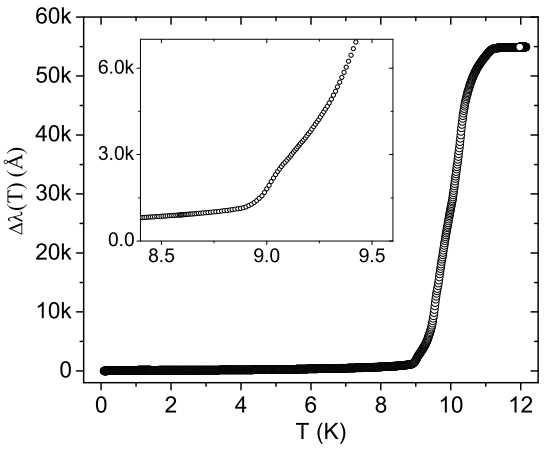

Figure 7.7: $\Delta\lambda(T)$ from 0.1 K to 12 K.

been reported over a range from 700 Å [107] to 1150 Å [103]. We take $\lambda(0)$ to be the parameter in our model, keeping in mind that it has to be in the vicinity of the above two values.

Figures 7.7, 7.8 and 7.9 show the temperature-dependence of the in-plane penetration depth $\Delta\lambda(T)$. We saw a small shoulder at around 9.1 K, which Jacobs *et al.* also saw in their surface reactance data near 9.5 K [80]. We also see the following features: (1) a slight dip in $\Delta\lambda$(T) at $T_N = 6.0$ K, (2) a peak in $\Delta\lambda$(T) at $T_{WFM} = 2.3$ K, and (3) another maximum at 1.1 K. The small dip at T_N has not been seen in previous microwave measurements of either thin-film [108] or single-crystal $ErNi_2B_2C$ [80], but has been observed in SANS data [107]. For dirty AF superconductors, the penetration depth is expected to decrease below T_N by both the susceptibility (χ) and mean free path (l) as $\lambda \sim \lambda'_L/\sqrt{1+4\pi\chi}$, where $\lambda'_L \approx \lambda_L(1+\xi_0/l)$ [125]. Neither effect, however, explains our data: First, using the mean-field expression for χ, in order to reproduce the experimental dip, the peak in χ at T_c has to be at least an order of magnitude larger than that suggested by magnetization measurements [103]. Second, from our resistivity data we obtained $H_{c2}(T)$, and hence we calculated $\xi_0(T)$, *l(T)*, and lastly, λ'_L. Our values of λ'_L also are unable to explain the magnitude of the drop of λ below T_N. Our conclusions are thus similar to Gammel *et al.* for their SANS data [107].

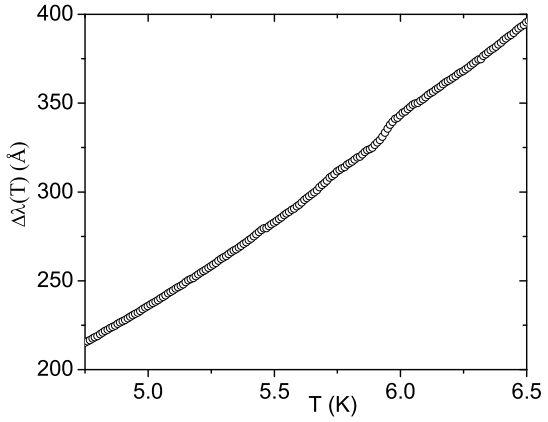

Figure 7.8: $\Delta\lambda(T)$ near the AF transition at 6 K.

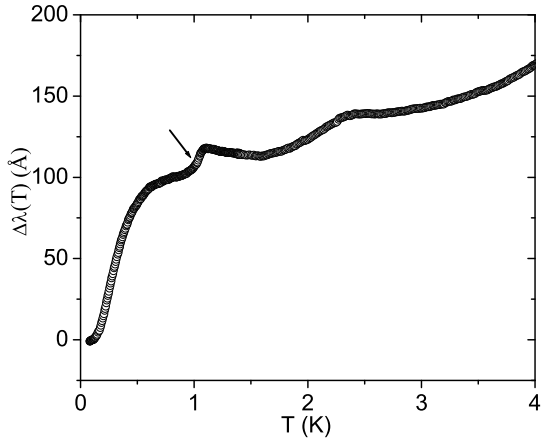

Figure 7.9: $\Delta\lambda(T)$ near the WFM transition at 2.3 K. The arrow indicates the temperature (1 K) where ρ_s is defined to be zero, i.e. the downturn below 1 K is ignored.

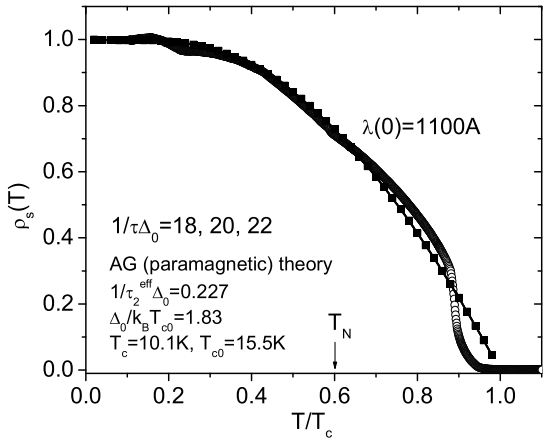

Figure 7.10: $\rho_s(T)$ from 0.1 K to T_c. (◯) data. Solid squares = Paramagnetic fitting curve. The arrow denotes Néel temperature at 6 K.

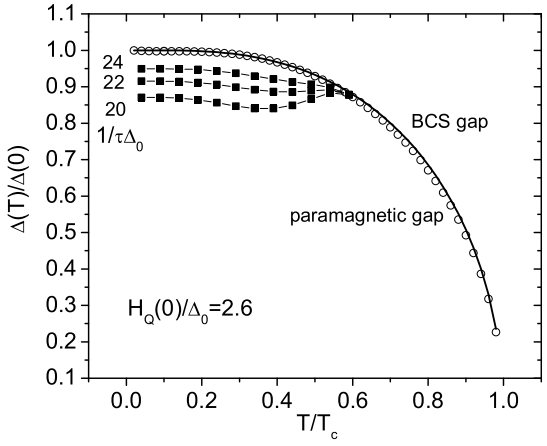

Figure 7.11: Chi-Nagi model calculation for the superconducting gap Δ. Solid line = BCS temperature-dependence. (◯) Paramagnetic gap. Solid squares = Incorporating AF phase below T_N, for different values of $1/\tau\Delta_0$.

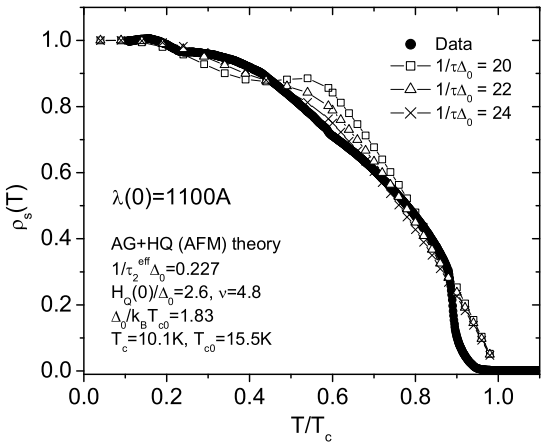

Figure 7.12: $\rho_s(T)$ from 0.1 K to T_c. Solid circles = data. Open squares (triangles, crosses) = AF-phase fitting curves for $1/\tau\Delta_0 = 20$ (22, 24).

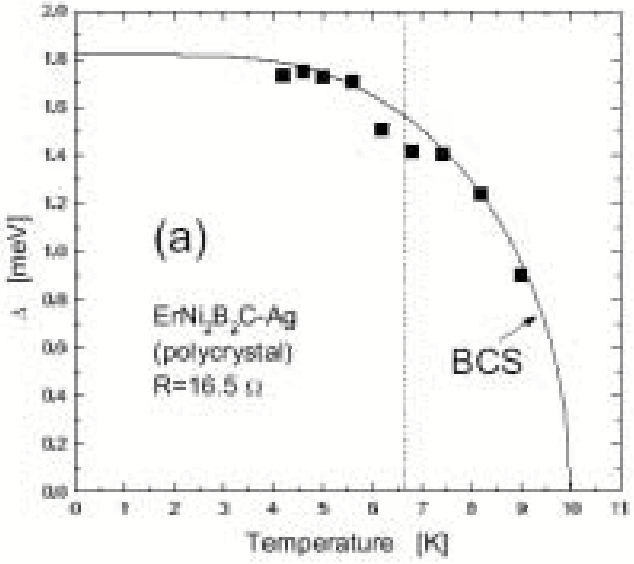

Figure 7.13: Solid squares = Superconducting gap obtained from tunneling measurements. Solid line = BCS calculation. Taken from Ref. [126].

As described in Section 6.3 we neglect the downturn below 1 K when we convert to superfluid density ρ_s, i.e. we assume ρ_s (T=1 K) = 1. Converting to ρ_s in Fig. 7.10, we see that AF order at T_N has negligible effect on superconductivity — ρ_s increases only marginally. The best fit to Eqn. 7.10 (solid squares) is obtained when $\lambda(0) = 1100$ Å; we assume paramagnetism from $T = 0$ to T_c, neglecting AF order, with parameter $1/\tau\Delta_0 = 18$. The paramagnetic curve is almost unchanged if one uses $1/\tau\Delta_0 = 20$ or 22. We see that the paramagnetic curve fits well with the experimental data, even without taking AF order into account. We suggest two possible explanations for this: First, there is near-complete cancellation between the effects of the molecular field and spin-fluctuation scattering, such that there is negligible change in pair-breaking at T_N.

Fig. 7.11 shows the calculated superconducting gap amplitude $\Delta(T)$ for various values of $1/\tau\Delta_0$, as well as the paramagnetic curve. The normalized paramagnetic gap (open circles) agrees excellently with the BCS gap (solid line). Tunneling measurements also show that $\Delta(T)$ follows the BCS curve above T_N [126] (Fig. 7.13). Next, as shown in Fig. 7.11, in the AF phase, as $1/\tau\Delta_0$ is increased, superconductivity is gradually recovered, as evidenced by the increase of $\Delta(T)$ (see the square curves in Fig. 7.12). When $1/\tau\Delta_0 = 24$, Δ is only slightly depressed below the BCS value, in agreement with tunneling data [126, 101]. This value of $1/\tau\Delta_0$ corresponds to a mean free path (mfp) of 49 Å.

To see if this is reasonable, we take $\Delta(0) = 1.83T_c$ for $ErNi_2B_2C$ [122], for which the BCS coherence length $\xi_{0BCS}^{\Delta} = \hbar v_F/\pi\Delta(0) = 470$ Å, where $v_F = 3.6 \times 10^5$ m/s is taken from band-structure calculations for $LuNi_2B_2C$ and YNi_2B_2C [127]. Using the relation

$$H_{c2}(0) = 0.693T_c(\frac{dH_{c2}}{dT})\Big|_{T_c}, \tag{7.16}$$

and $dH_{c2}/dT|_{T_c}$ ($H \parallel c$) = -2.67 kOe/K [103], we obtain the coherence length

$$\xi_0^{H_{c2}} = \sqrt{\frac{\phi_0}{2\pi H_{c2}(0)}} = 130 \text{ Å}. \tag{7.17}$$

Finally, using the relation [95]

$$\xi_0^{H_{c2}} = 0.85(\xi_{0BCS}^{\Delta} l)^{1/2}, \tag{7.18}$$

we obtain the mfp l = 42 Å. On the other hand, from the resistivity value just above T_c, $\rho(T_c^*)$ = 5.8 $\mu\Omega$-cm, we get l = 56 Å. These two values agree well with the value of 49 Å calculated from $1/\tau\Delta_0 = 24$ obtained earlier, implying that this particular value of the non-magnetic scattering rate needed to explain our ρ_s data is consistent with H_{c2} data. Note that this value of mfp calculated from H_{c2} data does not depend on the exact value of T_c. Also, the prefactors 0.693 and 0.85 in the above relations are for materials in the dirty limit. Here l $< \xi_0$, so our $ErNi_2B_2C$ sample may be considered as "quasidirty". Moreover, in this sample the non-magnetic scattering rate ($1/\tau$) is at least two orders of magnitude larger than the effective magnetic scattering rate ($1/\tau_2^{eff}$), thus the mfp value is largely determined by $1/\tau$. Our mfp value, however, is smaller than the 90 Å obtained from resistivity measurements just above T_c in Ref. [128]. The CNNL model is thus able to explain our superfluid density data, both qualitatively and quantitatively. Our data, in agreement with others, also shows that AF order coexists with superconductivity below T_N.

We turn next to an alternative explanation for the negligible change of ρ_s at T_N. Ramakrishnan and Varma [112] predicted that for materials with a nested FS, since the peak in susceptibility and the joint density of states (defined as the difference between the susceptibility in the superconducting state and the normal state) occur at the same Q-value, one should expect an increase in pair-breaking at T_N. Conversely, a non-nested FS will give rise to decreased pair-breaking at T_N (see Fig. 7.14). Two-dimensional angular correlation of

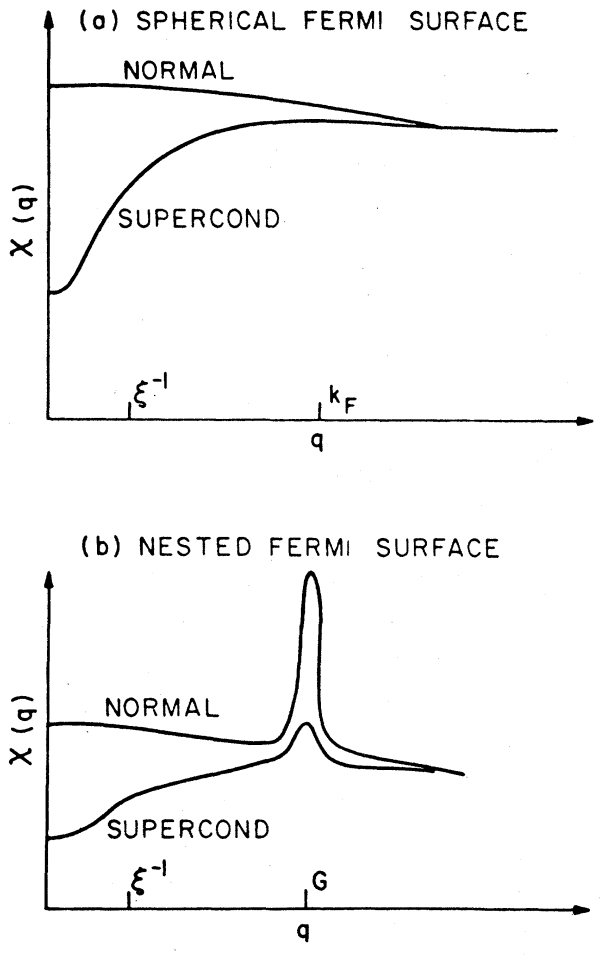

Figure 7.14: (a) Schematic representation of the q-dependence of the conduction-electron susceptibility for the normal state and the superconducting state for a metal with a spherical FS. (b) Same as (a) for a metal with a FS with nesting near $q = G$. Taken from Ref. [112].

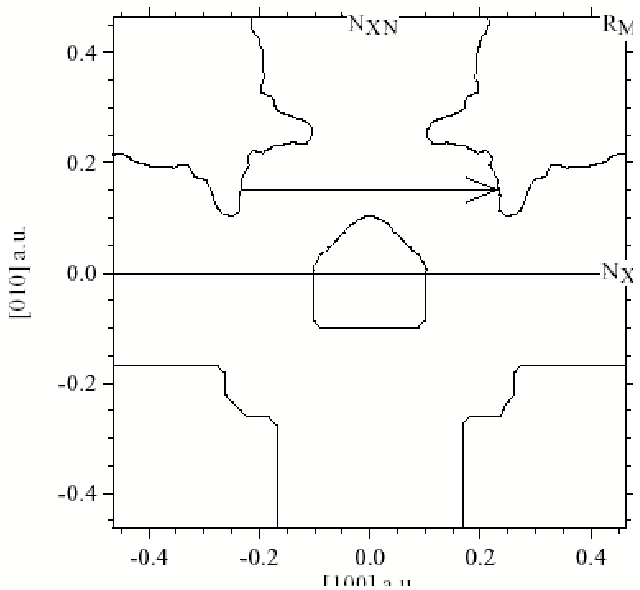

Figure 7.15: The experimental (top) and calculated (bottom) FS topology of $LuNi_2B_2C$. The calculation is of the FS in the third band in the (001) plane through the Γ point. The arrow indicates the nesting feature. Taken from Ref. [123].

electron-positron annihilation radiation measurements show that only one out of the three FS sheets in $LuNi_2B_2C$ possesses nesting properties, thereby accounting for the propensity for magnetic ordering found in the other magnetic members of the RE nickel borocarbides [123] (Fig. 7.15). Also, Dugdale *et al.* [123] estimated that the fraction of the FS that would be able to participate in nesting is only 4.4%. Contrast this with CNNL model, which assumes perfect 1-D nesting. Hence the increased pair-breaking due to partial nesting on one FS sheet is compensated by decreased pair-breaking by the other two sheets, resulting in negligible change in pair-breaking at T_N.

As temperature further reduces below T_N, the theoretical curve in Fig. 7.10 overestimates the experimental curve below 3 K ($\sim 0.3T_c$). This is due to additional pair-breaking effects of WFM, which shows up as a small peak near $T_{WFM} = 2.3$ K (see Fig. 7.9). This is the first observation of WFM in penetration depth measurements. The small dip in superfluid density shows that this WFM slightly depresses, but does not completely destroy, superconductivity, demonstrating the coexistence of WFM and superconductivity. We model this WFM by

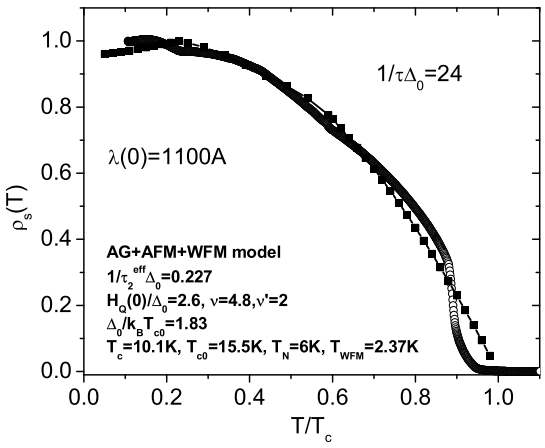

Figure 7.16: $\rho_s(T)$ from 0.1 K to T_c. ($\bigcirc$) data. Solid squares = Fitting curve incorporating WFM.

including a temperature-dependent magnetic impurity scattering rate $1/\tau_2^{WFM} = 1/20(g_J - 1)J(J+1)(1 - T/T_{WFM})^{\nu'}$ (with the same value of g_J and J as before), and adding this to the previous effective magnetic scattering rate, i.e. $1/\tau_2^{total} = 1/\tau_2^{eff} + 1/\tau_2^{WFM}$ when $T < T_{WFM}$. The pre-factor $1/20$ arises from the fact that one out of every 20 spins contributes to the WFM [129], giving rise to a weak magnetization. The temperature dependence $(1 - T/T_{WFM})^{\nu'}$ is analogous to the molecular field formulation. We obtain $\nu' \approx 2$ from Jensen's calculation [130] or Choi and Canfield's data [102, 105]. Fig. 7.16 shows ρ_s when one accounts for WFM. Agreement between theory and data is good. The dip in ρ_s is reproduced, though it still overestimates ρ_s near 3 K. This can be explained by neutron-scattering data, which shows that this weak ferromagnetic component already shows up at 3 K [102]. There is as yet no direct measurement of superconducting gap amplitude at this temperature range, though our model predicts a drop in Δ there.

Finally we turn to another small peak in $\Delta\lambda$ near 1.1 K (see Fig. 7.9), which looks similar to the WFM peak at 2.3 K. This peak has not been observed elsewhere, mainly because experiments have not been carried out at such low temperatures and high precision.

We conjecture that this is a second weak ferromagnetic component, of similar origin to the first. We await other experiments to confirm our observation.

7.4 Conclusion

In conclusion, we present in-plane penetration depth data of single-crystal $ErNi_2B_2C$ down to 0.1 K. The negligible change in pair-breaking at T_N can be attributed to the near-complete cancellation of the effects of the AF molecular field and spin-fluctuation scattering. It could also be due to the combined effects of non-perfect nesting on one piece of the FS and non-nesting on other pieces of the FS. The increased pair-breaking at T_{WFM} is modelled by a magnetic impurity scattering parameter, and both magnetic orders coexist with superconductivity. We also see the first observation of a possible second weak ferromagnetic component near 1.1 K. This observation has to await confirmation from other experiments.

I wish to thank Professor Y. C. Chang for teaching me the computational aspects of the Chi-Nagi model, and Professor C. Varma for encouraging discussions on my interpretation of the data. I also thank Dr. Tuson Park for taking the resistivity data. The data were taken from samples obtained from Professor S.-I. Lee.

Chapter 8

$HoNi_2B_2C$: Interplay between superconducting and magnetic order

8.1 Introduction

The family of quarternary compounds RENi2B2C (RE = rare-earth) have attracted much interest due to the considerable interaction among their superconducting and magnetic properties [73]. $HoNi_2B_2C$ in particular, exhibits rich behavior due to this interplay within a narrow temperature range. It becomes superconducting at ~ 8 K, then reenters the normal state at ~ 5 K, only to quickly become superconducting again with further reduction of temperature [73]. In the same temperature range three types of magnetic order were observed in the Ho f electron sublattice [97]: (a) a commensurate antiferromagnetic structure below 5 K, which consists of sheets of ferromagnetic moments in the $a-b$ plane, with adjacent sheets coupled antiferromagnetically along the c-axis; (b) an incommensurate c-axis helical magnetic state at ≈ 8.5 K; (c) another incommensurate a-axis modulation at ≈ 6.3 K. A deep minimum in H_{c2} near 5 K [73] showed that superconductivity is reentrant, below which both the c- and a-axis incommensurate structures disappear, or lock into the commensurate structure. Once the system is in the commensurate antiferromagnetic state, this permits the return of superconductivity, and long-range antiferromagnetic order coexists with superconductivity at low temperatures. Here we report measurements of the in-plane magnetic penetration depth $\lambda(T)$ in single crystals of $HoNi_2B_2C$ from T_c down to 0.1 K. The samples

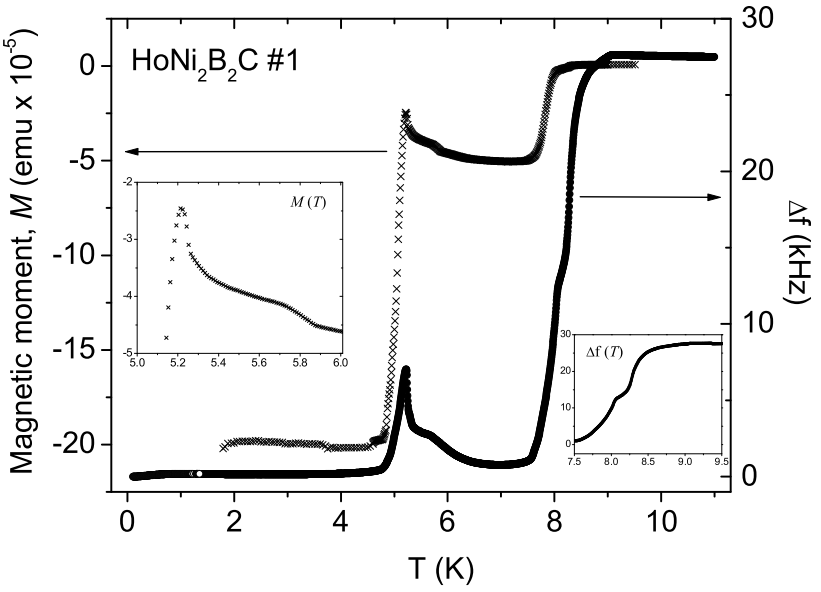

Figure 8.1: $\Delta f(T)$ for $T = 0.1$ K–11 K (solid circles) and zero-field-cooled $M(T)$ for T = 1.8 K–9 K (crosses) as a function of temperature for sample #1. Insets show $\Delta f(T)$ features around 8 K, and $M(T)$ features around 5 K, in greater detail.

come from the same batch, and we label them sample #1 and #2, with sample #2 being slightly smaller in dimensions. We do not convert Δf to $\Delta\lambda$ in this chapter, since we are looking only at qualitative features. Moreover, as explained in Section 6.3, we do not know if the low-T downturn is real, so it is problematic to convert the data to superfluid density. The results of this chapter were published in the Journal of Magnetism and Magnetic Materials, volume 226, pages 301-303 (2001).

8.2 Data and Analysis

Fig. 8.1 shows $\Delta f(T)$ and the zero-field-cooled dc magnetization $M(T)$ as a function of temperature for sample #1. The insets expand the regions around 8 K for $\Delta f(T)$ and 5 K for $M(T)$. We see a broad decrease in $\Delta f(T)$ beginning near 9 K and leveling off before dropping sharply at 8 K. Comparing with the magnetization data, it is generally

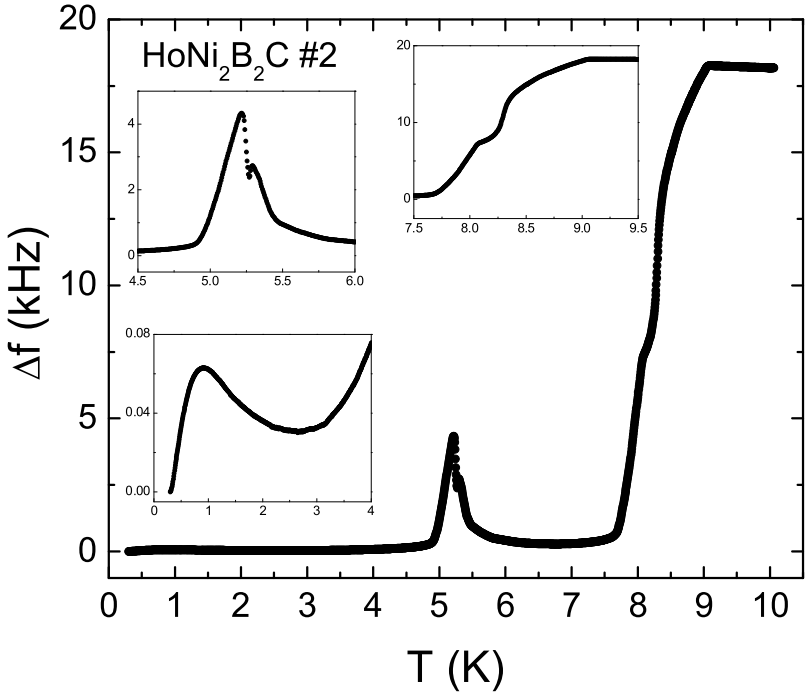

Figure 8.2: $\Delta f(T)$ as a function of temperature in the temperature range (0.3–10) K for sample #2. The insets show the low-temperature region, the 5 K-peaks and the 8 K-shoulder in greater detail.

agreed that bulk superconductivity sets in at 8 K. There is evidently a significantly loss of rf penetration between the Neel temperature $T_N \sim 8.5$ K and $T_c \sim 8$ K, and that could be due to the onset of weak superconductivity at ~ 9 K with very small H_{c1}. In addition, we see dramatic increases in $\Delta f(T)$ starting near 6.5 K and peaking at 5.2 K. The 5.2 K-peak most certainly corresponds to the commensurate antiferromagnetic state. The rise near 6.5 K can be correlated with the incommensurate a-axis transition at 6.3 K reported previously [97]. Just below the 5.2 K peak, $\Delta f(T)$ drops abruptly, suggesting a reentrant superconducting state. The $M(T)$ data of sample #1 (1.8 K–9 K), in an applied field of 5 G parallel to the c-axis of the crystal, agree with the general features of the $\Delta f(T)$ data: superconducting transition at 8 K, knee at 5.7 K, and reentrant superconductivity below 5.2 K. It also shows that the sample does not go completely normal at 5.2 K, agreeing with our penetration depth data. When we measured $M(T)$ at 20 G, however, the material goes completely normal at 5.2 K. This can be attributed to flux penetration, since the applied field is comparable to H_{c1} at this temperature. We also note that our results differ from [73], where for H parallel to the c-axis the reentrant behavior was only barely visible for 200 G $< H <$ 500 G. Ours also differ from [131], where the reentrant behavior was visible only for powdered samples at 1 G, not for annealed bulk samples. Fig. 8.2 shows a similar structure from sample #2, though the shoulder at 8 K is more pronounced, and the features near 5 K are closer together and resolved as two peaks at 5.2 K and 5.3 K. The 5.3 K-peak of sample #2, and the 5.7 K-knee of sample #1, may be related to the two shoulders in the specific heat data seen in [73]. The slight difference between samples #1 and #2 may reflect the sensitivity of magnetic ordering on surface composition, on whether the different magnetic states come from the same region of the sample's surface [97]. For both samples, the peak frequency shift at 5.2 K is significantly smaller than the ~ 9 K value, suggesting that the c-axis helical phase significantly reduces the density of Cooper pairs, but does not completely destroy superconductivity, in agreement with Ref. [80].

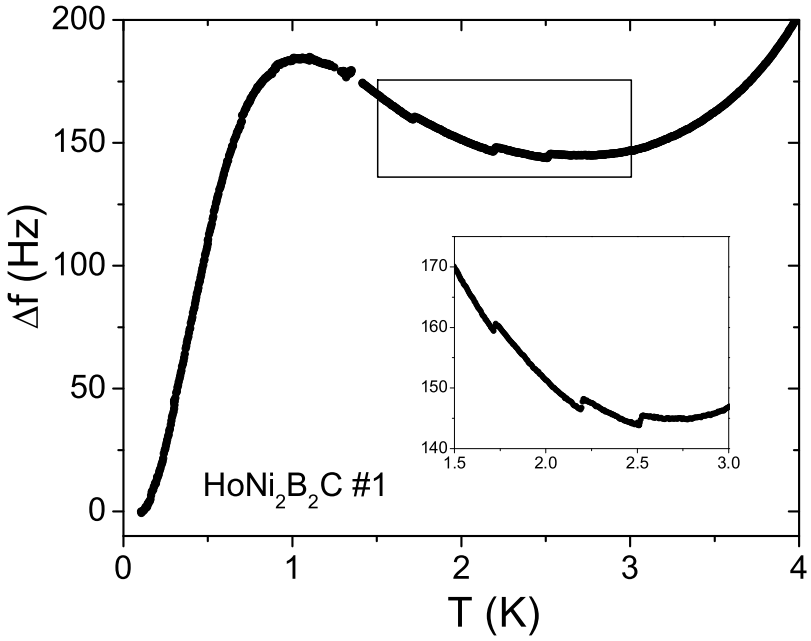

Figure 8.3: $\Delta f(T)$ as a function of temperature for sample #1 at low temperatures. Inset shows the three jumps between 1.7 K and 2.5 K.

Fig. 8.3 expands the lower temperature regions of Fig. 8.1. Below 3 K $\Delta f(T)$ increases with decreasing T, but only by $\sim 0.2\%$ of the total signal. This agrees with Ref. [80], and possibly suggests a new source of magnetic scattering below 3 K. Lying on top of this increase are three previously unreported, smaller jumps near 1.7 K, 2.2 K, and 2.5 K. The magnitude of these peaks ($\sim$ 1 Hz) is $\sim 10^{-8}$ of the total signal, and appear on repeated runs on sample #1. These may be additional magnetic transitions that the material goes through as temperature is lowered, corresponding to reorientations of the Ho magnetic moments as they reach the true ground state of the system. Lastly, $\Delta f(T)$ increases to a broad maximum near 1 K, then displays the expected decrease at the lowest temperatures down to 100 mK. The rise of $\Delta f(T)$ from 3 K to a broad maximum near 1 K, and the eventual decrease at the lowest temperatures, are also seen in sample #2. However, sample #2 does not display the three smaller jumps that sample #1 exhibits, perhaps because sample #2, being smaller in size, gives a signal comparable to the noise of the system.

The downturn below 1 K has been seen in all the magnetic *and* non-magnetic borocarbide samples I measured: $LuNi_2B_2C$, YNi_2B_2C, $ErNi_2B_2C$, and $HoNi_2B_2C$. This could mean that the rare-earth borocarbides are multi-gap superconductors, with the small downturn due to the opening up of the second superconducting gap on a different Fermi sheet. This could also be an extrinsic effect, for example, due to flux on the surface, and even penetrating through, the samples, since these are flux-grown sample. Scanning Electron Microscope analysis on some of the samples show a blobs of Ni on parts of the surface. They could be Ni_2B flux.

8.3 Conclusion

In conclusion, we report measurements of the magnetic penetration depth in single crystals of $HoNi_2B_2C$ down to 100 mK using a tunnel-diode based, self-inductive technique at 28 MHz. We observe a sharp decrease in the rf penetration depth $\lambda(T)$ at the superconducting transition near 9 K. A pronounced shoulder appears at approximately 8 K, followed by

dramatic increases in $\lambda(T)$ at 5.7 K and 5.2 K. These increases correspond approximately to the onsets of previously reported magnetic structures. Just below the 5.2 K peak, $\lambda(T)$ drops abruptly, suggesting a reentrant superconducting state. Below 3 K, $\lambda(T)$ increases gradually to a broad maximum near 1 K, then decreases again. In addition, three previously unreported, smaller transitions are observed between 1.7 K and 2.5 K. It appears that the c-axis helical phase inhibits the increase in the density of Cooper pairs, but does not destroy superconductivity. Magnetization data of $HoNi_2B_2C$ is also presented for comparison. I thank Professor S.-I. Lee for providing the samples.

Chapter 9

Sr_2RuO_4

9.1 Introduction

Sr_2RuO_4 has the same layered-perovskite K_2NiF_4-type crystal structure as the high-T_c cuprate superconductor $La_{2-x}Ba_xCuO_4$ [138]. The transition temperature of Sr_2RuO_4 has now reached $T_c = 1.50$ K, which is very close to the intrinsic value for this superconductor [139]. Table 9.1 summarizes some of the anisotropic superconducting parameters based on the observed critical fields and specific heat [132], along with values for other superconductors for comparison. Fig. 9.1 depicts its Fermi surface (FS), consisting of three nearly cylindrical sheets called α, β, and γ [137]. They originate from different orbitals of Ru $4d$ electrons. Comparison with some other superconductors, based on Table 9.1, leads to a few observations: firstly, for the zero-temperature penetration depth $\lambda(0)$, $\lambda_{SRO}(0) > \lambda_{YBCO}(0)$ $> \lambda_{Al}(0)$, which imply that the carrier density in Sr_2RuO_4 is relatively low compared to Al. This means that the carriers are less heavily screened than they are in ordinary metals and makes the Coulomb repulsion between them more important. Secondly, for the coherence length ξ, $\xi_{YBCO} < \xi_{SRO} < \xi_{Al}$, which makes thermal fluctuations in Sr_2RuO_4 larger than in Al, and also makes defects such as impurity concentrations, grain boundaries and surface rearrangements much more important than in Al, but perhaps less so than in YBCO. Thirdly, in comparing Sr_2RuO_4 with the heavy-fermion superconductor UPt_3, both of which have similar T_c's, we see that they have roughly comparable ξ's and λ's to the same order of magnitude. In fact, we will see later from Knight shift and other experiments that both

	Sr_2RuO_4 [132]	YBCO [133]	UPt_3 [134, 135]	Al [136]
T_c(K)	1.49	92	0.46	1.18
$\xi_{ab}(0)$(Å)	660	12	200	16000
$\xi_c(0)$(Å)	33	3		
$\lambda_{ab}(0)$(Å)	1800	890	7820	400
$\lambda_c(0)$(Å)	37000	5500	7070	
$\kappa_{ab}(0)$(Å)	55	74	23	0.03
$\kappa_c(0)$(Å)	2.7	2750		

Table 9.1: Anisotropic superconducting parameters of Sr_2RuO_4. $\xi(0)$ is the coherence length at $T = 0$ K, $\lambda(0)$ is the penetration depth, and $\kappa(0)$ is the Ginsburg-Landau (GL) parameter. The mean free path of the Sr_2RuO_4 crystal used for the measurement is $l = 2100$ Å. Corresponding values of a few superconductors are listed for comparison. YBCO $\equiv YBa_2Cu_3O_{7-\delta}$.

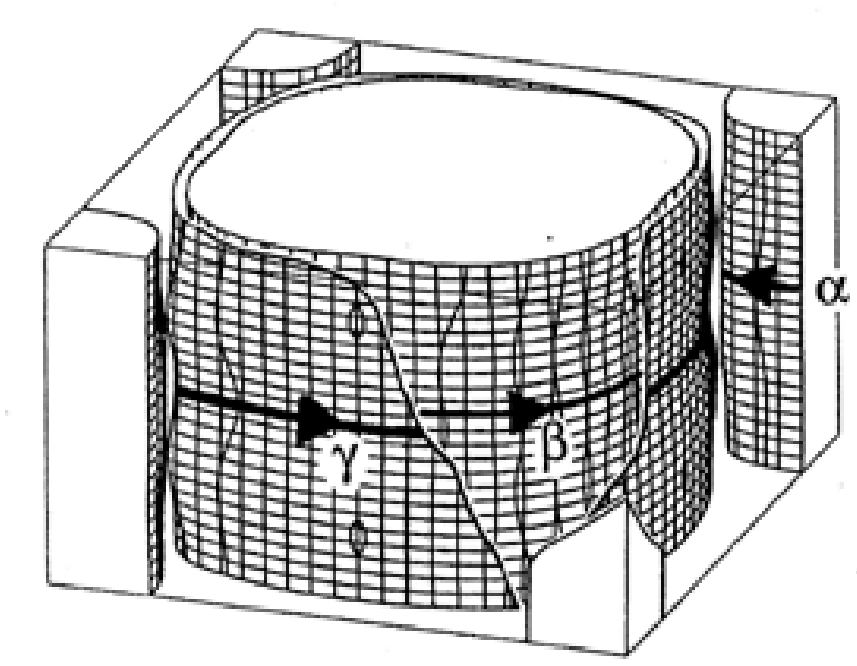

Figure 9.1: The Fermi surface of Sr_2RuO_4. It consists of three slightly warped cylinders with axes along the c-axis. γ and β are electron surfaces, while α is a hole surface. Taken from Ref. [137].

of them are spin-triplet superconductors. Sr_2RuO_4 has generated so much interest due to the possibility of spin-triplet pairing. Early experimental evidence for unconventional superconductivity was in the absence of the Hebel-Slichter peak in the Ru nuclear relaxation rate [140]. The non-s-wave character of the superconductivity has been established by the extreme sensitivity of T_c to non-magnetic impurities and defects [141, 142].

9.2 Spin-triplet superconductivity

This section follows that of Ref. [139]. We can represent the spin-triplet wave function in terms of the "**d**-vector" [143]. As described in Section 2.2, Eqn. 2.17, the superconducting gap function (or order parameter) $\Delta(\mathbf{k})$ is represented by the 2×2 matrix

$$\hat{\Delta}(\mathbf{k}) = \begin{pmatrix} \Delta_{\uparrow\uparrow} & \Delta_{\uparrow\downarrow} \\ \Delta_{\downarrow\uparrow} & \Delta_{\downarrow\downarrow} \end{pmatrix} = \begin{pmatrix} -d_x(\mathbf{k}) + id_y(\mathbf{k}) & d_z(\mathbf{k}) \\ d_z(\mathbf{k}) & d_x(\mathbf{k}) + id_y(\mathbf{k}) \end{pmatrix}, \tag{9.1}$$

where $\Delta_{\uparrow\downarrow} = \Delta_{\downarrow\uparrow} \equiv \Delta_0$ and $\mathbf{k} = (\mathrm{k}_x, \mathrm{k}_y, \mathrm{k}_z)$ is the vector specifying the direction in the momentum space. We introduce the **d**-vector

$$\begin{aligned} \mathbf{d} &= d_x\mathbf{x} + d_y\mathbf{y} + d_z\mathbf{z} \\ &= \frac{1}{\sqrt{2}}\left\{\Delta_{\uparrow\uparrow}|\uparrow\uparrow\rangle + \Delta_{\downarrow\downarrow}|\downarrow\downarrow\rangle + \Delta_0(|\uparrow\downarrow\rangle + |\downarrow\uparrow\rangle)\right\}. \end{aligned} \tag{9.2}$$

The **d**-vector $\mathbf{d}(\mathbf{k}) = (\mathrm{d}_x, \mathrm{d}_y, \mathrm{d}_z)$ can now be transformed as a three-dimensional vector under rotation in spin space. The relation between the two representations is shown in Eqn. 9.1.

Let us take the wave function $\mathbf{d} = \mathbf{z}(k_x + ik_y) \equiv \mathbf{z}f(\mathbf{k})$, for example, since, we shall show later, that this **d**-vector is compatible with some existing experimental observations. The *spin* part of the wave function consists of only the $\mathbf{z} = |S_z = 0\rangle = 2^{-1/2}\{|\uparrow\downarrow\rangle + |\downarrow\uparrow\rangle\}$ component. This means that the parallel spins of the Cooper pairs are in the plane normal to the z-direction. In the presence of weak spin-orbit interaction, it is natural to take

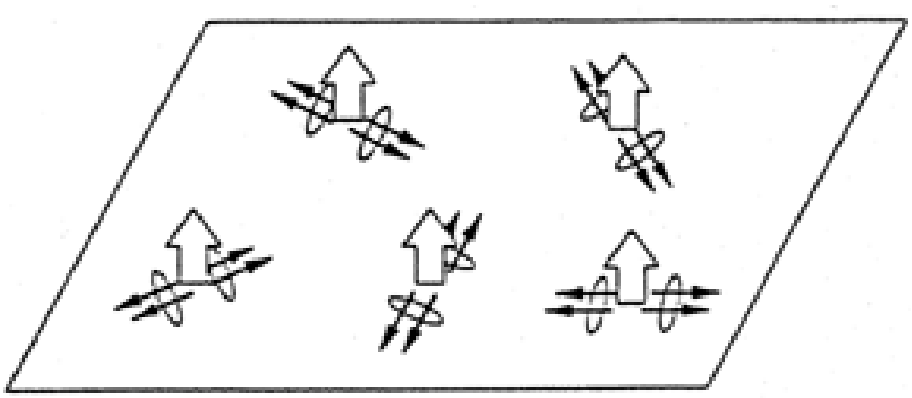

Figure 9.2: Schematic representation of the spin and orbital parts of the spin-triplet pairing function $\mathbf{d} = \mathbf{z}\ (k_x + ik_y)$ on the RuO_2 plane. The pairs of thin arrows depict the spin part $\mathbf{z}$, whereas the thick open arrows indicate the orbital part with angular momentum $L_z = +1$. Taken from Ref. [139].

the z-direction along the c-axis. As depicted in Fig. 9.2 by the pairs of thin arrows, for an arbitrary quantization axis x' within the plane, the spin wave function is the equally weighted superposition of the $\uparrow\uparrow$ and $\downarrow\downarrow$ pairs, i.e.

$$\begin{aligned} \mathbf{z} &= \frac{-i}{2}\{|\uparrow\uparrow\rangle_{x'} + |\downarrow\downarrow\rangle_{x'}\} \\ &= \frac{-i}{2}\{(-\mathbf{y}' + i\mathbf{z}) + (\mathbf{y}' + i\mathbf{z})\}. \end{aligned} \tag{9.3}$$

The *orbital* part of the wave function, $k_x + ik_y$, can be described by the spherical harmonic $Y_1^{-1}(\mathbf{k}) \propto \sin\theta\ e^{i\phi}$ for the relative motion of the paired electrons. Its orbital angular momentum, $L_z = +1$, is depicted in Fig. 9.2 by the thick open arrows. The superconducting gap is proportional to $(\mathbf{d} \cdot \mathbf{d}^*)^{1/2} = (\mathrm{k}_x^2 + \mathrm{k}_y^2)^{1/2}$ and is therefore isotropic.

9.3 Experimental results

Many experiments confirm the unconventional nature of superconductivity in Sr_2RuO_4. The NMR nuclear-spin lattice relaxation rate $1/T_1$ decreases sharply without the coherence peak just below T_c, suggesting an unconventional pairing state [140]. Knight shift for field parallel

to the basal plane remains unchanged as one goes below T_c, suggesting a spin-triplet structure [144]. For comparison, the Knight shift should decrease below T_c for a spin-singlet d-wave. It can be shown that for the equal-spin-pairing (ESP) state, as depicted in Fig. 9.2, the Cooper pairs consist of the spin pairs $|\uparrow\uparrow\rangle$ and $|\downarrow\downarrow\rangle$ with their quantization axis perpendicular to the c-axis direction. As a result, an invariant spin susceptibility χ_s is expected when the field is parallel to any direction within the a-b plane [12]. The experimental results clearly demonstrate no change of the spin susceptibility of Cooper pairs, and therefore lead to the definitive conclusion that spin-triplet superconductivity is realized in Sr_2RuO_4. Muon-spin relaxation data [145] show the presence of a spontaneous magnetic field appearing within the superconducting state. This indicates that the superconducting state of Sr_2RuO_4 is a time-reversal-symmetry-breaking (TRSB) state.

The above experiments were explained by the p-wave spin-triplet state with the order parameter [5]

$$\mathbf{d}_1(\mathbf{k}) = \mathbf{z}\Delta_1(T)(\hat{k}_x + i\hat{k}_y), \tag{9.4}$$

where Δ_1 is the $\mathbf{k}$-independent part of the gap. This state is analogous to the A-phase of superfluid ^{3}He [12], which has point nodes of the energy gap at $k_x = k_y = 0$ on the spherical FS, i.e. the north and south poles. However, since the FS of Sr_2RuO_4 consists of three cylindrical surfaces, the above p-wave state would not have nodes even if there were states $k_x = k_y = 0$, hence it has a finite energy gap on the FS. This implies that the low-temperature behavior of electrodynamic and thermodynamic quantities like penetration depth and specific heat should exhibit an activated behavior, i.e. exponential T-dependence at low temperatures. However, specific heat measurements [139] give C(T) $\propto T^2$, and the NMR $1/T_1 \propto T^3$ at low temperatures [139]. These temperature dependences are interpreted as a consequence of line nodes in the energy gap. However, thermal conductivity measurements [146] gave no evidence of strong anisotropy of the gap in the basal plane, essentially excluding vertical line nodes. If present at all, nodes would have to be horizontal, i.e. parallel to the (k_x,k_y)-plane

[147]. By contrast, the p-wave state in Eqn. 9.4 has an isotropic energy gap, i.e. does not have any nodes. Hence the p-wave pairing state in Eqn. 9.4 seems unable to describe the pairing mechanism for Sr_2RuO_4.

Penetration depth measurements on a pure sample (T_c = 1.5 K) were performed by Bonalde *et al.* [4], and it gives a T^2 dependence up to $0.6T_c$, which the authors attributed to the presence of line nodes, with the extra factor T coming from nonlocal corrections instead of impurity scattering (see Fig. 9.3). Later we took another on another pure sample with T_c = 1.43 K (not converted to $\Delta\lambda$), and also obtained a T^2 low-temperature dependence up to $0.53T_c$ (see Fig. 9.4). However, Kusunose and Sigrist [KS] [5], using the idea first proposed by Zhitomirsky and Rice [148], performed a calculation on Sr_2RuO_4 which incorporates multiple bands, nonlocality and horizontal line nodes, where the main "active" γ band $\Delta_1(T)$ is fully gapped with p-wave symmetry of the form in Eqn. 9.4, while the "passive" α and β bands have horizontal line nodes with an order parameter of the form [5]

$$\mathbf{d}_2(\mathbf{k}) = \mathbf{z}\Delta_2(T)(\hat{k}_x + i\hat{k}_y)cos(k_z c/2). \tag{9.5}$$

In the "one-band" limit, where interband scattering is absent, only the quasiparticles from the passive bands contribute to the low-temperature behavior, while those in the totally gapped dominant band are inactive. In this one-band Pippard limit [5],

$$\frac{\Delta\lambda(T)}{\lambda(0)} = \frac{1}{18}\left(\frac{T}{T_p}\right)^2 + \frac{83}{3240}\left(\frac{T}{T_p}\right)^4, \tag{9.6}$$

where $T_p = \Delta_2(0)/\pi$. So $\Delta(T) \propto T^2$ only at very low temperatures, specifically $T < T^*$ $\approx 0.3T_p$. Even with the maximal gap, $\Delta_2(0) = \Delta_{BCS}$ ($= 1.76T_c$), $T^* < 0.17T_c \approx 0.26$ K. That is, the T^2-behavior should only be seen below 0.26 K, and not 0.9 K as observed in Ref. [4]. Hence a single-gap model, even with nonlocality and horizontal line nodes, is unable to explain the T^2-behavior of penetration depth over a *wide* temperature range.

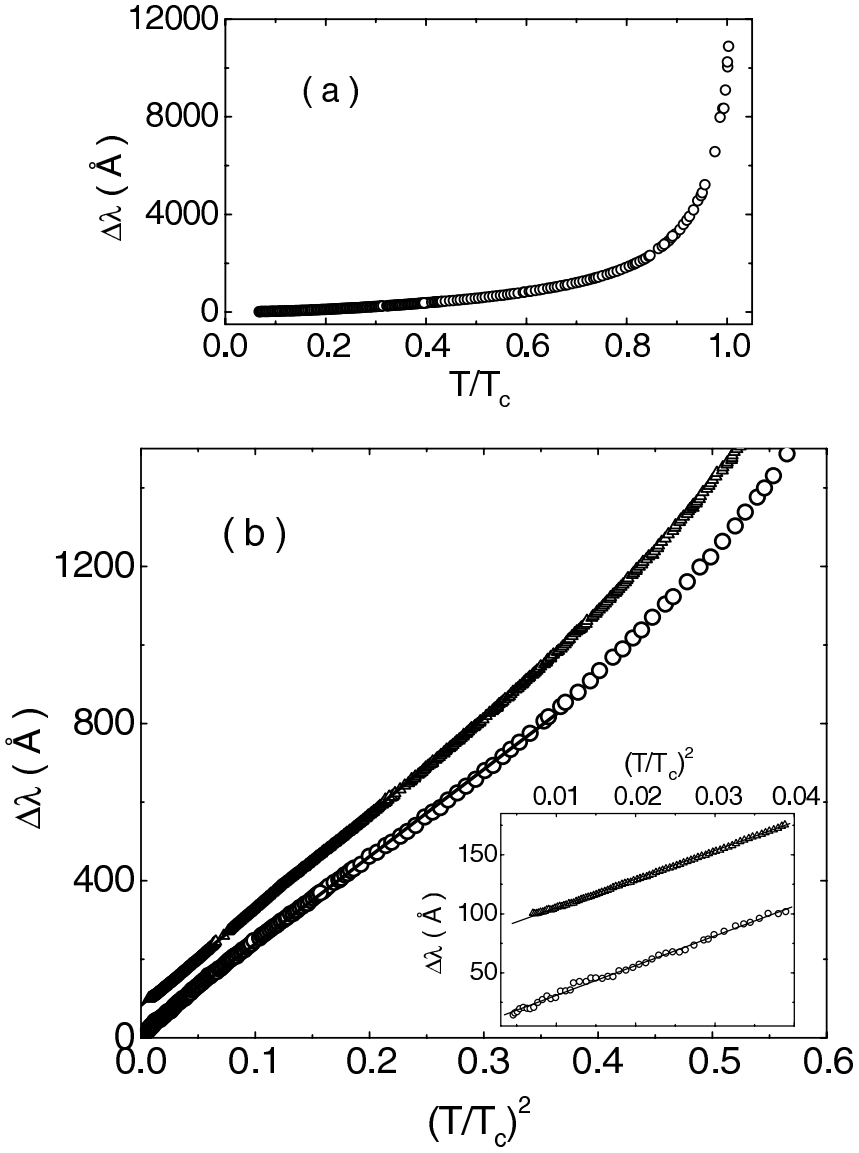

Figure 9.3: (a) $\Delta\lambda(T)$ vs T/T_c for sample 1 of Ref. [4]. (b) $\Delta\lambda(T)$ vs $(T/T_c)^2$ in the temperature range (0.04-1.16) K for samples 1 (◯) and 3 (△), and the inset shows the low temperature regime $T < 0.2T_c$ for the same data. All straight lines are fits to the data. The data have been shifted for clarity. Taken from Ref. [4].

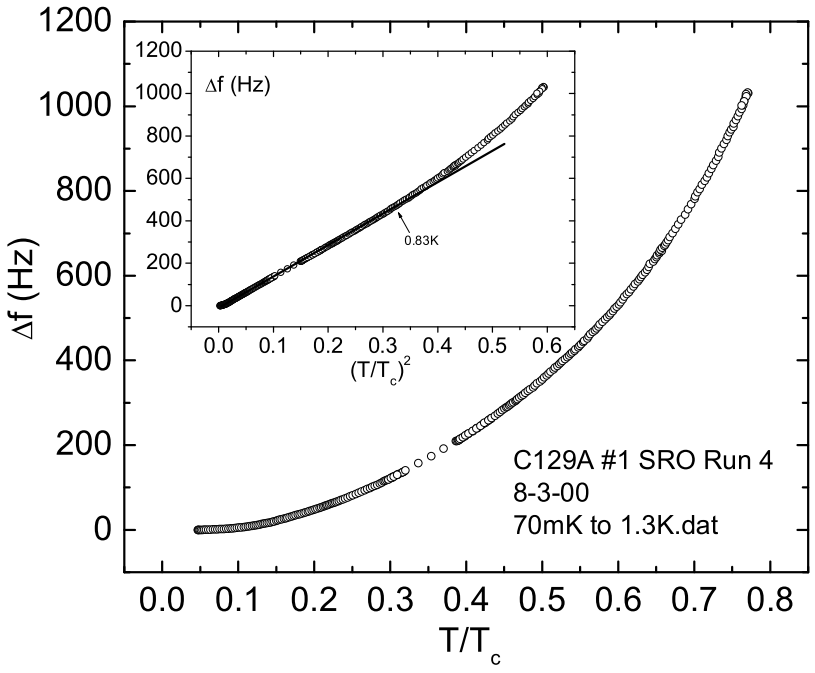

Figure 9.4: Δf vs T/T_c of another pure Sr_2RuO_4 sample (C129A, $T_c = 1.43$ K). Inset shows the low temperature region plotted against $(T/T_c)^2$. The straight line is a fit to $0.53T_c$.

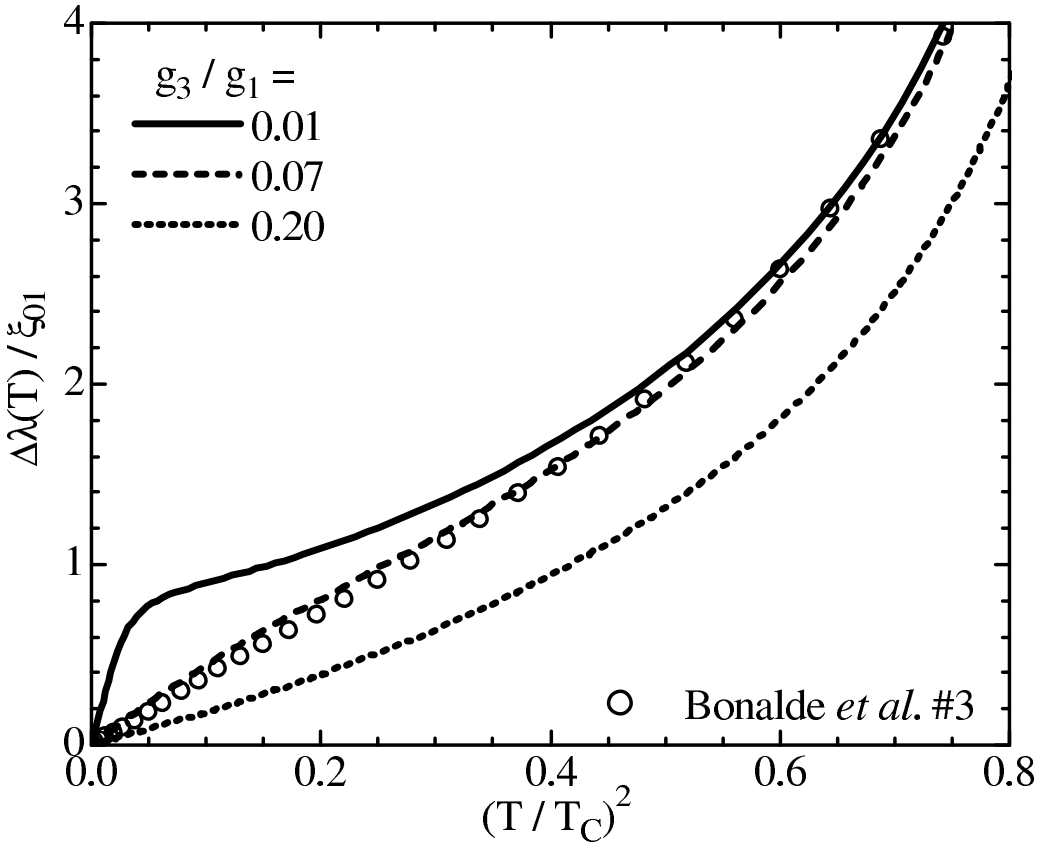

Figure 9.5: Calculated $\Delta\lambda(T)$ for different g_3/g_1. The other parameters are fixed at $g_1 = 0.4$, $g_2/g_1 = 0.85$ and $\kappa_1 = 2.3$ (GL parameter of the active band). A moderate interband coupling fits well the observed temperature dependence. The open circles are the experimental data of Bonalde *et al.* [4]. Taken from Ref. [5].

KS then turned to the multi-gap scenario for Sr_2RuO_4, in which the temperature dependence of the gap magnitudes are given by an effective two-band model: $\Delta_\alpha = \Delta_\beta = \Delta_2(T)$ and $\Delta_\gamma = \Delta_1(T)$. Moreover, the pairing interactions in the gap equations are momentum-*dependent*, defined as $V_{11} = -g_1 \hat{\mathbf{k}} \cdot \hat{\mathbf{k}'}$, $V_{22} = -2g_2(\hat{\mathbf{k}} \cdot \hat{\mathbf{k}'}) \cos(k_z c/2) \cos(k'_z c/2)$ for intraband coupling, and $V_{12} = -\sqrt{2} g_3 (\hat{\mathbf{k}} \cdot \hat{\mathbf{k}'}) \cos(k'_z c/2)$ for the interband Cooper pair scattering. Then, with these intraband and interband coupling parameters, as well as other material parameters, they performed the same nonlocal calculations as in the one-band case, and are able to fit the penetration depth data over a wider temperature range (see Fig. 9.5). In the fit the GL parameter of the active band, κ_1, is found to be 2.3. This is slightly smaller than the generally cited value $\kappa \approx 2.6$ [5]. They also found that the same set of interband and intraband scattering parameters ($g_1 = 0.4$, $g_2 = 0.34$, $g_3 = 0.028$) is able to explain the temperature dependence of both the penetration depth and specific heat data. The apparent T^2-dependence of the penetration depth on a pure Sr_2RuO_4 sample is an accidental one. However, in the same paper, the authors also considered the case where the passive gap is nodeless, i.e. $\mathbf{d}_2 = \mathbf{z}\Delta_2(T)(\hat{k}_x + i\hat{k}_y)$. Trying the same fitting procedure, they find only a minor difference at very low temperatures compared to the the previous fit. While the difference is small in $\lambda(T)$, horizontal line nodes are necessary to fit the specific heat data [148]. Hence it is not possible, using penetration depth data from the pure samples, to ascertain the detailed gap structure of Sr_2RuO_4. Also, Ref. [5] did not attempt to explain the T^3-dependence of dirty samples, which will be described in the next paragraphs.

Bonalde *et al.* also performed penetration depth measurements on a dirty sample ($T_c = 0.82$ K) [4], and obtained a T^3-dependence, which they attributed to the combined effects of nonlocality and impurity scattering, each giving an extra factor T besides the linear T expected for line nodes. However, in the dirty limit ξ no longer diverges near the nodes, and hence the nonlocal condition $\xi \gg \lambda$ no longer applies, so one should expect only a T^2 dependence and not T^3. Bonalde *et al.* argued that since the GL parameter κ is not large in Sr_2RuO_4, $\kappa = \lambda/\xi \approx 2$–3, a large portion of the FS near the nodes fulfills the nonlocal

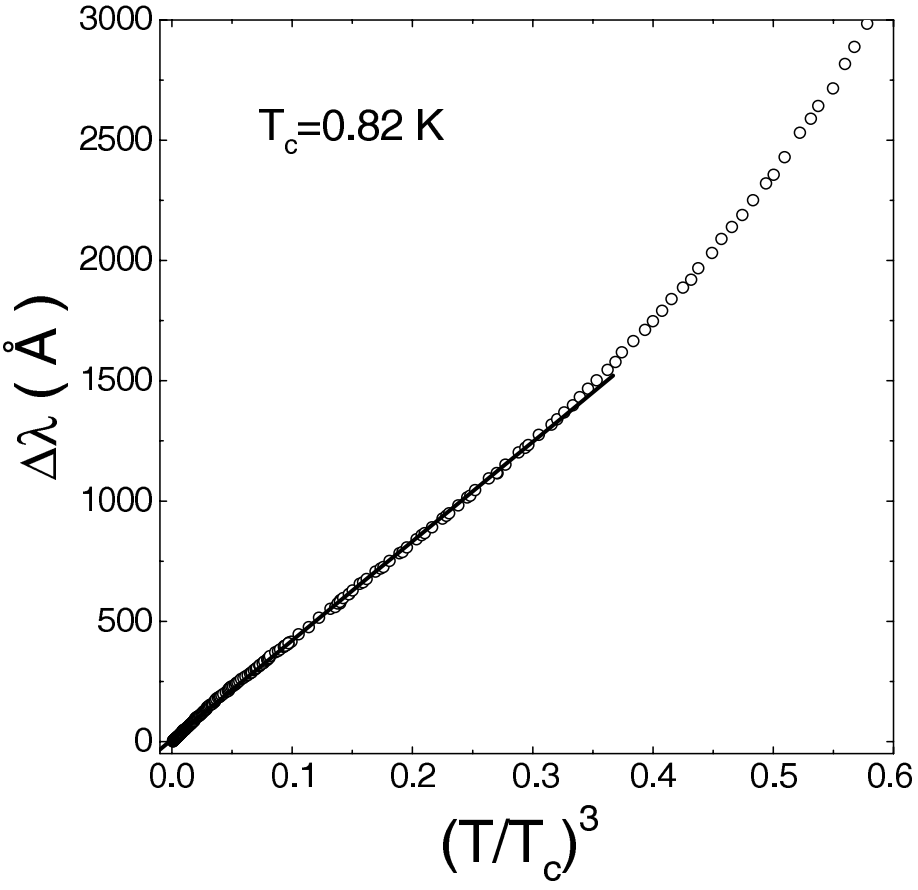

Figure 9.6: $\Delta\lambda(T)$ vs $(T/T_c)^3$ in the temperature range (0.040.69) K for an impure sample ($T_c = 0.82$ K). The line is a fit to the data. Taken from Ref. [4].

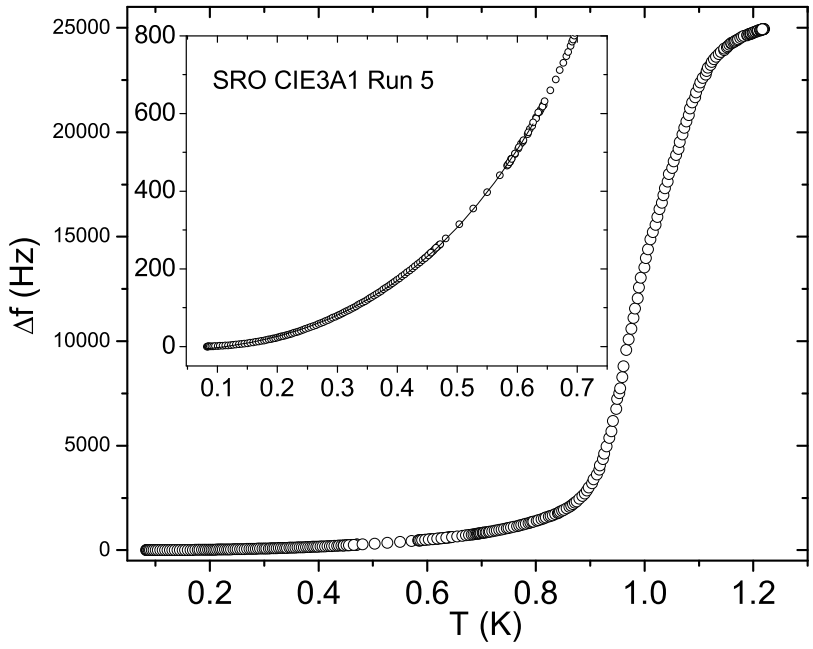

Figure 9.7: $\Delta f(T)$ vs T for SRO sample with $T_c \approx 1$ K. Inset shows the low-temperature region. Solid line is a fit to Eqn. 9.6 from 82 mK to 0.63 K.

condition $\xi > \lambda$ in the purest samples. So even in slightly dirtier samples, the nonlocal condition can still be satisfied, albeit in smaller parts of the FS closer to the nodes. There is at present no conclusive explanation for this T^3 behavior. In this thesis, we present additional data on one dirty sample of Sr_2RuO_4 with $T_c \approx 1$ K. We attempt to explain the temperature dependence of these samples using the nonlocal calculation of KS [5]. Our conclusion is that the effective single band theory is able to explain the T^3-dependence of dirty samples, but not the T^2-dependence of pure samples. We also propose an alternative method to explain the data of both pure and dirty samples within the same two-band framework.

First we consider the one-band model. As we go across the samples with different T_c's, the magnitude of the smaller gap, $\Delta_2(0)$ depends only on T_c. We assume that the prefactors 1/18 and 83/3240 in Eqn. 9.6, to a first approximation, do not change with the purity of the sample. We also assume $\Delta_2(0) = \Delta_{BCS}(0) = 1.76T_c$. So $T_p = \Delta_2(0)/\pi = 0.56T_c$. Using these values of T_p for different values of T_c, we can calculate the relative contributions of the

Sample T_c(K)	$\Delta_2(0)$=1.76T_c (K)	T_p=$\Delta_2(0)/\pi$ (K)	b/c theory	b/c data
0.82	1.44	0.46	0.46	0.3
1.0	1.76	0.56	0.68	0.6
1.5	2.64	0.84	1.53	10

Table 9.2: Value of b/c obtained from data and KS one-band model. b/c is the contribution of T^2 term relative to the T^4 term, to $\Delta\lambda(T)$ or $\Delta f(T)$.

T^2 and T^4 terms in Eqn. 9.6. We clearly see that as the sample gets dirtier, T_p gets smaller, and the relative contribution of the T^4 term increases. Fig. 9.7 shows $\Delta f(T)$ for a sample whose $T_c \approx 1$ K. As with the earlier dirty sample ($T_c = 0.82$ K), we obtain a T^3-fit from 120 mK to $0.5T_c$. Next, we fit the experimental data to the equation $\Delta f(T) = \mathrm{a} + bT^2 + cT^4$. The relative contribution of the T^2-term relative to the T^4-term is then b/c. Table 9.2 compares the predicted and experimental values of b/c, together with the values of T_c, $\Delta(0)$ and T_p for the different samples. We see that for the the dirty samples, the values of b/c predicted by the one-band model roughly agree with data. But for the purest sample, the experimental T^2-dependence ($b/c \approx 10$) is much stronger than the predicted one ($b/c \approx 1.5$).

The above analysis suggests that for dirty samples, there is effectively only *one* superconducting gap whose amplitude is close to the BCS value, whereas for pure samples, a one-gap description is insufficient to explain the data. This agrees with KS, who stated that for strong interband coupling, all gaps are tied together and act like a superconductor with a single order parameter [5].

However, Mazin [149] pointed out that the merging of two gaps to one in the presence of moderate-to-strong interband impurity scattering takes place only *if* the order parameter has a *non-zero* average over the FS in the clean limit, for example, in s-wave superconductors. If the FS-average of the order parameter is zero, as is the case for d- or p- superconductors, then the gap suppression follows the Abrikosov-Gorkov theory all the way, with a possible gapless superconductivity just before superconductivity is totally suppressed. Golubov and Mazin [150] examined the effect of magnetic and nonmagnetic impurities on *multi-band* superconductors. Recall that for single-band superconductors, the Anderson theorem states

that non-magnetic impurities do not influence T_c. In the multi-band case, however, only *intra*band non-magnetic scattering does not influence T_c, i.e. besides magnetic impurities, *inter*band *non*-magnetic impurity scattering also suppresses T_c. Our dirty Sr_2RuO_4 samples contain Al as the (non-magnetic) impurity to suppress T_c. In the two-band case, weak-scattering limit ($\gamma_{\alpha\beta} \ll T_c$) assuming there are no magnetic impurities, we have the two-band Abrikosov-Gorkov relation [150]

$$\frac{T_{c0} - T_c}{T_c} = \frac{\pi \left[\Delta_1^2 \gamma_{12} - \Delta_1 \Delta_2 (\gamma_{12} + \gamma_{21}) + \Delta_2^2 \gamma_{21}\right]}{8 T_c (\Delta_1^2 + \Delta_2^2)}, \tag{9.7}$$

where T_{c0} is the superconducting transition temperature of the purest sample (≈ 1.5 K), and γ_{ij} is the non-magnetic impurity scattering rate from band i to band j. Thus we could use Eqn. 9.7 to obtain γ_{12} (assuming $\gamma_{12} = \gamma_{21}$) for each of our dirty samples. Then we use γ_{12} to calculate how much the gaps Δ_1 and Δ_2 in the active and passive bands are suppressed. Finally, armed with the temperature dependence of the two suppressed gaps, we perform the same calculations as in the pure case to obtain the temperature dependence of the superfluid density, or penetration depth. The above will be the object of future theoretical work.

9.4 Conclusion

Previous data taken by Bonalde *et al.* on pure Sr_2RuO_4 samples [4] were reanalyzed by Kusunose and Sigrist's [5]. It is found that a one-band nonlocal model is not able to explain the approximate T^2-behavior over a wide temperature range as seen in penetration depth data. A two-band model is thus required, with the active band being fully gapped, and the passive band having horizontal line nodes. The same set of intraband and interband coupling parameters can explain both the penetration depth and heat capacity data. However, a two-band model with a fully-gapped passive band is also able to explain the penetration depth data. Kusunose and Sigrist did not attempt to use the model to explain the T^3 low-temperature dependence of dirty samples. We ran two additional samples, one with

$T_c \approx 1.5$ K (pure) and the other with $T_c \approx 1$ K (dirty). We confirmed the T^2 and T^3 low-temperature dependence of the pure and dirty sample, respectively. We propose that Kusunose and Sigrist's *one*-band model is able to explain T^3-dependence of dirty samples, suggesting that for dirty samples, there is effectively only one superconducting gap. The one-band model is not able to explain the T^2-dependence of pure samples. We also present an alternative explanation by Golubov and Martin [150] which examined the effects of impurites on multi-band superconductors, and suggest that the two gaps in Sr_2RuO_4 are suppressed by impurities following the two-band Abrikosov-Gorkov relation [150]. One then can use the same intraband and interband expressions of the momentum-dependent pairing interactions as in the pure case to calculate the temperature dependence of the penetration depth in dirty samples. This will be the object of future theoretical work.

Experimentally, we also hope to run more samples with different T_c's ranging from 0.7 K to 1.4 K. I wish to thank Professors Igor Mazin and Hiraoki Kusunose for enlightening discussions. I also thank Professor Y. Maeno for providing the samples.

When this thesis was almost completed a paper appeared in the Los Alamos archives [151], which described the measurement of the in-plane field-angle-dependent heat capacity of Sr_2RuO_4 down to 0.1 K. The data revealed that the SC state of Sr_2RuO_4 has a band-dependent gap, and the gap on the active band has strong in-plane anisotropy with a minimum along the [100] direction. The conclusions are still controversial at this moment.

Chapter 10

Pb: Effect of spin-density order on superconductivity

10.1 Introduction

Lead (Pb) is a conventional superconductor with not-so-conventional properties. Tunneling measurements gave an estimate of the zero-temperature gap $\Delta_0 = 1.35$ meV $\approx 2.2T_c$ [152], suggesting that Pb is a strong-coupling superconductor. Specific-heat measurements [153] reveal that the electronic part of the specific heat, C_{es}, at 0.5 K is four orders of magnitude larger than that predicted by BCS theory. Moreover, impurites eliminate the large anomaly. Ultrasonic attenuation experiments also indicate a much larger concentration of quasiparticles than that predicted from the value of Δ_0.

All the above data suggest a high number of quasiparticles. In particular, the specific-heat data [153] imply the presence of regions of a reduced energy gap of about $\Delta_0/4$. Theoretical work which incorporates the strong-coupling nature of Pb, however, predicts only a less than 10% gap anisotropy [154].

Overhauser and Daemen [6, 155] proposed a remarkable answer to this puzzle: the electronic ground state of Pb possesses a spin density wave (SDW) structure, which is not included in the BCS and strong-coupling calculations. This SDW interferes with Cooper pairing, such that the superconducting gap is reduced at the intersection of SDW planes and

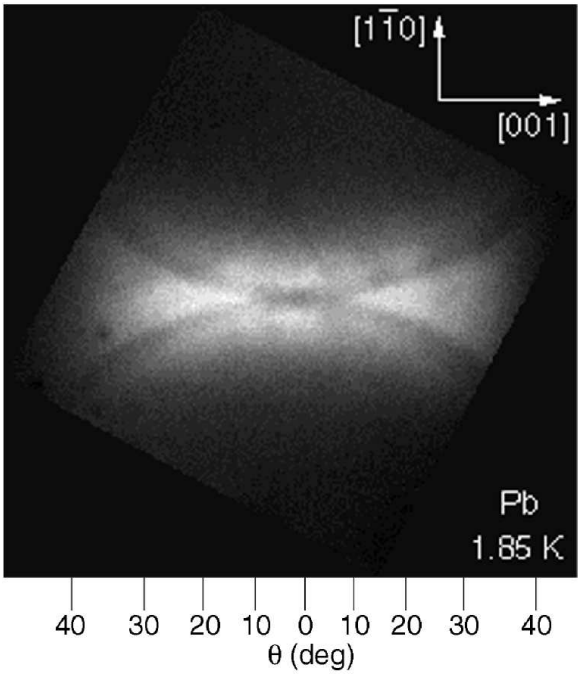

Figure 10.1: Phonon image in Pb at 1.85 K. Taken from Ref. [7].

the Fermi surface (FS). This leads to a large anisotropy in the superconducting gap, and explains the anomalous temperature dependencies of the specific heat and acoustic attenuation. Chen and Overhauser [156] further showed that such an electronic ground state would lead to a highly anomalous phonon dispersion in Pb.

Short and Wolfe [7] performed phonon imaging experiments on superconducting Pb. Fig. 10.1 shows the phonon image in Pb at 1.85 K. The striking result in the figure is the pattern of dark lines crossing in the [110] direction. These lines correspond to absorption of sub-gap phonons with wavevectors in the {111} planes. They postulated that the phonon absorption is due to phonon-quasiparticle scattering. By plotting the amount of absorption at different temperatures (1.4 K–2 K) and fitting it to the BCS expression (Fig. 10.2), they found that the best fit occurs when the gap parameter $\Delta_{fit} = \Delta_0/6$. However, the small temperature range of the data cannot distinguish between an exponential (implying $\Delta_{fit} > 0$) and polynomial dependence (implying $\Delta_{fit} = 0$). The temperature dependence is thus much slower than expected, and is consistent with the slow temperature-dependence of specific

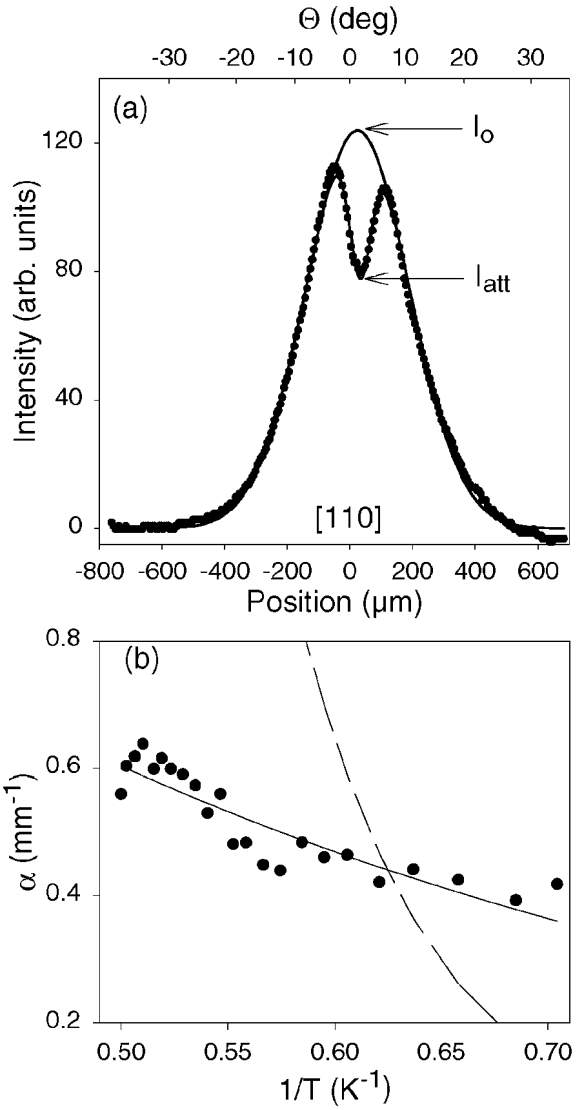

Figure 10.2: (a) Solid dots are the measured phonon flux along a vertical line through the center of the phonon image in Fig. 10.1. The unattenuated flux is approximated with a Gaussian function of amplitude I_0. The thin line through the data points is a fit to a Gaussian-exponential function in Ref. [7]. (b) Temperature dependence of the phonon attenuation coefficient along [110]. The solid line shows an exponential fit using an energy gap of $\Delta_0/6$ and the dashed lines uses Δ_0 with an arbitrary vertical displacement. Taken from Ref. [7].

heat and ultrasonic attenuation data. The energy of the absorbed phonons implies that the their wavevector lies in the {111} planes.

Daemen and Overhauser [155] pointed out that for Pb the candidate SDW wavevectors are $\mathbf{Q} = (2\pi/a)[211]$ or $(2\pi/a)[210]$. In the spherical FS approximation, the intersection of the $(2\pi/a)[211]$ planes with the FS of Pb are circles, while Short and Wolfe calculated and obtained [7], using de Haas-van Alphen data [158] for Pb, a triangular-shaped intersection of the $(2\pi/a)[211]$ planes with the *actual* FS of Pb. Three types of quasiparticle-scattering are possible: (1) intravalley scattering, (2) inter-valley scattering and (3) exit-valley scattering. The schematic of these types of scattering processes is shown in Fig. 10.3. Phonons with energy less than Δ_0 are restricted to scattering a quasiparticle from one part of the node structure to a nearby portion of the node structure — processes shown in Fig. 10.3a and referred to collectively as "in-valley" — as the phonon has insufficient energy to eject the quasiparticle from the valley. If there are intersecting valleys, we distinguish between inter-valley and intra-valley scattering events as illustrated in the figure. By comparing theoretical calculations with data, Short and Wolfe [7] concluded that the transitions responsible for the absorption lines are the inter-valley transitions.

In a later paper, however, Short and Wolfe [157] suggested two corrections to their previous hypothesis. First, the previous model did not account for mass-defect (or isotope) scattering resulting from the random occurrence of atomic isotopes in a crystal. After taking isotope-scattering into account and fitting it to data, they obtained $\Delta_{min} = \Delta_0/3.5$, which agrees even better with specific heat data [153]. Second, the phase space for in-valley scattering is too small to explain the observed absorption. They then proposed that "exit-valley" transitions (Fig. 10.3b), mediated by phonons whose energies exceed Δ_0, are more likely the dominant scattering mechanism. They then proposed a new experiment, where only low-energy "in-valley" phonons ($h\nu < \Delta_0 - \Delta_{min}$) are used to mediate in-valley transitions, so that one can ascertain gap minima directions. The proposed experiment is still underway, carried out by Tim Head from Professor Jim Wolfe's group.

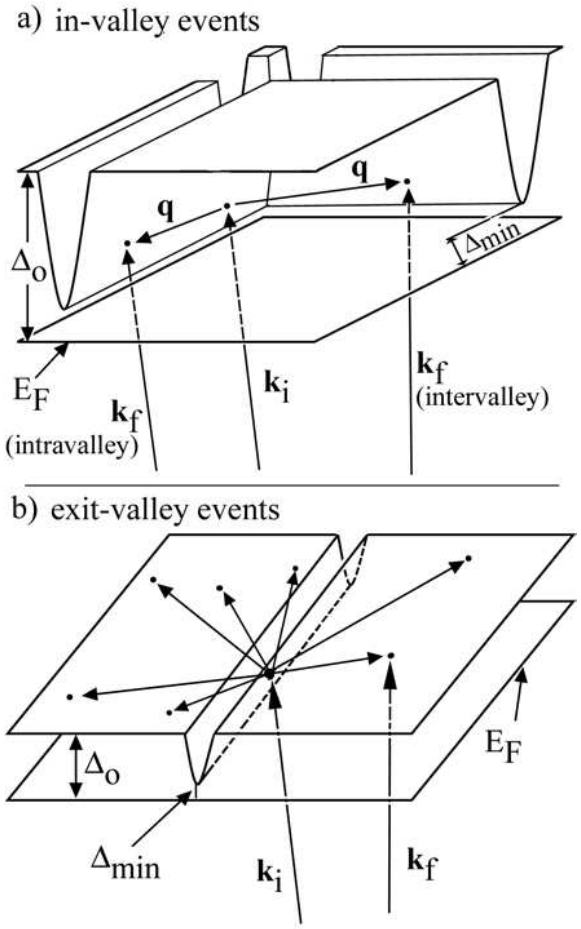

Figure 10.3: Diagram of (hypothetical) sharp gap anistropy in the superconducting energy gap. The bottom of the "valleys" correspond to a minimum gap value of Δ_{min} with the full gap value Δ_0 on the rest of the FS. (a) Definition of "in-valley" phonon scattering. (b) Definition of "exit-valley" scattering. In-valley phonons (a) scatter quasiparticles within the gap valleys as shown and exit-valley phonons (b) scatter a quasiparticle from within a valley to a final state anywhere on the FS. Taken from Ref. [157].

A proposed experiment to indirectly support the SDW theory is to take penetration depth data for two Pb single-crystal cylinders cut in two different orientations. One has the cylindrical axis pointing in the [111]-direction, and the other in the [110]-direction. In general if there exists nodes in a certain direction in **k**-space, then applying a field *perpendicular* to that direction in real space probes the quasiparticles excited along that direction in **k**-space. In our setup the ac field is always applied parallel to the cylindrical axis. Since the proposed nodal regions are close to the (111)-plane, we should see a greater departure from BCS dependence if the field is applied perpendicular to the [110] direction compared with [111] direction. What is uncertain is whether the departure from BCS theory is observable.

10.2 Data and Analysis

We measured the penetration depth of two samples of different crystal orientations. Pb#1 (or Pb(111)) is a cylindrical sample of diameter 1.4 mm and length 0.23 mm, and the cylindrical axis points in the [111] direction, i.e. its cross-sectional area is the (111) plane. Pb#2 (or Pb(110)) is also a cylinder, with diameter 1.3 mm and length 0.8 mm, but its cylindrical axis points in the [110] direction. The samples are 99.9999% pure Pb grown by Metal Crystals & Oxides, Ltd., United Kingdom. The ac field is applied along the cylindrical axis.

Fig. 10.4 shows the temperature dependence of the change in penetration depth, $\Delta\lambda(T) = \lambda(T) - \lambda(0.1\text{ K})$ of Pb#1. The insert shows the low-temperature region in detail. Below 1.1 K, there is a clear downturn, before another upturn appears near 0.6 K. This signal is obtained after subtraction of the background signal from the sapphire sample holder. Initially we thought that this upturn is due to the sample holder, but later measurements on the Pb#2 sample did not reveal an upturn of such magnitude. This upturn may be due to the presence of very small amount of paramagnetic impurities inside the sample. We have ordered another Pb(111) sample, and will run it to confirm this feature.

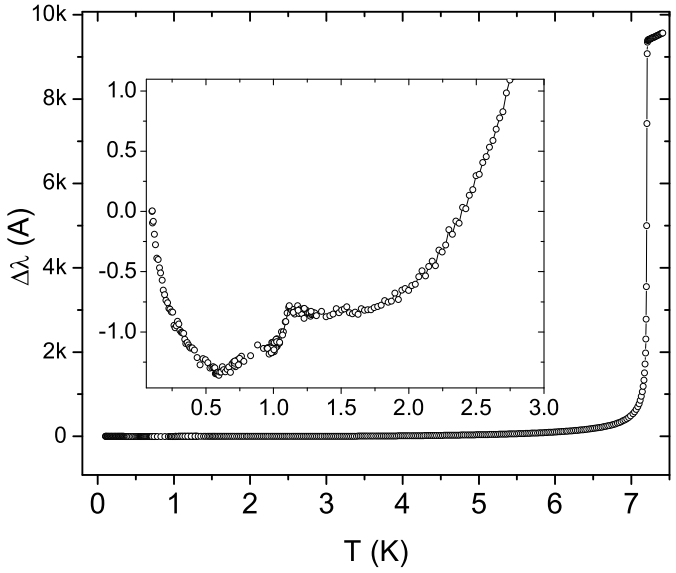

Figure 10.4: $\Delta\lambda(T)$ for Pb#1. Inset shows low-temperature region.

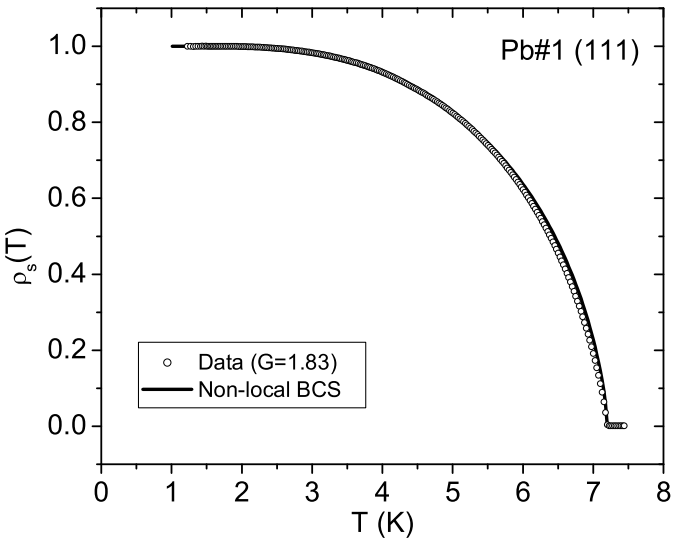

Figure 10.5: Superfluid density $\rho_s(T)$ for Pb#1. (◯) Data, using G = 1.83. (Solid line) Nonlocal BCS superfluid density expression.

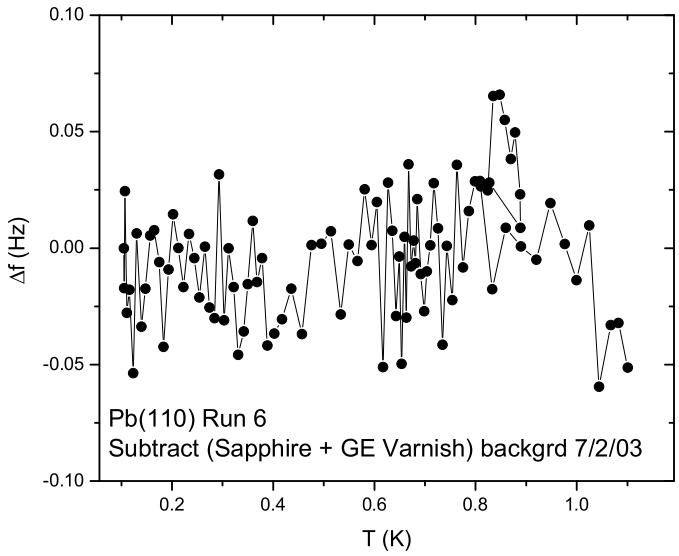

Figure 10.6: $\Delta f(T)$ vs T for Pb#2 below 1 K. Within errors due to noise and background, the signal is essentially zero.

We now turn to the high-temperature region (1 K $< T < T_c$). First we convert $\Delta\lambda(T)$ to superfluid density ρ_s. Fig. 10.5 shows $\rho_s(T)$ from 1.1 K to T_c. We have assumed $\lambda(0.1\text{ K}) = 0$, and $\lambda(0) = 390$ Å. The circles are the data points, where we have used the calibration factor G = 1.83, obtained from the calibration method described in Section 3.5. The solid line is the BCS superfluid density expression in the pure nonlocal limit, given by Eqn. 3.39, where we have used $T_c = 7.19$ K, $\Delta_0/k_BT_c = 2.15$, and the specific heat jump $\Delta C/C = 2.71$ from Ref. [159]. The agreement between data and theory is quite remarkable, and is another confirmation that our calibration method is accurate.

Fig. 10.6 shows the low-temperature $\Delta f(T)$ for sample Pb#2. The low-temperature signal is basically flat, suggesting that at this temperature range ($T \leq 0.14\ T_c$), all the quasiparticles have been frozen out. Fig. 10.7 shows $\Delta f(T)$ from 0.1 K to 3.6 K ($\sim 0.5\ T_c$). The solid line is the fit of the data to the low-temperature local limit

$$\Delta f = constant \times \sqrt{\frac{\pi\Delta(0)}{2T}} exp\left(-\frac{\Delta(0)}{k_BT}\right), \tag{10.1}$$

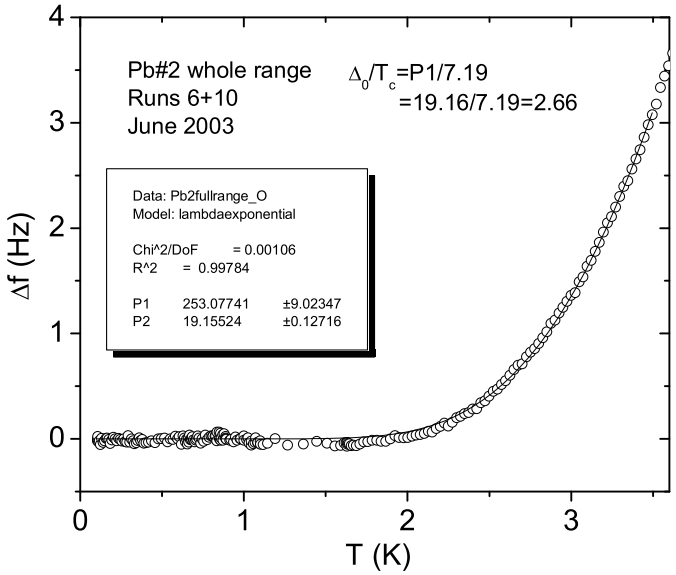

Figure 10.7: $\Delta f(T)$ vs T for Pb#2 below 3.6 K. Solid line is the low-temperature BCS fit.

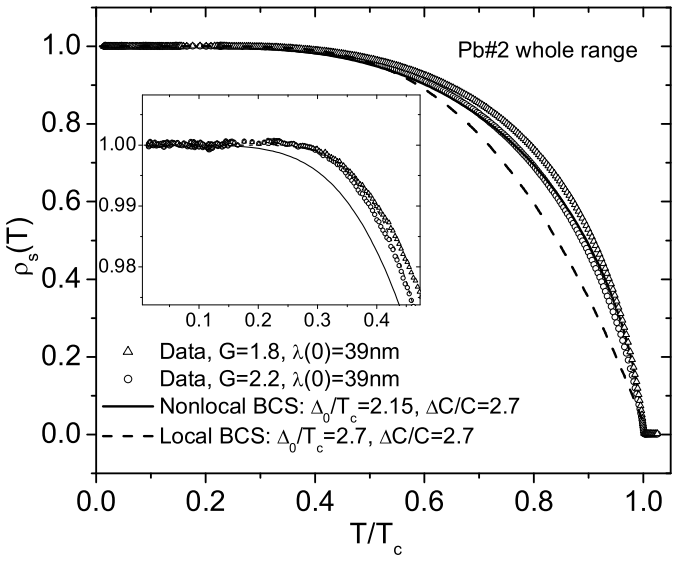

Figure 10.8: $\rho_s(T)$ of Pb#2. (◯) Data using G = 1.8. (△) Data using G = 2.2. (Solid line) BCS nonlocal limit. (Dashed line) BCS local limit. Inset shows the low-temperature region in detail.

where $\Delta(0)$ is the zero-temperature gap. For the best fit we obtain $\Delta(0) = 19.2$ K, which implies $\Delta(0)/T_c = 19.2/7.19 = 2.66$. This is larger than the value of 2.15 obtained from other measurements [159]. Note that this value of the gap does *not* depend on the value of the calibration constant G. Fig. 10.8 shows $\rho_s(T)$ from 0.1 K to T_c. The circles are the data points using $G = 1.8$, and the solid line is the BCS expression for ρ_s in the pure *nonlocal* limit. This time the agreement between data and theory is unsatisfactory. To have them agree requires $G \approx 2.2$ ($\triangle$). This is about 20% larger than the calculated value, but is still smaller than the "infinite-slab" value of 2.6. This discrepancy may be due to the comparatively smaller aspect ratio of sample Pb#2, which we explained in Section 3.5. Also in the same figure is the BCS expression for ρ_s in the pure *local* limit (dashed line). From the figure and its inset, we see that the nonlocal expression fits the $G = 2.2$ data better for the entire temperature range, while the local expression fits the low-T region better, though with a larger value of $\Delta(0)/T_c$ (2.66). Our BCS expressions are valid for the extreme local or nonlocal limit, while in Pb, $\lambda/\xi = 0.48$ [159], implying that Pb is only a moderately nonlocal superconductor. This might be the reason for the discrepancy between data and fits.

If we assume that the total change in penetration depth from the two orientations are equal, it is then instructional to normalize both sets of data to the same total change in frequency, say 10 kHz, and plot them on the same graph. Fig. 10.9 shows $\Delta f(T)$ normalized to 10 kHz vs T for Pb#1 and Pb#2 samples. Inset shows the low-temperature region — the curves have been offset by 0.5 Hz for clarity. Above 1 K it seems that the temperature dependence of both signals are identical, i.e. we cannot see any qualitative or quantitative difference between the two samples, but we can't be entirely sure about this.

10.3 Conclusion

We therefore cannot say anything conclusive about both samples: Pb#1 may have some impurities in it, while Pb#2 is too thick for the calibration method to work nicely. We have

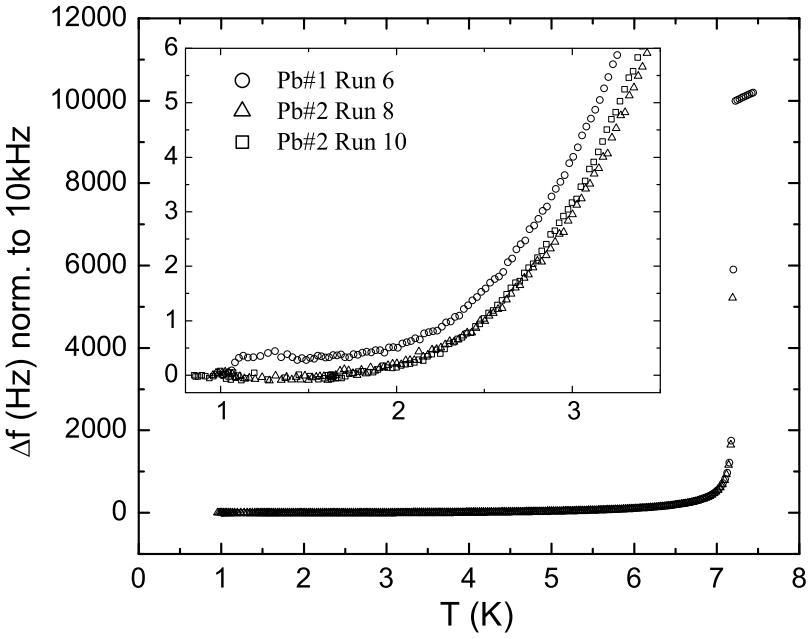

Figure 10.9: $\Delta f(T)$ normalized to 10 kHz for Pb#1 and Pb#2 samples. Inset shows low-temperature region — the curves have been offset by 0.5 Hz for clarity.

already ordered two samples of exactly identical dimensions, of large aspect ratios (i.e. thin samples), one each of (111) and (110) orientation. Having identical dimensions will allow us to directly compare the raw $\Delta f(T)$ data from these two samples, thereby eliminating the need to calculate G. Of course if we want to convert to ρ_s we still need G, but at least G, being a purely geometrical factor, will be the same for both samples.

I wish to thank Professor Jim Wolfe, Jonathan Short, and Tim Head for enlightening discussions about ballistic phonon experiments in Pb.

Chapter 11

Concluding Remarks

In this thesis we present measurements of the temperature-dependence of the penetration depth of a number of unconventional superconductors. We see that penetration depth is a very direct way of probing the symmetry of the order parameter of the superconducting gap. We can deduce, if the temperature-dependence is exponential (or power-law), that the superconducting gap is fully-gapped (or has nodes) on the Fermi surface. We also see how different types of magnetic order influences superconductivity, by suppressing it, destroying it, or having negligible effect on it.

In the heavy-fermion superconductor $CeCoIn_5$ ($T_c = 2.3$ K), we obtain a $T^{3/2}$ dependence, which we take to be a crossover from T to T^2. Two models could explain this crossover — Hirschfeld and Goldenfeld's Resonant Impurity Scattering (RIS) [18] and Kosztin and Leggett's nonlocal theory [20], both for d-wave superconductors. By calculating the theoretical crossover temperature T^* in these two models, and comparing them with the experimental crossover temperature, it would seem at first sight that the nonlocal theory is a better model for explaining the crossover in this material. However the coefficients in the RIS theory are approximations [39]. Taking this into account, we therefore conclude that both impurity scattering and nonlocality are viable theories to explain the crossover effect, and it is not clear which is better.

In another heavy-fermion superconductor $PrOs_4Sb_{12}$ ($T_c = 1.8$ K), we measured the penetration depth when the probing field is in each of the three crystallographic axes, and found

that in all three cases $\lambda \sim T^2$ at low temperatures. We examined four candidate gap functions, calculated their quasiparticle density of states and superfluid densities, and concluded that the superconducting gap in this material has two point nodes on the fermi surface, and the gap dispersion is similar to that of the A-phase of superfluid ^{3}He. We also come to an interesting conclusion that this material has multi-domains — a consequence of the field-direction-independence of the superfluid density *and* the good fit of the experimental superfluid density and the calculated superfluid density averaged across three crystallographic directions.

We next measured $\Delta\lambda$ of the non-magnetic members of the borocarbide family, YNi_2B_2C ($T_c = 15.9$ K) and $LuNi_2B_2C$ ($T_c = 15.5$ K). We found an additional downturn below 1 K, and concluded that this downturn must be due to extrinsic effects like surface flux or surface oxide layer. We tried to apply Suhl's two-band model [90] to fit the superfluid density, but found that a very large gap opens up on the band with a very small density of states, contradicting de Haas-van Alphen data. We also tried to apply Maki's pure and dirty $s + g$ model [93] to explain our data.

The magnetic member of the borocarbide family, $ErNi_2B_2C$ ($T_c = 10.1$ K) has a superconducting transition temperature of 11 K. It exhibits an antiferromagnetic spin-density-wave phase below 6 K, and a weak ferromagnetic component appears below 2.3 K. We found that the antiferromagnetic phase has negligible effect on the superconductivity, whereas the weak ferromagnetic component slightly depresses, but does not completely destroy, superconductivity. We used Chi and Nagi's model [115] to calculate the superfluid density in the paramagnetic ($T_N < T < T_c$) and antiferromagnetic ($T < T_N$) phase, as well as extending it to include the weak ferromagnetic phase below 2.3 K. We find good fit between theory and experiment. We also suggest an alternative explanation, that the increased pair-breaking due to partial nesting on one FS sheet in $ErNi_2B_2C$ is compensated by decreased pair-breaking by the other two sheets, resulting in negligible change in pair-breaking at T_N.

The other magnetic member, $HoNi_2B_2C$ ($T_c = 8$ K) show three types of magnetic order in the Ho f electron sublattice [97]: (a) a commensurate antiferromagnetic structure below

5 K, which consists of sheets of ferromagnetic moments in the $a-b$ plane, with adjacent sheets coupled antiferromagnetically along the c-axis; (b) an incommensurate c-axis helical magnetic state at ≈ 8.5 K; (c) another incommensurate a-axis modulation at ≈ 6.3 K. Our data reveal a coexistence of these three types of magnetic order and superconductivity. The c-axis helical phase slightly suppresses, but does not completely destroy, superconductivity.

Penetration depth measurements on a *pure* spin-triplet superconductor Sr_2RuO_4 ($T_c = 1.5$ K), shows an approximate T^2-behavior at low temperatures. Its Fermi surface consists of an active γ-band that is fully-gapped, and passive α or β bands (treated as one band) with horizontal line nodes. A one-band picture, even in the Pippard limit, is unable to explain the T_2-behavior over a large temperature range as seen in penetration depth data. Kusunose and Sigrist [5] proposed a two-band model to explain this temperature-dependence. The same set of intraband and interband coupling parameters is able to explain both penetration depth and heat capacity data. However, Kusunose and Sigrist did not attempt to use the model to explain the low-temperature T^3-behavior of *dirty* samples, as seen in two of our samples with T_c's of 0.82 K and 1 K. We ran two additional samples, one with $T_c \approx 1.5$ K (pure) and the other with $T_c \approx 1$ K (dirty). We confirmed the T^2 and T^3 low-temperature dependence of the pure and dirty sample, respectively. We propose that Kusunose and Sigrist's *one*-band model is able to explain T^3-dependence of dirty samples, suggesting that for dirty samples, there is effectively only one superconducting gap. The one-band model is not able to explain the T^2-dependence of pure samples. We also present an alternative explanation by Golubov and Martin [150] which examined the effects of impurites on multi-band superconductors, and suggest that the two gaps in Sr_2RuO_4 are suppressed by impurities following the two-band Abrikosov-Gorkov relation [150]. One then can use the same intraband and interband expressions of the momentum-dependent pairing interactions as in the pure case to calculate the temperature dependence of the penetration depth in dirty samples. This will be the object of future theoretical work.

Finally, we look at the "conventional" BCS superconductor, Pb. Overhauser [6] proposed that the electronic ground state of Pb possesses a spin density wave (SDW) structure. This SDW interferes with Cooper pairing, such that the superconducting gap is reduced at the intersection of SDW planes and the Fermi surface. This leads to a large anisotropy in the superconducting gap, and explains the anomalous temperature dependencies of the specific heat, acoustic attenuation, and phonon imaging experiments. We measured the penetration depth of two Pb cylinders with cylindrical axis pointing in the [111]-, and [110]-, directions, but with different diameters and thicknesses, and hope to see a difference in the temperature dependence of λ. Unfortunately we cannot see any qualitative or quantitative difference between the two samples, within experimental uncertainty. We plan to repeat the measurements on two more cylindrical samples of exactly the same dimensions, so that one can eliminate errors due to calibration.

References

[1] H. K. Onnes. *Commun. Phys. Lab. Univ. Leiden*, page No 124c, 1911.

[2] J. Bardeen, L. N. Cooper, and J. R. Schrieffer. *Phys. Rev.*, 108:1175, 1957.

[3] M. K. Wu, J. R. Ashburn, C. J. Torng, P. H. Hor, R. L. Meng, L. Gao, Z. J. Huang, Y. Q. Wang, and C. W. Chu. *Phys. Rev. Lett.*, 58:908, 1987.

[4] I. Bonalde, Brian D. Yanoff, M. B. Salamon, D. J. Van Harlingen, E. M. E. Chia, Z. Q. Mao, and Y. Maeno. *Phys. Rev. Lett.*, 85:4775, 2000.

[5] H. Kusunose and M. Sigrist. *Europhys. Lett.*, 60:281, 2002.

[6] A. W. Overhauser and L. L. Daemen. *Phys. Rev. Lett.*, 61:1885, 1988.

[7] J. D. Short and J. P. Wolfe. *Phys. Rev. Lett.*, 85:5198, 2000.

[8] I. Kosztin. *Topics in Theory of Superconductivity.* PhD thesis, University of Illinois at Urbana-Champaign, 1997.

[9] F. Gross, B. S. Chandrasekhar, D. Einzel, K. Andres, P. J. Hirschfeld, H. R. Ott, J. Beuers, Z. Fisk, and J. L. Smith. *Z. Phys. B*, 64:175, 1986.

[10] J. F. Annett, Nigel Goldenfeld, and S. R. Renn. *Physical Properties of High-Temperature Superconductors*, volume II, chapter 8, pages 573–685. World Scientific, Singapore.

[11] V. P. Mineev and K. V. Samokhin. *Introduction to Unconventional Superconductivity.* Gordon and Breach Science Publishers, 1999.

[12] A. Leggett. *Rev. Mod. Phys.*, 47:331, 1975.

[13] V. V. Schmidt. *The Physics of Superconductors.* Springer, 1997.

[14] M. Tinkham. *Introduction to Superconductivity.* McGraw-Hill, Inc., New York, 2nd edition, 1996.

[15] G. R. Stewart. *Rev. Mod. Phys.*, 56:755, 1984.

[16] D. Xu, S. K. Yip, and J. A. Sauls. *Phys. Rev. B*, 51:16233, 1995.

[17] J. Annett, N. Goldenfeld, and S. R. Renn. *Phys. Rev. B*, 43:2778, 1991.

[18] Peter J. Hirschfeld and Nigel Goldenfeld. *Phys. Rev. B*, 48:4219, 1993.

[19] W. N. Hardy, D. A. Bonn, D. C. Morgan, Ruixing Liang, and Kuan Zhang. *Phys. Rev. Lett.*, 70:3999, 1993.

[20] Ioan Kosztin and Anthony J. Leggett. *Phys. Rev. Lett.*, 79:135, 1997.

[21] A. A. Abrikosov. *Fundamentals of the Theory of Metals.* Elsevier Science Pub. Co., Amsterdam, New York: NorthHolland, 1988.

[22] C. T. Van Degrift. *Rev. Sci. Instrum.*, 46:599, 1975.

[23] B. D. Yanoff. *Temperature Dependence of the Penetration Depth in the Unconventional Superconductor* Sr_2RuO_4. PhD thesis, University of Illinois at Urbana-Champaign, 2000.

[24] Woo F. Chow. *Principles of Tunnel Diode Circuits.* John Wiley & Sons, Inc., 1964.

[25] S. G. Gevorgyan, G. D. Movsesyan, A. A. Movsisyan, and V. T. Tatoyan. *Rev. Sci. Instrum.*, 69:2550, 1998.

[26] V. G. Welsby. *The Theory and Design of Inductance Coils.* MacDonald & Co. (Publishers) Ltd., 1950.

[27] F. Habbal, G. E. Watson, and P. R. Elliston. *Rev. Sci. Instrum.*, 46:192, 1975.

[28] J. D. Jackson. *Classical Electrodynamics*. John Wiley & Sons, Inc., 3rd edition, 1998.

[29] R. Prozorov, R. W. Gianetta, A. Carrington, and F. M. Araujo-Moreira. *Phys. Rev. B*, 62:115, 2000.

[30] D. Shoenberg. *Superconductivity*. Cambridge University Press, 2nd edition, 1962.

[31] C. Petrovic, P. G. Pagliuso, M. F. Hundley, R. Movshovich, J. L. Sarrao, J. D. Thompson, Z. Fisk, and P. Monthoux. *J. Phys.: Condens. Matter*, 13:L337, 2001.

[32] Donavan Hall, E. Palm, T. Murphy, Z. Fisk, U. Alver, R. G. Goodrich, J. L. Sarrao, P. G. Pagliuso, and Takao Ebihra. *Phys. Rev. B*, 64:212508, 2001.

[33] S. Ikeda, H. Shishido, M. Nakashima, R. Settai, D. Aoki, Y. Haga, H. Harima, Y. Aoki, T. Namiki, H. Sato, and Y. Ōnuki. *J. Phys. Soc. Jpn.*, 70:2248, 2001.

[34] Rodrigo J. Ormeno, A. Sibley, Colin E. Gough, S. Sebastian, and I. R. Fisher. *Phys. Rev. Lett.*, 88:047005, 2002.

[35] R. Movshovich, M. Jaime, J. D. Thompson, C. Petrovic, Z. Fisk, P. G. Pagliuso, and J. L. Sarrao. *Phys. Rev. Lett.*, 86:5152, 2001.

[36] K. Izawa, H. Yamaguchi, Yuji Matsuda, H. Shishido, R. Settai, and Y. Onuki. *Phys. Rev. Lett.*, 87:057002, 2001.

[37] Y. Kohori, Y. Yamato, Y. Iwamoto, T. Kohara, E. D. Bauer, M. B. Maple, and J. L. Sarrao. *Phys. Rev. B*, 64:134526, 2001.

[38] N. J. Curro, B. Simovic, P. C. Hammel, P. G. Pagliuso, J. L. Sarrao, J. D. Thompson, and G. B. Martins. *Phys. Rev. B*, 64:180514, 2001.

[39] Nigel Goldenfeld. *private conversation*.

[40] C. Petrovic, R. Movshovich, M. Jaime, P. G. Pagliuso, M. F. Hundley, J. L. Sarrao, Z. Fisk, and J. D. Thompson. *Europhys. Lett.*, 53:354, 2001.

[41] Ioan Kosztin, Qijin Chen, Boldizsar Janko, and K. Levin. *Phys. Rev. B*, 58:R5936, 1998.

[42] Qijin Chen, Ioan Kosztin, Boldizsar Janko, and K. Levin. *Phys. Rev. Lett.*, 81:4708, 1998.

[43] Qijin Chen, Ioan Kosztin, and K. Levin. *cond-mat/9908362*, 1999.

[44] V. A. Sidorov, M. Nicklas, P. G. Pagliuso, J. L. Sarrao, Y. Bang, A. V. Balatsky, and J. D. Thompson. *cond-mat/0202251*, 2002.

[45] A. Carrington, I. J. Bonalde, R. Prozorov, R. W. Giannetta, A. M. Kini, J. Schlueter, H. H. Wang, U. Geiser, and J. M. Williams. *Phys. Rev. Lett.*, 83:4172, 1999.

[46] Yu. S. Barash, M. S. Kalenkov, and J. Kurkijarvi. *Phys. Rev. B*, 62:6665, 2000.

[47] T. P. Orlando, Jr E. J. McNiff, S. Foner, and M. R. Beasley. *Phys. Rev. B*, 19:4545, 1979.

[48] V. Z. Kresin and V. P. Parkhomenko. *Sov. Phys.- Solid State*, 16:2180, 1975.

[49] A. Carrington, R. W. Giannetta, J. T. Kim, and J. Giapintzakis. *Phys. Rev. B*, 59:R14173, 1999.

[50] D. M. Broun, D. C. Morgan, R. J. Ormeno, S. F. Lee, A. W. Tyler, A. P. Mackenzie, and J. R. Waldram. *Phys. Rev. B*, 56:R11443, 1997.

[51] D. A. Bonn, S. Kamal, Kuan Zhang, Ruixing Liang, D. J. Baar, E. Klein, and W. N. Hardy. *Phys. Rev. B*, 50:4051, 1994.

[52] S. Özcan, D. M. Broun, B. Morgan, R. K. W. Haselwimmer, J. L. Sarrao, Saeid Kamal, C. P. Bidinosti, P. J. Turner, M. Raudsepp, and J. R. Waldram. *Europhys. Lett.*, 62:412, 2002.

[53] J. Wills. unpublished.

[54] E. D. Bauer, N. A. Frederick, P.-C. Ho, V. S. Zapf, and M. B. Maple. *Phys. Rev. B*, 65:100506 (R), 2002.

[55] M. B. Maple, P.-C. Ho, V. S. Zapf, N. A. Frederick, E. D. Bauer, W. M. Yuhasz, F. M. Woodward, and J. W. Lynn. *J. Phys. Soc. Jpn., Suppl. B*, 71:23, 2002.

[56] D. E. MacLaughlin, J. E. Sonier, R. H. Heffner, O. O. Bernal, Ben-Li Young, M. S. Rose, G. D. Morris, E. D. Bauer, T. D. Do, and M. B. Maple. *Phys. Rev. Lett.*, 89:157001, 2002.

[57] H. Suderow, S. Vieira, J. D. Strand, S. Bud'ko, and P. C. Canfield. *cond-mat/0306463*, 2003.

[58] H. Kotegawa, M. Yogi, Y. Imamura, Y. Kawasaki, G. q. Zheng, Y. Kitaoka, S. Ohsaki, H. Sugawara, Y. Aoki, and H. Sato. *Phys. Rev. Lett.*, 90:027001, 2003.

[59] Masanori Ichioka, Noriyuki Nakai, and Kazushige Machida. *cond-mat/0304538*, 2003.

[60] K. Izawa, Y. Nakajima, J. Goryo, Y. Matsuda, S. Osaki, H. Sugawara, H. Sato, P. Thalmeier, and K. Maki. *Phys. Rev. Lett.*, 90:117001, 2003.

[61] Y. Aoki, A. Tsuchiya, T. Kanayama, S. R. Saha, H. Sugawara, H. Sato, W. Higemoto, A. Koda, K. Ohishi, K. Nishiyama, and R. Kadono. *Phys. Rev. Lett.*, 91:067003, 2003.

[62] H. Sugawara, S. Osaki, S. R. Saha, Y. Aoki, H. Sato, Y. Inada, H. Shishido, R. Settai, Y. Onuki, H. Harima, and K. Oikawa. *Phys. Rev. B*, 66:220504, 2002.

[63] H. Sugawara. *private conversation.*

[64] M. Sigrist and K. Ueda. *Rev. Mod. Phys.*, 63:239, 1991.

[65] E. E. M. Chia, I. Bonalde, B. D. Yanoff, D. J. Van Harlingen, M. B. Salamon, and J. L. Sarrao. *Phys. Rev. B*, 67:014527, 2003.

[66] K. Maki, P. Thalmeier, Qungshan Yuan, K. Izawa, and Y. Matsuda. *cond-mat/0212090*, 2002.

[67] J. Goryo. *cond-mat/0212094*, 2002.

[68] R. Vollmer, A. Faiβt, C. Pfleiderer, H. v. Lohneysen, E. D. Bauer, P.-C. Ho, V. Zapf, and M. B. Maple. *Phys. Rev. Lett.*, 90:057001, 2003.

[69] E. Fawcett. *Rev. Mod. Phys.*, 60:209, 1988.

[70] S. A. Werner, A. Arrott, and H. Kendrick. *J. Appl. Phys.*, 37:1260, 1966.

[71] T. J. Bastow and R. Street. *Phys. Rev.*, 141:51, 1966.

[72] K. Machida. *private conversation.*

[73] P. C. Canfield, B. K. Cho, D. C. Johnston, D. K. Finnemore, and M. F. Hundley. *Physica C*, 230:397, 1994.

[74] H. Michor, T. Holubar, C. Dusek, and G. Hilscher. *Phys. Rev. B*, 52:16165, 1995.

[75] S. A. Carter, B. Batlogg, R. J. Cava, J.J. Krajewski, W. F. Peck Jr., and H. Takagi. *Phys. Rev. B*, 50:4216, 1994.

[76] L. F. Mattheiss. *Phys. Rev. B*, 49:R13 279, 1994.

[77] S. Manalo and E. Schachinger. *J. Low Temp. Phys.*, 123:149, 2001.

[78] K. Izawa, A. Shibata, Yuji Matsuda, Y. Kato, H. Takeya, K. Hirata, C. J. van der Beek, and M. Konczykowski. *Phys. Rev. Lett.*, 86:1327, 2001.

[79] N. Mangkorntong M. Nohara, H. Suzuki and H. Takagi. *Physica C*, 341-348:2177, 2000.

[80] T. Jacobs, Balam A. Willemsen, S. Sridhar, R. Nagarajan, L. C. Gupta, Z. Hossain, Chandran Mazumdar, P. C. Canfield, and B. K. Cho. *Phys. Rev. B*, 52:R7022, 1995.

[81] In-Sang Yang, M. V. Klein, S. L. Cooper, P. C. Canfield, B. K. Cho, and Sung-Ik Lee. *Phys. Rev. B*, 62:1291, 2000.

[82] T. Yokoya, T. Kiss, T. Watanabe, S. Shin, M. Nohara, H. Takagi, and T. Oguchi. *Phys. Rev. Lett.*, 85:4952, 2000.

[83] Etienne Boaknin, R. W. Hill, Cyril Proust, C. Lupien, and Louis Taillefer. *Phys. Rev. Lett.*, 87:237001, 2001.

[84] K. Izawa, K. Kamata, Y. Nakajima, Y. Matsuda, and T.Watanabe. *Phys. Rev. Lett.*, 89:137006, 2002.

[85] T. Park, M. B. Salamon, E. M. Choi, H. J. Kim, and S.-I. Lee. *Phys. Rev. Lett.*, 90:177001, 2003.

[86] D. J. Singh. *Solid State Commun.*, 98:899, 1996.

[87] G. Goll, M. Heinecke, A. G. M. Jansen, W. Joss, L. Nguyen, E. Steep, K. Winzer, and P. Wyder. *Phys. Rev. B*, 53:R8871, 1996.

[88] S. V. Shulga, S.-L. Drechsler, G. Fuchs, K.-H. Müller, K. Winzer, M. Heinecke, and K. Krug. *Phys. Rev. Lett.*, 80:1730, 1998.

[89] T. Terashima, C. Haworth, H. Takeya, S. Uji, H. Aoki, and K. Kadowaki. *Phys. Rev. B*, 56:5120, 1997.

[90] H. Suhl, B. T. Matthias, and L. R. Walker. *Phys. Rev. Lett.*, 3:552, 1959.

[91] Elbert E. M. Chia, I. Bonalde, Brian D. Yanoff, D. van Harlingen, M. B. Salamon, Sung-Ik Lee, and Heon Jung Kim. *J. Magn. Mag. Mat.*, 226-230:301, 2001.

[92] Qingshan Yuan, Hong-Yi Chen, H. Won, S. Lee, K. Maki, P. Thalmeiera, and C. S. Ting. *cond-mat/0306093*, 2003.

[93] Kazumi Maki, Hyekyung Won, and Stephan Haas. *cond-mat/0309688*, 2003.

[94] K. Maki. *private conversation.*

[95] K. D. D. Rathnayaka, A. K. Bhatnagar, A. Parasiris, D. G. Naugle, P. C. Canfield, and B. K. Cho. *Phys. Rev. B*, 55:8506, 1997.

[96] J. I. Lee, T. S. Zhao, I. G. Kim, B. I. Min, and S. J. Youn. *Phys. Rev. B*, 50:4030, 1994.

[97] J. W. Lynn, S. Skanthakumar, Q. Huang, S. K. Sinha, Z. Hossain, L. C. Gupta, R. Nagarajan, and C. Godart. *Phys. Rev. B*, 55:6584, 1997.

[98] Y. J. Tang, X. W. Cao, J. C. Ho, and H. C. Ku. *Phys. Rev. B*, 46:1213, 1992.

[99] V. Metlushko, U. Welp, A. Koshelev, I. Aranson, G. W. Crabtree, and P. C. Canfield. *Phys. Rev. Lett.*, 79:1738, 1997.

[100] M. E. Palistrant. *cond-mat/0305496*, 2003.

[101] T. Watanabe, K. Kitazawa, T. Hasegawa, Z. Hossain, R. Nagarajan, and L. C. Gupta. *J. Phys. Soc. Jpn.*, 69:2708, 2000.

[102] S.-M. Choi, J. W. Lynn, D. Lopez, P. L. Gammel, P. C. Canfield, and S. L. Bud'ko. *Phys. Rev. Lett.*, 87:107001, 2001.

[103] B. K. Cho, P. C. Canfield, D. C. Johnston, W. P. Beyermann, and A. Yatskar. *Phys. Rev. B*, 52:3684, 1995.

[104] J. Zarestky, C. Stassis, A. I. Goldman, P. C. Canfield, P. Dervenagas, B. K. Cho, and D. C. Johnson. *Phys. Rev. B*, 51:R678, 1995.

[105] P. C. Canfield, S. L. Bud'ko, and B. K. Cho. *Physica C*, 262:249, 1996.

[106] A. Andreone, C. Aruta, F. Fontana, M. Iavarone, M. L. Russo, and R. Vaglio. *J. Supercond.*, 11:707, 1998.

[107] P. L. Gammel, B. P. Barber, A. P. Ramirez, C. M. Varma, D. J. Bishop, P. C. Canfield, V. G. Kogan, M. R. Eskildsen, N. H. Andersen, and K. Mortensen. *Phys. Rev. Lett.*, 82:1756, 1999.

[108] A. Andreone, C. Aruta, M. Iavarone, F. Palomba, M. L. Russo, M. Salluzzo, R. Vaglio, A. Cassinese, M. A. Hein, T. Kaiser, G. Muller, and M. Perpeet. *Physica C*, 319:141, 1999.

[109] W. Baltensperger and S. Strassler. *Phys. Kondens. Materie*, 1:20, 1986.

[110] G. Zwicknagl and P. Fulde. *Z. Phys. B*, 43:23, 1981.

[111] Kazushige Machida, Kazuo Nokura, and Takeo Matsubara. *Phys. Rev. B*, 22:2307, 1980.

[112] T. V. Ramakrishnan and C. M. Varma. *Phys. Rev. B*, 24:137, 1981.

[113] M. J. Nass, K. Levin, and G. S. Grest. *Phys. Rev. Lett.*, 46:614, 1981.

[114] M. J. Nass, K. Levin, and G. S. Grest. *Phys. Rev. B*, 25:4541, 1982.

[115] Hongguang Chi and A. D. S. Nagi. *J. Low Temp. Phys.*, 86:139, 1992.

[116] A. Abrikosov and L. P. Gorkov. *Soviet Phys. - JETP*, 12:1243, 1961.

[117] Charles Ro and K. Levin. *Phys. Rev. B*, 29:6155, 1984.

[118] P. W. Anderson. *J. Phys. Chem. Solids*, 11:26, 1959.

[119] J. Zittartz. *Phys. Rev.*, 164:575, 1967.

[120] H. Takeya, T. Hirano, and K. Kadowaki. *Physica C*, 256:220, 1996.

[121] Tuson Park. unpublished.

[122] L. F. Rybaltchenko, I. K. Yanson, A. G. M. Jansen, P. Mandal, P. Wyder, C. V. Tomy, and D. McK. Paul. *Physica B*, 218:189, 1996.

[123] S. B. Dugdale, M. A. Alam, I. Wilkinson, R. J. Hughes, I. R. Fisher, P. C. Canfield, T. Jarlborg, and G. Santi. *Phys. Rev. Lett.*, 83:4824, 1999.

[124] M. El-Hagary, H. Michor, and G. Hilscher. *Phys. Rev. B*, 61:11695, 2000.

[125] K. E. Gray. *Phys. Rev. B*, 27:4157, 1983.

[126] I. K. Yanson. *Rare Earth Transition Metal Borocarbides (Nitrides): Superconducting, Magnetic and Normal State Properties*, volume 14 of *Series II: Mathematics, Physics and Chemistry*. Kluwer Academic Publishers, Dordrecht, 2001.

[127] W. E. Pickett and D. J. Singh. *Phys. Rev. Lett.*, 72:1994, 3702.

[128] A. K. Bhatnagar, K. D. D. Rathnayaka, D. G. Naugle, and P. C. Canfield. *Phys. Rev. B*, 56:437, 1997.

[129] H. Kawano-Furukawa, H. Takeshita, M. Ochiai, T. Nagata, H. Yoshizawa, N. Furukawa, H. Takeya, and K. Kadowaki. *Phys. Rev. B*, 65:R180508, 2002.

[130] Jens Jensen. *Phys. Rev. B*, 65:140514(R), 2002.

[131] M. S. Lin, J. H. Shieh, Y. B. You, W. Y. Guan, H. C. Ku, H. D. Yang, , and J. C. Ho. *Phys. Rev. B*, 52:1181, 1995.

[132] T. Akima, S. NishiZaki, and Y. Maeno. *J. Phys. Soc. Jpn.*, 68:694, 1999.

[133] M. B. Salamon. *Physical Properties of High Temperature Superconductors*, volume 1. World Scientific, Singapore, 1989.

[134] C. Broholm, G. Aeppli, R. Kleiman, D. Harshman, D. Bishop, E. Bucher, D. Williams, E. Ansaldo, and R. Heffner. *Phys. Rev. Lett.*, 65:2062, 1990.

[135] U. Rauchschwalbe, U. Ahlheim, F. Steglich, J. Aarts, K. Martini, and A. Mota. *Phys. Rev. Lett.*, 49:1448, 1982.

[136] T. Orlando and K. Delin. *Foundations of Applied Superconductivity.* Addison-Wesley, Reading, MA, 1991.

[137] A. P. Mackenzie, S. R. Julian, A. J. Diver, G. J. McMullan, M. P. Ray, G. G. Lonzarich, Y. Maeno, S. NishiZaki, and T. Fujita. *Phys. Rev. Lett.*, 76:3786, 1996.

[138] J. G. Bednorz and K. A. Muller. *Z. Phys.*, B64:189, 1986.

[139] Y. Maeno, S. NishiZaki, and Z. Q. Mao. *J. Supercond.*, 12:535, 1999.

[140] K. Ishida, Y. Kitaoka, K. Asayama, S. Ikeda, S. NishiZaki, Y. Maeno, K. Yoshida, and T. Fujita. *Phys. Rev. B*, 56:R505, 1997.

[141] A. P. Mackenzie, R. K. W. Haselwimmer, A. W. Tyler, G. G. Lonzarich, Y. Mori, S. NishiZaki, and Y. Maeno. *Phys. Rev. Lett.*, 80:161, 1998.

[142] Z. Q. Mao, Y. Mori, and Y. Maeno. *Phys. Rev. B*, 60:610, 1999.

[143] T. M. Rice and M. Sigrist. *J. Phys.: Condens. Matter*, 7:L643, 1995.

[144] K. Ishida, H. Mukuda, Y. Kitaoka, K. Asayama, Z. Q. Mao, Y. Mori, and Y. Maeno. *Nature*, 396:658, 1998.

[145] G. M. Luke, Y. Fudamoto, K. M. Kojima, M. I. Larkin, J. Merrin, B. Machumi, Y. J. Uemura, Y. Maeno, Z. Q. Mao, Y. Mori, H. Nakamura, and M. Sigrist. *Nature*, 394:558, 1998.

[146] K. Izawa, H. Takahashi, H. Yamaguchi, Yuji Matsuda, M. Suzuki, T. Sasaki, T. Fukase, and Y. Yoshida. *Phys. Rev. Lett.*, 86, 2653.

[147] Y. Hasegawa, K. Machida, and M. Ozaki. *cond-mat/9909316*, 1999.

[148] M. E. Zhitomirsky and T. M. Rice. *Phys. Rev. Lett.*, 87:057001, 2001.

[149] I. Mazin. *private conversation.*

[150] A. A. Golubov and I. I. Mazin. *Phys. Rev. B*, 55:15146, 1997.

[151] K. Deguchi, Z. Q. Mao, H. Yaguchi, and Y. Maeno. *cond-mat/0311366*, 2003.

[152] I. Giaever, Jr. H. R. Hart, and K. Megerle. *Phys. Rev.*, 126:941, 1962.

[153] J. C. Van Der Hoeven Jr. and P. H. Keesom. *Phys. Rev.*, 137:A103, 1965.

[154] A. Bennett. *Phys. Rev.*, 140:A1902, 1965.

[155] L. L. Daemen and A. W. Overhauser. *Phys. Rev. B*, 39:6431, 1989.

[156] X. M. Chen and A. W. Overhauser. *Phys. Rev. B*, 47:14338, 1993.

[157] J. D. Short and J. P. Wolfe. *unpublished.*

[158] J. R. Anderson and A. V. Gold. *Phys. Rev.*, 139:A1459, 1965.

[159] C. P. Poole Jr., H. A. Farach, and R. J. Creswick. *Superconductivity.* Academic Press, 1995.

Vita

Chia Ee Min Elbert was born on November 25, 1968 in Kadang Kerbau Hospital, Singapore. He attended Hwa Chong Junior College for his high school education from 1985 to 1986. In 1988 he won a Singapore Government Scholarship to study Mathematics and Physics at the University of Auckland, New Zealand, and obtained a B.Sc. (Honours) First Class in Mathematics in 1992. He also met his wife-to-be, Renee Yan Yu Woo, in Auckland. While in Auckland he won a Australian National University Vacation Scholarship, and did some theoretical research (Topic: "Quark Deconfinement: A Phenomenological Approach") under Dr. L. J. Tassie from November 1990 to February 1991. After returning to Singapore, Elbert spent nine months in the National Institute of Education, Nanyang Technological University, pursuing a Postgraduate Diploma in Education (Secondary), where he obtained a Distinction. Elbert then spent four very fulfilling years as a high school physics teacher in Temasek Junior College, Singapore, where he was made the Head of Department (Science) in 1998. In the Fall of 1998 Elbert came to the University of Illinois at Urbana-Champaign to pursue a Ph.D. degree in the Department of Physics. He held a teaching assistantship from September 1998 to May 1999. In May 1999 he joined Professor Myron Salamon's research group, and remained as a Research Assistant until the completion of his doctoral degree. Besides his wife Renee, he was also joined by his son Daniel Jia-Nuo Chia, who was born in August 18, 2001 in Covenant Hospital, Urbana.